REDUCED GRAPHENE OXIDE - COBALT TUNGSTEN OXIDE COMPOSITE THIN FILM FOR SUPERCAPACITOR AND OXYGEN EVOLUTION REACTION

By

Ms. PRITY P. BAGWADE

Under the Supervision of

PROF. C. D. LOKHANDE

Thesis Submitted to

D. Y. PATIL EDUCATION SOCIETY
INSTITUTION DEEMED TO BE UNIVERSITY
KOLHAPUR
DNYANADHEENAM JAGAT SARVAM

For the Degree of

Doctor of Philosophy in Physics
2022

REDUCED GRAPHENE OXIDE - COBALT TUNGSTEN OXIDE COMPOSITE THIN FILM FOR SUPERCAPACITOR AND OXYGEN EVOLUTION REACTION

A THESIS SUBMITTED TO

D. Y. PATIL EDUCATION SOCIETY (DEEMED TO BE UNIVERSITY), KOLHAPUR

FOR THE DEGREE OF

DOCTOR OF PHILOSOPHY

IN

PHYSICS

UNDER THE FACULTY OF

INTERDISCIPLINARY STUDIES

BY

Ms. PRITY PRAKASH BAGWADE

M. Sc.

UNDER THE SUPERVISION OF

Prof. CHANDRAKANT D. LOKHANDE

M. Sc., Ph. D.

CENTRE FOR INTERDISCIPLINARY RESEARCH,
D. Y. PATIL EDUCATION SOCIETY (DEEMED TO BE
UNIVERSITY), KOLHAPUR- 416 006, MAHARASHTRA, (INDIA)

(2022)

DECLEARATION

I hereby declare that the thesis entitled **"REDUCED GRAPHENE OXIDE - COBALT TUNGSTEN OXIDE COMPOSITE THIN FILM FOR SUPERCAPACITOR AND OXYGEN EVOLUTION REACTION"** submitted for the degree of **Doctor of Philosophy (Ph.D.)** in **Physics** under the faculty of **Centre for Interdisciplinary Research** of D. Y. Patil Education Society (Deemed to be University), Kolhapur is completed and written by me, has not before made the basis for the award of any other higher education institute in India or any other country to the best of my knowledge. Further I declare that I have not violated any of the provisions under Copyright and Piracy/Cyber/IPR Act amended from time to time.

Place: Kolhapur

Research Student

PBagwade

Date: 31 / 10 /2022

Ms. Prity Prakash Bagwade

D. Y. Patil Education Society

(Deemed to be University), Kolhapur

Centre for Interdisciplinary Research

CERTIFICATE

This is to certify that the thesis entitled ***"Reduced graphene oxide-cobalt tungsten oxide composite thin film for supercapacitor and oxygen evolution reaction"*** which is being submitted herewith for the award of the Degree of ***Doctor of Philosophy (Ph.D.)*** in ***Physics*** of ***D. Y. Patil Education Society (Deemed to be University), Kolhapur,*** is the result of the original research work completed by ***Ms. Prity Prakash Bagwade*** under my supervision and guidance and to the best of my knowledge and belief the work embodied in this thesis has not formed earlier the basis for the award of any degree or similar title of this or any other University or examining body.

Place: Kolhapur

Research Guide

Date:31/10/2022

Prof. Chandrakant D. Lokhande

Prof. C. D. LOKHANDE
Research Director
D. Y. Patil Education Society
(Institution Deemed to be University)
869, 'E', Kasaba Bawada
KOLHAPUR- 416006

ACKNOWLEDGEMENT

This was a beautiful journey, a journey of expanding the boundaries of knowledge, a journey of finding your strengths and weaknesses, a journey of becoming mentally and emotionally strong. It became more beautiful and interesting because of the people I met along the way. I would like to take this opportunity to acknowledge those fascinating people.

*Foremost, I would express my deepest gratitude to my genius mentor, **Prof. C. D. Lokhande**, Research Director, D. Y. Patil Education Society, for his guidance, support and many fruitful discussions during the course of this work. I am always amazed by his enthusiasm for science and how effectively he has shaped the young minds of two generations. I am very thankful to him for choosing me as his PhD student and I feel very fortunate to be part of CDL group.*

*I would like to express my sincere thanks to Vice-Chancellor **Prof. R. K. Mudgal**, Ex Pro-Vice Chancellor **Dr. Shimpa Sharma** and the Registrar **Dr. V. V. Bhosale** for the inspiration and support. I thank **Dr. U. M. Patil**, **Dr. J. L. Gunjakar**, and **Dr. Vishwajeet Khot** who helped me to analyse the results with all their empathy and cooperative mind. I also thank **Dr. A. C. Lokhande**, **Dr. V. C. Lokhande**, and **Dr. R. N. Bulakhe** for providing me important sample characterization data during entire research work.*

*I would like to express sincere thanks to my seniors **Dr. D. M. Malavekar**, **Dr. S. B. Ubale**, **Dr. T. T. Ghogare**, **Dr. S. B. Kale**, **Dr. S. J. Marje and Dr. P. K. Katkar**, **Dr. S. B. Pujari, Dr. S. A. Khalate, Dr. S. B. Sadavar, Dr. N. S. Padalkar and Dr. R. B. Shinde, Dr. S. B. Jadhav** for insightful guidance, scientific discussions and valuable suggestions on the present work.*

*To my dear friends **Vikas Magdum** and **Yogesh Chitare** thank you for always being there for me in any situation and supporting and helping me. I would like to acknowledge my colleagues at Centre for Interdisciplinary Research**, Shirin Kulkarni**, **Ranjit Nikam**, **Sambhaji Khot**, **Sambhaji Kumbhar, Shraddha Bhosale and Vinod Patil** for their wonderful collaboration. I want to thank them for their support and valuable suggestions during research work.*

I am also thankful to my friend ***Supreme Dhas*** *and* ***Sharad Patil*** *for their continuous support. I am also thankful to all teaching and nonteaching staff of the Centre for Interdisciplinary Research for their cooperation.*

My heartfelt appreciation goes out to my late father ***Prakash****, my mother* ***Aasha****, my lovely brother* ***Gautam****, and my lovely sister* ***Amruta*** *for their continuous support and love.*

~Prity

Place: Kolhapur

SUMMARY OF RESEARCH WORK

Published (Indian) Patents

1) A method for synthesis of dysprosium sulfide (Dy_2S_3) thin film and supercapacitive application thereof, Prof. C. D. Lokhande, Ms. T. T. Ghogare, **Ms. P. P. Bagwade**, Dr. V. V. Bhosale, (Application No: 201921046414).

2) Asymmetric solid state supercapacitor, Prof. C. D. Lokhande, **Ms. P. P. Bagwade**, Ms. T. T. Ghogare, Dr. V. V. Bhosale, (Application No:202021000458).

3) Chemical synthesis of cadmium selenide/reduced graphene oxide composite thin film and photoelectrochemical cell application, Prof. C. D. Lokhande, Mr. R. P. Nikam, Mr. S. D. Khot, **Ms. P. P. Bagwade**, Mr. D. J. Patil, (Application No: 202121062097).

4) Electrochemical supercapacitor device, Prof. C. D. Lokhande, **Ms. P. P. Bagwade**, Dr. D. B. Malavekar, Mr. S. D. Khot, Mr. R. P. Nikam, (Application No: 202221029730).

5) Chemical Synthesis of reduced graphene oxide - dysprosium selenide composite thin films for energy storage device, Prof. C. D. Lokhande, Mr. S. D. Khot, Dr. D. B. Malavekar, Mr. R. P. Nikam, **Ms. P. P. Bagwade** (Application no. 202221021506).

6) A electrochemical method of preparation of managanese ferrite thin films on conducting substrates for energy storage, Dr. V. S. Jamdade, Mr. R. P. Bhosale, Dr. N. L. Tarwal, **Ms. P. P. Bagwade**, Prof. C. D. Lokhande, (Application no. 202221030806).

Papers Accepted at International Journals

1) **P. P. Bagwade,** D. B. Malavekar, T. T. Ghogare, S. B. Ubale, V. J. Mane, R. N. Bulakhe, I. In, C. D. Lokhande, A high performance flexible solid-state asymmetric supercapacitor based on composite of reduced graphene oxide@dysprosium sulfide nanosheets and manganese oxide nanospheres, J. Alloys Compd., 859 (2021) 157829 **(I. F- 6.37).**

2) **P. P. Bagwade**, D. B. Malavekar, S. B. Ubale, T. T. Ghogare, R. N. Bulakhe, I. In, U. M. Patil, C. D. Lokhande, Characterization of Dy_2S_3 thin films deposited by successive ionic layer adsorption and reaction (SILAR) method, Solid State Sci., 119 (2021) 106693 **(I. F-3.75).**

3) **P. P. Bagwade,** D. B. Malavekar, S. B. Ubale, R. N. Bulakhe, I. In, U. M. Patil, C. D. Lokhande, Synthesis, characterization and supercapacitive application of nanocauliflower-like cobalt tungstate thin films by successive ionic layer adsorption and reaction (SILAR) method, Electrochim. Acta, 408 (2022) 139933 **(I.F-7.33).**

4) **P. P. Bagwade**, V. V. Magdum, D. B. Malavekar, Y. M. Chitare, J. L. Gunjakar, U. M. Patil, C. D. Lokhande, Synthesis, characterization and visible light driven dye degradation performance of one pot synthesized amorphous $CoWO_4$ powder, J. Mater. Sci. Mater., (2022) **(I. F-2.77).**

5) **P. P. Bagwade,** D. B. Malavekar, V. V. Magdum, S. D. Khot, R. P. Nikam, D. J. Patil, U. M. Patil, C. D. Lokhande, Nanocrystalline Cobalt Tungstate Thin Films Prepared by SILAR Method for Electrocatalytic Oxygen Evolution Reaction, Int. J. Hydrog. Energy, (2022) **(I.F- 7.13).**

6) S. D. Khot, D. B. Malavekar, R. P. Nikam, S. B. Ubale, **P. P. Bagwade**, D. J. Patil, V. C. Lokhande, C. D. Lokhande, SILAR synthesized dysprosium selenide (Dy_2Se_3) thin films for hybrid electrochemical capacitor, Synth. Met., 287 (2022) 117075 **(I. F-4.0).**

7) S. B. Ubale, S. B. Kale, V. J. Mane, **P. P. Bagwade**, C. D. Lokhande, SILAR synthesized nanostructured ytterbium sulfide thin film electrodes for symmetric supercapacitors, J. Solid State Chem., 25 (2021) 1753 **(I. F-3.65).**

8) H. L. Pushpalatha, T. T. Ghogare, N. H. Vibhu, **P. P. Bagwade**, R. N. Bulakhe, I. In, and C. D. Lokhande, Characterization of soft chemically deposited yttrium sulfide (Y_2S_3) thin films, Materials Today: Proceedings, 59 (2022) 1236 **(I.F-.1.42).**

9) D. J. Patil, D. B. Malavekar, V. C. Lokhande, **P. P. Bagwade**, S. D. Khot, T. Ji, C. D. Lokhande, Binder free synthesis of mesoporous nickel tungstate for Aqueous Asymmetric Supercapacitor Applications: Effect of film thickness, Energy Technol., **(I.F-3.63).**

10) R. P. Bhosale, S. S. Kumbhar, P. P. Bagwade, C. D. Lokhande, V .S. Jamadade, Chemical synthesis of manganese ferrite thin films for energy storage, Solid state Sci., **(submitted) (I. F-3.75).**

Papers/Poster Presented at National/International Conferences

1) International Conference on “Recent Advances in Materials and Manufacturing (ICRAMM 2021)”- 25th and 26th November 2021, DYPET Kolhapur.
2) National Conference on “Emerging Trends in Chemistry”- 10th February 2022, SMM Akluj.
3) Asian e-Conference on “Engineered Science” 2020 -5th-6th December 2020, PSGVP college, Nandurbar.
4) International seminar series on “Nanotechnology for Envoirnment and sustainability”- 12th and 13th January 2021.
5) International conference on “Cancer Biology: Basic science to translational research”- 17th and 18th January 2020.
6) Poster presentation on “High performance flexible solid state supercapacitor device based on cobalt tungsten oxide nanoparticles” -28th February 2022

Workshops Attended

1) Workshop on “Good Laboratary Practices”- 6th February 2021, DYP Education society, Kolhapur.

CONTENTS

List of Figures

Chapter 1 **Introduction and literature survey**

Chapter 2 **Basic of SILAR Method and Thin Film Characterization Technique**

Chapter 3 **Synthesis, characterization, supercapacitive and electrocatalytic performance of cobalt tungsten oxide thin film electrode**

Chapter IV **$CoWO_4$ and $CoWO_4$@rGO thin films by SILAR method; characterizations, electrochemical and electrocatalytic performance**

Chapter V **Fabrication and performance evaluation of asymmetric FSS–SSCs device based on $CoWO_4$@rGO and CuS thin films**

List of Charts and Tables

LIST OF ABBREVIATIONS

AC	Activated carbon	**HSC**	Hybrid capacitor
AR	Analytical reagent	**IR**	Internal resistance
ASC	Asymmetric supercapacitor	**KOH**	Potassium Hydroxide
BET	Brunauer-Emmett-Teller	**LEDs**	Light emitting diodes
BJH	Barrett-Joyner-Halenda	**LIBs**	Lithium-ion batteries
CBD	Chemical bath deposition	**P**	Adsorptive pressure
CC	Carbon Cloth	**PAA**	Polyacrylate
CCD	Charge coupled device	**PAN**	Polyacrylonitrile
C_{dl}	Double Layer Capacitance	**PANI**	Polyaniline
CF	Carbon foam	**PC**	Propylene carbonate
CNTs	Carbon nanotubes	**PEC**	Photoelectrochemical
C_s	Specific capacitance	**PEO**	poly (ethylene oxide)
CV	Cyclic voltammetry	**PMMA**	Poly (methyl methacrylate)
CVD	Chemical vapour deposition	**PPy**	Polypyrrole
DDW	Double distilled water	**Ps**	Saturated vapour pressure
EC	Ethylene carbonate	**PTh**	Polythiophene
ECSA	Electrochemical Active Surface Area	**PV**	Photovoltaic
EDAX	Energy dispersive X-ray spectroscopy	**PVA**	Poly (vinyl alcohol)
EDLC	Electric double-layer capacitors	**PVF**	Poly (vinylidene fluoride)
EIS	Electrochemical impedance spectroscopy	**Q**	Stored charges
EMC	Ethyl methyl carbonate	**R_{ct}**	Charge transfer resistance
FE–SEM	Field emission scanning electron microscopy	**rGO**	Reduced graphene oxide
FT-IR	Fourier transform infrared spectroscopy	**RHE**	Reversible Hydrogen Electrode
FWHM	Full width at half maximum	**R_s**	Series resistance
GCD	Galvanostatic charge-discharge	***SB***	Specific surface area
GCE	Glassy Carbon Electrode	**SCE**	Saturated calomel electrode
GNS	Graphene nanosheets	**SCs**	Supercapacitors

GO	Graphene oxide	**S_E**	Specific energy
HER	Hydrogen Evolution Reaction	**SILAR**	Successive ionic layer adsorption and reaction
Hg/HgO	Mercury/mercury oxide	**TMCs**	Transition metal chalcogenides
S_P	Specific power	**t_0**	Relaxation time constant
SS	Stainless steel	**ΔE**	Potential window
SSC	Symmetric supercapacitor	***W***	Warburg impedance
ST	Total surface area	**XRD**	X-ray diffraction
		XPS	X-ray photoelectron spectroscopy

CHAPTER-1

General Introduction and Literature Survey

CHAPTER 1

General Introduction and Literature Survey

1.1 General: Introduction

1.1.1 Need of supercapacitor:

Renewable energy sources are in high demand due to their ability to generate and store energy, as well as, cost effectiveness compared to non-renewable energy sources which are available in limited supply. Although, renewable energy sources such as sun, wind etc. are not stable and efficient storage is not possible [1]. This problem is overcome by use of electrical energy storage (EES) technologies such as batteries, fuel cells, flywheel and supercapacitors (SCs) [2]. Batteries are being widely used nowadays can be of rechargeable and non-rechargeable type, wherein chemical energy produced due to redox reactions occurring at a cathode and an anode get converted into electrical energy. The process of redox reactions is reversed for limited times in rechargeable type of batteries [3]. Although only batteries cannot provide complete solution for electricity storage due to limitations such as low power density, heat generation, and limited life cycles [4, 5]. Therefore, there is a demand for long-lasting and safe electricity storage device with high power and energy density. This can be achieved using supercapacitor that has greater specific capacity and specific energy related to conventional capacitors. Further, they are characterized by greater specific power, shorter charging time, more efficient discharging than batteries, and they cause no pollution in the environment [6]. On the contrary, their energy density is 10 to 50 times lower than lithium ion batteries, but supercapacitors with a near unlimited cycle life are useful in the fields of power system, memory storage, and vehicle assistant equipment [7]. This can be explained by example such as creating an electric vehicle with longer life, lower costs, and more power by combining a supercapacitor and a battery in single unit. Classification of SCs depending upon principle of energy storage can be given as electric double-layer capacitors (EDLCs) which stores charges using the very thin double layer structure formed at the interface between electrode and electrolyte, and pseudo-capacitors which use fast, and reversible redox reactions on the surface and bulk near the surface of electrodes for energy storage [4]. In contrast EDLCs, pseudo-capacitors exhibit higher capacitance, and higher energy density [6–10]. Energy in the battery is stored by means of chemical reactions whereas, in SCs by simply electrostatic charge transfer for various energy storage devices. Figure 1.1 shows Ragone plot of energy density vs. power density.

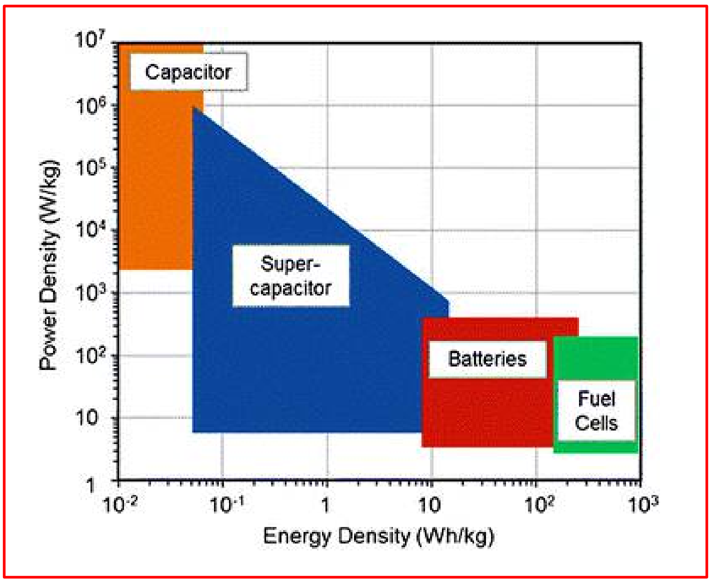

Figure 1.1 Ragone plot of energy density vs. power density for various energy-storing devices.

1.1.1.1 Types of supercapacitors:

SCs have been classified by using different definitions and terms. But these are generally termed as electrochemical capacitors to distinguish them from the conventional capacitors. Helmholtz, first recognized that the electrical charge could be stored not only on the surface of the conductor but also at the interface of the electrode/electrolyte [11, 12]. Electric double-layer capacitor by using SCs terminology is used to explain carbon-based SCs, in which the charge and discharge processes are very rapid, due to the simple electric charge orientation of the double layer at the electrode/electrolyte interface. Whereas, in reality, an electric double-layer capacitor is equivalently used for two different definitions: (i) electric double layer capacitor or (ii) electrochemical double layer capacitor. By using features of specific capacitance (C_s), having a different way of working, 'Pseudo-capacitors' have been developed. In this, there is incomplete storage of electrical charge in the 'double layer' and partially is results due to faradaic reactions (charge transfer of electrons and protons) between the electrode and electrolyte. As can be seen working mechanisms is shifted from conventional capacitor to electrochemical battery [13-15]. The uses of SCs can be identified in particular materials in the electrolyte such as organic, aqueous, ionic liquids and solids or in the electrodes such as activated carbons, electronically conducting polymers, metal oxides, and battery-like components [16, 17]. As shown in chart 1.1, all the previous commercial and under progress supercapacitor can be divided into three main categories including a) Symmetric SCs, b) Asymmetric supercapacitor, and c) Hybrid supercapacitor. Each category is explained in brief as follows:

a) Symmetric supercapacitor (SSC):

It is termed as symmetric because electrodes used in it are made up of the same material with the identical design and, practically, similar mass is deposited on both of them [16]. The electrodes are characterized by equal fundamental charge storage principle efficiently working (either physical or chemical or a combination of the two). In this category of symmetric supercapacitor two classes are involved that are i) EDLC and (ii) Pseudo-capacitors.

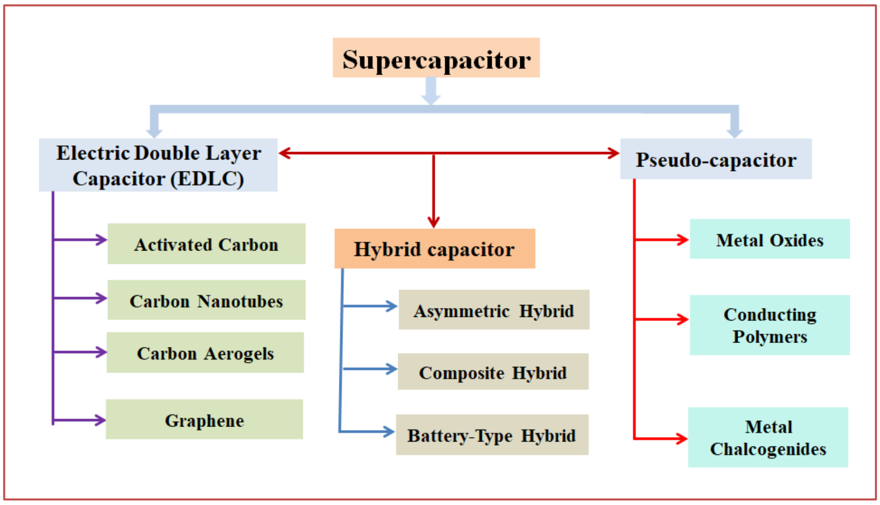

Chart 1.1 Classification of supercapacitor.

i) Electric double-layer capacitors:

In these capacitors, the electrical charge is deposited on the double layer, which is created at the electrode–electrolyte interface under applied bias. They are characterized by extreme reversibility and extended life due to absence of chemical reactions and material conversions that exist during charge and discharge cycles. Due to the use of double-layer charge storage at both electrodes, increase C_s with respect to conventional capacitors can be obtained. Materials such as activated carbons possessing considerably higher surface area and extremely small thickness of double layers are used in EDLC supercapacitors, compared to the electrode distance in conventional capacitors [17]. There is utilization of double layer nonfaradic capacitance, with different electrolytes (aqueous, organic and ionic liquids) and electrodes (activated carbons, carbon aerogels and carbon nanotubes) in all EDLC supercapacitors.

ii) Pseudo-capacitors:

The second class of symmetric supercapacitors is pseudo-capacitors, consisting of electrodes with active materials that work dissimilarly from EDLC to store electrical charge and energy. Double-layer assures the charge storage between electrode and electrolyte, whereas, a larger amount of charge transfer and storage is resulted because of faradic mechanisms such as electrosorption, redox reactions, and intercalation. The latter process is capable of doubling the energy density more than that of EDLC. In recent years, materials possessing good pseudo-capacitive properties have been detected such as iridium dioxide, ruthenium dioxide, nickel oxide and their mixtures [18, 19]. Conducting polymers enhance the attractiveness, whereas, applications needing limited cycle number may take advantage of the substantially greater energy density of any kind of pseudo-capacitor. These devices have some drawback in the use of precious metals, which made their application relatively expensive.

b) Asymmetric supercapacitor (ASC):

The asymmetric supercapacitor is characterized by dissimilar processes with respect to its nature [20]. Redox reactions are occurring on first electrodes and charge-discharge of electrostatic charge storage in the electric double-layer on second electrode serve as a representative example of this category of supercapacitor. For such SCs, term hybrid is also used these days. This category includes, all the improved symmetric supercapacitors, in which there are changes in the electrolyte compositions and in the mass loading, geometry of the electrodes, without changing the active materials and the operating processes.

c) Hybrid supercapacitor:

Hybrid supercapacitor are the most innovative which combines the better performances of different supercapacitor. Their purpose is to improve technical characteristics, and even reduce costs of more conventional SCs using different materials for each electrode. Combinations of positive and negative electrodes coming from different technologies have been obtained due to current research and development activities. To be able to decrease the gap between supercapacitor and electrochemical batteries is the major technological challenge. Two electrodes made of dissimilar materials and, eventually, using different working processes (faradic and non-faradic) is the fundamental design of a hybrid supercapacitor. Aims of investigated combinations are to maintain extended cycle life of EDLC and power capacity of conventional capacitors along with decreasing the cost constraints of pseudo-capacitors to enhance energy density to get closer to those of batteries. This category encompasses main three types as follows: (i) hybrid electrolytic, (ii) composite, and (iii) battery-like supercapacitor.

i) Hybrid electrolytic capacitors:

It is a pseudo-capacitive electrode based on metal oxides, which can be combined with the electrode of a conventional electrolytic capacitor. Due to this, the high power characteristic of electrolytic capacitors is saved, but the addition of the capacitance pseudo-capacitance on one electrode substantially augments the specific of the device.

ii) Composite supercapacitor:

The second class of hybrid supercapacitor is characterized by devices, which combines the electrode of an EDLC with a composite electrode, using carbon-based material (e.g. carbon nanotubes) that incorporates either conducting polymers or a metal oxide [11, 13]. Such devices are also called asymmetric hybrid supercapacitors.

iii) Battery-type supercapacitor:

These SCs contain two different electrodes, which belong to two different storage mechanisms. The supercapacitor electrode is attached with a battery electrode. Different combinations of supercapacitor electrodes with electrode derived from batteries such as lead acid (lead oxides), alkaline (nickel oxides) and lithium are investigated in recent researches [19–21]. Apart from need to overcome battery-related limitations, these devices are interesting due to their usefulness.

1.1.2 Need of oxygen evolution reaction:

Among the various global problems, energy has emerged as an inevitable one and has evoked enormous research attention into this field. The worldwide energy consumption is increasing every year due to rapid industrialization as well as urbanization. This in turn increasing energy demand exponentially. Therefore, energy crisis is going to hike to a greater extent in coming years. Currently, large portion of energy is generated by the burning of fossil fuels. Around 80 % of the today's energy is generated by fossil fuels [22]. In addition, burning of fossil fuel produces lots of (CO_2) which again creates environmental pollution [23, 24]. Now it is time for humans to decrease the dependence on fossil fuels for the generation of energy as they are going to finish in near future. Therefore, an alternative source of energy is required to formulate which can provide energy without producing any secondary pollution and without affecting the environment [25, 26]. Recently, hydrogen (H_2) has gained substantial research preference as the source of clean and green energy [27-31]. The H_2 has been widely considered as the alternative energy source to replace the conventional energy generation sources and is able to deprive the dependence on the burning of fossil fuels [32, 33]. The H_2 possess high energy and it creates no pollution during combustion. Therefore, H_2 is widely being considered as future energy carrier and many countries and industries are using H_2 energy to fulfill their energy demands. However, H_2 cannot be obtained directly but it has to be produced at industries. Different techniques for H_2 production includes steam reforming, coal gasification and electrolysis of water. Steam reforming is a process in which methane (in natural gas) is heated in steam in presence of catalyst which produces carbon monoxide (CO) along with H_2. It is known that CO is a harmful gas that creates environmental pollution. On the other hand, coal gasification produces CO_2, CO and H_2 upon oxidation of coal by air, steam or CO_2 under certain conditions. This process also involves generation of environmentally harmful gases like CO, and CO_2 [34].

1.1.2.1 Electrochemical water splitting:

In that context, electrochemical water splitting finds advantageous method for the effective production of H_2 without creating any environmental harm. Electrochemical water splitting has emerged as an efficient method for the production of H_2 and oxygen (O_2). The method offers clean and green generation of H_2 and O_2, which involves decomposition of H_2O into its constituent elements (H_2 and O_2) by passing electricity through it. The simple electrolysis reaction can be written as follows.

$$2H_2O\ (l) \rightarrow 2H_2\ (g) + O_2\ (g) \qquad 1.1$$

This overall water splitting reaction consists of two half reactions. One is hydrogen evolution reaction (HER) taking place at cathode whereas oxygen evolution reaction (OER) taking place at anode. The half reactions initiate reduction of water at cathode and oxidation of water at anode which are represented as follows.

$$4H^+\ (aq) + 4e^- \rightarrow 2H_2\ (g)\ \text{(reduction of water at cathode)} \qquad 1.2$$

$$2H_2O\ (l) \rightarrow O_2\ (g) + 4H^+\ (aq) + 4e^-\ \text{(oxidation of water at anode)} \qquad 1.3$$

In this reaction, H_2 is generated at cathode whereas O_2 is generated at anode as by-product. A theoretical potential of 1.23 V is required to initiate water splitting. However, due to reaction kinetics, some additional potential need to be given. The additional potential is termed as overpotential (η). Figure 1.2 shows schematic of the electrolysis of water.

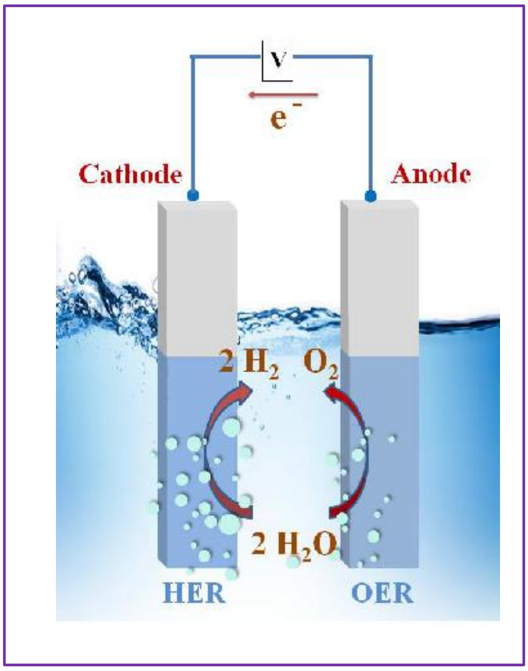

Figure 1.2: Schematic of the electrolysis of water.

1.1.2.2. Oxygen evolution reaction (OER) and measurement parameters:

As stated above, O_2 is the byproduct of the electrochemical water splitting reaction where the half reaction taking place at the anode is called as OER [35]. Theoretically, 1.23 V is required to initiate the OER reaction at anode [36, 37]. However, due to solution resistance, contact resistance and intrinsic reaction activation barrier the extra potential is required which makes the OER a sluggish one [38, 39]. In addition, OER requires transfer of 4 electrons in order to complete the reaction which generates different intermediate products that again results into the sluggish kinetics. The transfer of 4 electrons can be understood by following reactions.

$M + H_2O\ (l) \rightarrow MOH + H^+ + e^-$ 1.4

$MOH + OH- \rightarrow MO + H_2O\ (l) + e^-$ 1.5

$MO + H_2O\ (l) \rightarrow MOOH + H^+ + e^-$ 1.6

$MOOH + H_2O\ (l) \rightarrow M + O_2(g) + H^+ + e^-$ 1.7

The different intermediates include generation of O, OH, and OOH groups which transfers electrons through multistep reactions which eventually evolve one O_2 molecule [40, 41]. This slow and un-efficient reaction can be made faster by using different electrocatalysts which increases the rate of reactions to lower the overpotential value. To date, IrO_2 and RuO_2 are considered as best electrocatalysts for the efficient generation of O_2 [42, 43]. But their non-earth abundance limits their practical use at a large scale O_2 production. Therefore, there is an urgent need to find a competent material that can produce O_2 at a lower overpotential value and can sustain its structure for a longer period of time. Although, there are certain requirements for an electrocatalysts to give best performance by working at lower overpotential. It should possess a higher number of catalytically active sites. It should possess well defined porous morphology to transport O_2 evolved during the reaction. It should have high electrical conductivity. And it should have suitable band positions for the oxidation of water to occur electrolysis.

The performance measurement of an electrocatalyst is very crucial factor while studying the OER. It is well known that lower overpotential is a prime requisite and most important aspect to compare the OER performance.

However, some other factors are also required to consider for thorough study of an electrocatalyst while studying OER. The different aspects of OER study are discussed in details below.

1.1.2.2.1 Overpotential (η):

Overpotential is the most important factor to determine the OER performance of an electrocatalyst. Overpotential is defined as the additional potential required than that of theoretical potential (1.23 V) to initiate the electrochemical water splitting. A good electrocatalyst is characterized by its lower value of overpotential. That means lower the value of overpotential, the electrocatalyst is more efficient. Generally, overpotential is measured at the current density of 10 mA cm^{-2}. Overpotential is composed of three different types viz. activation overpotential, concentration overpotential, and resistance overpotentials which can be reduced by using different strategies. For example, selecting the appropriate electrocatalyst, or stirring the electrolyte solution can help to lower the overpotential.

1.1.2.2.2 Tafel slope (b):

Tafel slope is the measure of how efficiently an electrocatalyst can change the current density with respect to the applied potential. In turn, Tafel slope explains the charge transfer process. Therefore, lower Tafel slope shows the good OER property of an electrocatalyst. Tafel slope can be calculated by following equation:

$$\eta = a + b\log(j) \qquad 1.8$$

where, η is overpotential, a is Tafel constant, b is Tafel slope and j is current density.

1.1.2.2.3 Stability:

Stability is measure of the ability of an electrocatalyst to perform OER for a longer period of time. Generally, stability study is done in almost every applications including supercapacitor, gas sensor etc. Likewise, stability study is conducted in OER to study the applicability of the catalyst over a long time. The stability study can be conducted either by performing chronoamperometry (CA) or chronopotentiometry (CP) technique for a defined time period. In CA technique, a constant potential is given and current density is measured with respect to time for a given period of time. In CP technique, a constant current density is given and required potential to achieve the given current density is measured with respect to time for a given time period. A good electrocatalyst need to stable for a longer time.

1.1.2.2.4 Oxygen evolution electrocatalysts:

As seen in the above section, the formation of different intermediates takes place with the extraction of four electrons during OER. Given this, the electrocatalyst material becomes critically eminent. Indeed, it must overcome significant challenges to be considered an effective electrocatalysts for oxygen evolution. A suitable catalyst must bind the reactants (intermediate species) neither too strongly nor too feebly, because, according to Sabatier's principle strong or feeble binding leads to either poor adsorption of reactants or difficulty in removing final products, respectively [44]. The state-of-the-art OER catalysts have intermediate bonding strengths, which is one of the reasons for their excellent activity. The electrochemical water oxidation reaction takes place only on active sites existed at the surface of catalyst material; hence, an efficient electrocatalyst must possess a larger quantity of active sites [45]. During OER an electron is generated at each intermediate step. These electrons must be conducted to another half part of the water splitting reaction (or to anode) through an external circuit. For this, the electrocatalyst must be an electrically good conductor [46]. Therefore, the catalyst materials which can overcome these obstacles are highly appreciable in the field of electrochemical water splitting. In the past decades, considerable efforts have been devoted to the development of an efficient electrocatalyst for OER. As the state-of-the-art catalysts for oxygen evolution reaction are expensive and rare, there has been considerable interest in oxygen evolution electrocatalysts that use more abundant elements. An extensive literature survey suggests that the first row (3d) transition metals have long been known to be effective OER catalysts because of their low cost, high activity and long term stability under oxidation conditions.

1.1.2.2.5 Metal oxides as OER catalysts:

Up to now, numerous investigations have been reported while examining transition metal oxides in the thirst for identifying suitable electrocatalyst for water oxidation. Among the transition metal based oxide catalysts, $CoWO_4$ is one of the earlier used oxide as an OER catalyst in an alkaline medium due to its high stability and special 3d electronic configuration [48-50]. Although $CoWO_4$ have good stability and good catalytic activity, it is still inferior to noble metal oxides. It is found that binary, as well as ternary metal oxides, show better electrocatalytic OER performance than corresponding single metal oxide [51-59]. More than one transition metals produce synergistic effects that can effectively regulate the physicochemical properties of oxides and further improve catalytic activity. Most of the above mentioned metal oxides show the excellent electrocatalytic ability for OER, still, their usage is constrained due to the poor intrinsic electronic conductivity.

1.2 Literature survey on synthesis of cobalt tungsten oxide thin films:

The transition metal tungstate has attracted great attention due to their excellent physical and electrical properties useful for applications in electronic, optical, and optoelectronic devices [60]. In recent years, nanostructured transition metal tungstate have been investigated as a new class of energy storage material. The common characteristic of tungstates is that their metal constituent can appear in two or more valence states [61]. Also, while modelling anodic oxidation reaction of covellite, it was established that the equivalent electrical circuit has to contain one relatively high capacitor.

Metal tungstate represents promising and attractive electrode materials for SCs due to their high C_s, high energy density and better cycling stability as compared to conducting polymers. Metal tungstates had been the area of research interest because of its size and shape dependent properties that makes them applicable for practical applications. Metal tungstates of commonly AWO_4 type (A=Metal); the structure depends upon the metal in the metal tungstates. The large A^{2+} cations (A = Ba, Ca, Eu, Pb, Sr) show tetragonal, scheelite structure whereas the small A^{2+} cations (A = Co, Cd, Fe, Mg, Ni, Zn) show monoclinic wolframite structure. The AWO_4 type of metal tungstates have been used since recent years as laser host materials, scintillators, oxide ion conductors, magnetic materials, opto-electronic devices and antibacterial material.

The transition metal oxide and hydroxide electrodes with pseudo-capacitive behaviour are of great interest in SCs. Due to the different oxidation states transition metal oxides are greatly studied as pseudo-capacitive materials; for example oxides of Ru, Ni, Co, Mn, and Fe [62, 63]. Alloys and binary metal oxides have shown greater advantages than single metal oxides due to their reasonable oxidation states and current response. Recently, binary metal oxides such as $NiCo_2O_4$ [64], $FeWO_4$ [65], $NiMoO_4$ [66], $ZnWO_4$ [67], $TbWO_4$ [68], and $NiWO_4$ [69] have displayed outstanding pseudo-capacitive performance. The binary metal oxides do not show the highest performance in every case and not in all environments. The pseudocapacitive performance of electrode material depends on number of factors, such as electrolyte concentration, type of electrolyte (neutral, alkaline, and acidic), mass loading, electrical conductivity, crystalline nature, etc. In fact, some single component metal oxides have shown promising electrochemical performance. For example, cobalt oxide showed C_s of 127.58 F g^{-1} in 1 M KOH electrolyte [70]. In addition to this, pseudo-capacitive nature of WO_3 has been also reported. Ling et al. [71] reported C_s of 538 F g^{-1} for hydrothermaly prepared WO_3. These reports proved that single metal oxides also showed good electrochemical performance for energy storage. In case of metal tungstates the crystalline structure as well as existence of binary metal helps in the improvement in the C_s and stability [72], some of previous reports also suggest that tungstates showed improvement in pesudocapacitive performance than corresponding oxide [73].

Amongst these metal tungstates, $CoWO_4$ is a p-type semiconductor compound exhibiting outstanding catalytic and electrochemical properties [74]. It shows high chemical stability and possesses narrow size distribution with excellent phase composition. Due to optical features it has been utilized as an efficient photocatalyst for environmental restoration. It exhibits superior electrochemical properties than Co_3O_4 material owing to the multiple valence states of Co, and W and higher electrical conductivity [75]. Thus, $CoWO_4$ is a very favourable electrode material for supercapacitor. Li et al. [73] reported preparation of $CoWO_4$ nanoparticles through hydrothermal method in the mixture of deionized water and ethylene glycol as a solvent and achieved C_s of 1817.14 F g^{-1} at current density of 1 A g^{-1}. Lokhande and Ji [76] prepared $CoWO_4$ by hydrothermal process and reported C_s of 1372 F g^{-1} at a scan rate of 5 mV s^{-1}. There are several methods to produce these nanostructures such as sol-gel, chemical bath deposition (CBD), chemical vapour deposition (CVD), and hydrothermal.

1.2.1 Literature survey of cobalt tungsten oxide based supercapacitor:

Table 1.1 shows the specific energy and specific power values by $CoWO_4$ and their composites using different chemical methods of preparation, with electrolyte used in supercapacitors.

1.2.1 Literature survey of cobalt tungsten oxide based supercapacitors

Sr. No.	Material	Synthesis method	Substrate	Surface morphology	Electrolyte	Specific capacitance (F g^{-1})	Potential Window (V)	Stability (%) (cycles)	Ref. No.
1	$CoWO_4$	Hydrothermal	Nickel foam	Nanosheets	1 M KOH	1127.6	0 to 0.5	92.4 (3000)	77
2	$CoWO_4$	Hydrothermal	Nickel foam	Nanoparticles	2 M KOH	764.4	-0.2 to 0.8	50.6 (6000)	78
3	$CoWO_4$	Hydrothermal	GCE	Dandelion like	6 M KOH	1871.1	0 to 0.55	92 (1000)	79
4	$CoWO_4$	Coprecipitation	GCE	Cauliflower like	2 M H_2SO_4	378	0 to 0.4	95 (4000)	80
5	$CoWO_4$	Chemical and Hydrothermal	Nickel foam	Nanoparticles	1 M KOH	403	-0.5 to 0.5	(10,000)	81
6	$Co_3O_4/CoWO_4$	Hydrothermal	Carbon cloth	Hill like-hemisphere	6 M KOH	331.6	0 to 0.6	70.2 (2000)	82
7	$NiWO_4$-$CoWO_4$	Coprecipitation	GCE	Nanoparticles	2 M KOH	196.7	0 to 0.6	-	83
8	$CoWO_4/Co_3O_4$	Hydrothermal	Nickel foam	Nanospheres	3 M KOH	1728	-0.25 to 0.45	85.9 (5000)	84

9	rGO/$CoWO_4$	Hydrothermal	GCE	Nanoparticles	2 M KOH	159.9	-0.3 to 0.4	94.7 (1000)	85
10	NrGO/$CoWO_4$	Hydrothermal	GCE	Nanowire	2 M H_2SO_4	597	0.0 to 0.5	97 (4000)	86
11	$Co_{1-x}Ni_xWO_4$	Hydrothermal	carbon cloth	Nanostructure	1 M KOH	430.3	-0.1 to +0.3	85.4 (5000)	87
12	$CoWO_4$/$NiCo_2O_4$	Hydrothermal	Nickel foam	Nanorod	6 M KOH	1076	-0.2 to 0.4	80 (2000)	88
13	Co1-xNixWO$_4$	Hydrothermal	Carbon cloth	Nanoparticles	1 M KOH	430.30	-0.1 to 0.3	85.4 (5000)	89
14	$NiWO_4$/$CoWO_4$	wet chemical	Al	Plate like	1 M KOH	862.26	1 to 2.5	96.12 (2000)	90
15	$CoWO_4$	Hydrothermal	Nickel foam	Nanoparticles	6 M KOH	1 817.14	-0.2 to 0.8	92 (1000)	91
16	$CoWO_4$/Co−B	Hydrothermal and wet-chemical	GCE	Nanoflake-like	6 M KOH	612	-1 to 0	95.62 (10000)	92
17	$CoWO_4$/NF	Hydrothermal	Nickel foam	Nanoparticles flower-like	6 M KOH	1395	0 to 0.6	79 (3000)	93
18	$NiWO_4$ and $CoWO_4$	Hydrothermal	Nickel foam	Hill-like hemisphere	2 M KOH	797.8 & 764.4	0 to 0.6	(3000)	76

19	CuAl-LDH/$CoWO_4$	Solvothermal	Nickel foam	Nanoflowers	2 M KOH	675	0 to 0.5	97.1 (5000)	94
20	$CoWO_4/Co_{1-x}S$	Hydrothermal	Nickel foam	Rod-like	3 M KOH	1894.5	0 to 0.6	87.27 (5000)	95
21	$CoWO_4$	Hydrothermal	Nickel foam	Nanosheets	1 M KOH	1127.6	0.0 to 0.6	92.4 (3000)	96
22	$CoWO_4$	Hydrothermal	Carbon cloth	Spherical Nanoparticles	3 M KOH	1372	-0.2 to 0.4	96 (4000)	97
23	$NiWO_4$	Hydrothermal	Glassy carbon electrode	Chain-like	2 M KOH	1524	-1.0 to1.0	-1.0 – 1.0	98
24	$CoWO_4$/NrGO	Sonochemical	N- doped graphene	Hierarchical	2 M H_2SO_4	597	-0.5 to 0.5	97.1 (4000)	99
25	$CoWO_4/Co_3O_4$	Hydrothermal	Nickel foam	Nanowire	3 M KOH	1728	0 to 0.5	85.9 (5000)	100
26	$CoNiWO_4$	Hydrothermal	glassy carbon electrode	Spherical nanoparticles	6 M KOH	723.8	-0.2 to 0.6	77.4 (3000)	101
	$CoNiWO_4$/P-S-GNS			Nanosheets		1298.6	-0.2 to 0.6	89.8 (3000)	
27	rGO/$CoWO_4$	Hydrothermal	Nickel foam	Nanospheres	2 M KOH	159.9	-0.25 to 0.5	94.7 (1000)	102

28	$CoWO_4$	Wet-chemical	Nickel foam	Nanoparticles	1 M KOH	403	0.0 to 0.6	10,000	103
		Hydrothermal	Nickel foam	Nanoparticles	1 M KOH	264	0.0 to 0.6	10,000	103
29	$Co_{0.5}Ni_{0.5}WO_4$	Hydrothermal	Nickel foam	Nanosheets	2 M KOH	626.4	0.0 to 0.7	105.3 (10,000)	104
30	$CoWO_4/CoMn_2O_4$	Hydrothermal	Nickel foam	Nanoflakes	3 M KOH	2259.6	-0.2 to 0.6	92.6 (3000)	105
31	$CoWO_3$ and $CoWO_4$	Microwave irradiation	Nickel mesh	Nanoporous	2 M KOH	45	0.0 to 0.6	-	106
32	$CoWO_4/Co_3O_4$	Hydrothermal	Nickel foam	Nanocones	3M KOH	3560	-0.2 to 0.5	90.5 (5000)	107
33	$CoWO_4$	Hydrothermal	Carbon cloth	Nanosphere	3M KOH	1443	0 to 0.6	-	108
	CNT- $CoWO_4$		Carbon cloth	Nanosphere		1486	0 to 0.6	(4500)	
34	$CoWO_4$	Sol-gel	Nickel foam	Nanoparticles	3M KOH	76	0 to 0.45	98 (1000)	109
35	$CoWO_4/Ni$	wet chemical	Nickel foam	Spherical nanoparticles	6M KOH	271	-0.1 to 0.5	86.4 (1500)	110

36	$Ni_{(1-x)}Co_{(x)}WO_4$	Hydrothermal	Nickel foam	Spherical nanoparticles	3M KOH	636.8	0 to 0.5	92 (10000)	111
37	MnO_2/$CoWO_4$/ NCNO	Co-precipitation	Nickel foam	Spherical nanoparticles	6M KOH	209	-0.4 to 0.65	96 (3000)	112
38	$Li_2Co(WO_4)_2$	Self-combustion	Nickel foam	Spherical nanoparticles	6 M KOH	1192	-0.3 to 0.5 V	91.8 (10000)	113

Literature survey based on cobalt tungsten oxide show that metal tungstate materials are used for fabrication of supercapacitors.

1.2.2 Literature survey of cobalt tungsten oxide based oxygen evolution reaction:

Table 1.2 contains cobalt tungsten oxide and their deposition methods along with their oxygen evolution reaction performance.

Sr. No.	Material	Electrolyte	Method	Substrate	Overpotential @ 10 mA cm^{-2} (mV)	Tafel slope (mV/ decade)	Stability (h)	Remark	Ref.
1	$CoWO_4$ and $NiWO_4$	1 M KOH	Co-precipitation	Glassy carbon	255	47.6	10	The electrode kinetic parameters, Tafel slope and the reaction order for the OER determined from the EIS study are very close to those obtained from the steady-state dc polarization techniques.	114
2	$CoWO_4$	1 M KOH	Complexation-precipitation	Glassy carbon	450	82	10	Bifunctional performances of $CoWO_4$ nano-cubes are explored for water electrolysis in an alkaline medium	115
3	$Co_{1-(x+y)}Fe_x Mn_yWO_4$	1 M KOH	Hydrothermal	Glassy carbon	810	83	10	Fe and Mn codoped $CoWO_4$ is a highly efficient electrocatalyst for water splitting.	116
4	CTOHH	1 M KOH	Microwave heating	CC	355	47.5	12	CTOHH-DNA was prepared for the first time by utilizing a greener bio-scaffold DNA using microwave heating conditions within short time duration.	117
5	CoFeWOx	1 M KOH	Electrodepositoin	Nickel foam	300	32	10	Trimetallic Co–Fe–W oxyhydroxides enriched with Co_3.	118
6	$CoWO_4$	1 M KOH	Co-precipitation	glassy carbon	250	50	12	Amorphous Fe-doped	119

								$CoWO_4$ is a highly efficient bifunctional electrocatalyst for the overall water splitting under alkaline conditions	
7	$CoWO_4$	1 M KOH	Hydrothermal	glassy carbon	295	30.5	12	oxygen defect $CoWO_{4-x}$ nanoparticles with a diameter of 8 nm were deposited on carbon black ($CoWO_{4-x}$@C).	120
8	$Co_{0.5}Fe_{0.5}WO_4$	1 M KOH	Hydrothermal	glassy carbon	331	36.8	10	Highly active catalyst for the OER, consisting of wolframite-type ternary tungstates with iron and cobalt.	121
9	$CoWO_4$/NGO	0.5 M KOH	Hydrothermal	glassy carbon	189	-	12	Starting from $CoCl_2 \cdot 6H_2O$ and $Na_2WO_4 \cdot 2H_2O$ two different nanoparticles of $CoWO_4$: the nanodots and nanorods are synthesized	122
10	$CoWO_4$	0.2 M Na_2WO_4	Dip coating	ITO	115	110	13	$CoWO_4$ as a water oxidation catalyst	123
11	$CoMo_xO_y/Co_3O_4$(M=Mo,W,V)	1 M KOH	Hydrothermal	Nickel foam	219	84.7	10	The as-prepared electrocatalysts exhibit catalytic activity toward the OER with overpotentials of 219 mV, 259 mV and 268 mV to produce a current density of 10 mA cm^{-2} in alkaline	124

								electrolyte which is superior to the commercial RuO_2 catalyst.	
12	$CoMoO_4$	0.1 M KOH	Precipitation	FTO	680	110	10	Tungsten-doped cobalt molybdenum oxides (W-$CoMoO_4$) is investigated as electrocatalysts for Oxygen evolution reaction in alkaline media for the first time.	125
13	$CoWO_4$	1 M KOH	Soft template	-	448	61	10	Highly ordered cobalt tungstate mesoporous material was synthesized by soft template method with the aid of buffer solution for the first	126
14	$CoMnWO_4$	0.1 M KOH	Hydrothermal	Nickel mesh	400	-	10	The density functional theory revealed that the substitution of Mn in $CoWO_4$ elevate the 3d metal d band center closer to the Fermi energy and hence ease the electron transfer to facilitate ORR and OER.	127
15	$CoWO_4$	0.1 M NaOH	Electrospining	Carbon paper	306	72	10	$CoWO_4$ NF-based sensor presented a remarkable electrocatalytic activity towards H_2O_2 oxidation, including lower redox potential	128

16	$CoWO_4$	1M KOH	Molten salt	Glassy carbon electrode	450	87	10	Bifunctional performances of $CoWO_4$ nano-cubes are explored for water electrolysis in an alkaline medium (1.0 M KOH) under various atmospheres (N_2, air and O_2).	129
17	$CoWO_4$	0.1 M NaOH	Electrodeposition	Ni mesh	970	-	10	High overpotential was attributed to the instability of oxygen radicals formed during the oxygen evolution.	130
18	$CoFeWO_4$	1M KOH	Co-precipitation	Glassy carbon	327	53	10	Role of local structural distortion played in OER process was discussed.	131
19	WO_3@$CoWO_4$	0.1 M KOH	Hydrothermal	Glassy carbon	380	-	10	Two-dimensional (2D) bilayer nanosheets of WO_3@$CoWO_4$ were used as highly efficient catalysts for enhanced photo, electro and photoelectro-chemical oxygen evolution reactions (OERs).	132
20	$CoWO_4$	1 M KOH	Solvothermal	Carbon cloth	310	-	10	The excellent OER response was observed for XWO_4 nanostructures synthesized at optimum processing condition.	133

A literature study reveals that, only a few reports are available on cobalt tungstate preparation by simple chemical successive ionic layer adsorption and reaction (SILAR) method. So, our aim is to prepare cobalt tungstate using chemical method SILAR. This is promising method for the preparation of metal tungstate thin films over stainless steel substrate. This method is probably easiest, low cost, and suitable to prepare large-area, binder-free thin film electrodes for supercapacitor and OER applications.

1.3 Orientation and purpose of the thesis:

The transition metal oxides have been utilized in the various applications due to their different physical and chemical properties. $CoWO_4$ is environment friendly and highly stable p-type semiconductor transition metal oxide which is used in various applications such as OER activity, gas sensors, catalysis, SCs, batteries, electromagnetic and luminescence devices, and biomedicine. $CoWO_4$ have properties such as various oxidation states, electrochemical stability, and high reduction potential. Due to this properties, $CoWO_4$ are used in supercapacitors. In recent years, researchers all over the world concentrated on improvement of electrochemical performance of supercapacitor by means of enhanced energy density, power density, long cycle life and preparation of cost effective electrodes, which are the important four pillars of energy storage systems. A supercapacitor device with outstanding electrochemical activity and low cost may raises its usage over widespread applications. The active electrode material and electrolyte are key factors and influence the performance of supercapacitor in terms of capacitance and energy density. However, the energy densities of supercapacitor are still low; to overcome the challenges in field of supercapacitor, have to develop efficient active material with high capacitance. Previously reported major types of supercapacitor materials are carbon, conducting polymers, metal oxides and transition metal tungstates. Recently, transition metal tungstate attract more attention among those active materials for energy storage applications.

The fundamental requirements for supercapacitor electrodes include high electrical conductivity, chemical and mechanical stability, high surface area with appropriate pore sizes optimal for an electrolyte. To improve electrical conductivity of the electrode binder-free deposition approach is generally used for thin film electrode preparation.

The present work is focused on synthesis of $CoWO_4$ thin films by simple successive ionic layer adsorption and reaction method. Offers required material properties such as crystal structure, surface morphology and film thickness. Fabrication of flexible solid state supercapacitor device using $CoWO_4$@rGO composite thin films as an active cathode material with polyvinyl alcohol-potassium hydroxide (PVA-KOH) gel electrolyte is carried out. The activity of electrode material and usefulness of electrolytes are investigated by fabricating solid state devices. The performance of asymmetric device is studied in terms of capacitance, energy and power densities, and cyclic stability. Finally, conclusions are assessed on the basis of the performance of $CoWO_4$@rGO based devices.

The physical and chemical properties of prepared thin films studied by various characterizations. The phase identification of material is carried out by X-ray diffraction (XRD) technique. Chemical bonding in material is studied by Fourier Transform Infrared spectroscopy analysis (FT-IR). The surface morphology of prepared thin films is evaluated by Field Emission Scanning Electron Microscopy (FE-SEM) technique. Elemental composition of thin films is detected by Energy-Dispersive X-ray Spectroscopy (EDS) technique. Material confirmation, available oxidation states and chemical composition of thin film are done with X-ray Photoelectron Spectroscopy (XPS) technique. The supercapacitive properties of prepared thin films are investigated by cyclic voltammetry (CV), galvanostatic charge-discharge (GCD) and electrochemical impedance spectroscopy (EIS) techniques. Three electrode system used for the electrochemical study in 1 M KOH electrolyte, consists of $CoWO_4$ thin film used as working electrode, platinum as a counter and saturated calomel electrode (SCE) as a reference electrode. Furthermore, the performance of prepared thin films evaluated in terms of C_s and cyclic life.

It has been well documented that to store intermittent energy from renewable sources, we need an efficient energy carrier. In this scenario hydrogen economy is one of the promising solutions. But due to the sluggish kinetics, OER becomes a bottleneck for large scale hydrogen production. To increase the efficiency of water splitting, anodic half reaction (OER) must be accelerated. The high cost and low abundance of state-of-the-art OER catalyst materials kept them away from industrial applications. The presence of unfilled d-orbital in the 3d transition elements makes them a center of attraction in the field of electrochemical water splitting. Up to now, numerous materials containing these elements have been reported. Initially, oxides of these transition metals are considered promising OER catalysts due to their ability to form intermediate bonds with reactants easily. But the low value of their intrinsic conductivity makes them less compatible with practical application. On the other side, the sufficiently high conductivity of transition metal tungstate makes them promising candidates. It is observed that the binary and ternary metal tungstates are more active than primary metal tungstate.

The recent trend suggests that the composites of these metal tungstates with 3-D carbon structure (graphene oxide) enhances the mass and charge transport efficiency. This helps to improve catalytic activity via increasing electronic conductivity, surface area and mechanical strength. $CoWO_4$ is wildly studied materials in the field of supercapacitor but are rarely explored for electrochemical water splitting. Metal tungstate will give excellent OER performance, which can be further enhanced by compositing it with rGO. The preparation of catalyst material in the form of thin film is more admirable than the bulk form in the view of practical application. The physical methods of thin film deposition are expensive and put limitations on choice of substrates. Therefore, the simple successive ionic layer adsorption and reaction (SILAR) method is more appreciable for the deposition of thin films of various materials. Hence, the present study is focused on the synthesis of $CoWO_4$/rGO composite thin films using SILAR method on stainless steel (SS) substrate. To minimize the overpotential required for OER is the main intention of the present study. A composite thin film electrocatalyst of $CoWO_4$ with rGO is synthesized on SS substrates by SILAR method. Various characterization techniques such as XRD, Raman, FE-SEM and TEM are used to study material properties. The electrochemical performance of electrocatalysts towards OER is tested in three electrode system. Linear sweep voltammetry (LSV), CV, chronopotentiometry and EIS techniques are used to evaluate different electrocatalysts.

1.4 References:

[1] G. Eranna, B. Joshi, D. Runthal, R. Gupta, Crit. Rev. Solid State Mater. Sci., 29 (2004) 111-188.

[2] X. Wei, E. Li, Y. Guan, Y. Chong, J. Electromag. Wave, 23 (2009) 925-934.

[3] W. Martin and J. Brodd, Chem. Rev., 104 (2004) 4245-4270.

[4] H. Omanda, T. Brousse, C. Marhi, D. Schleich, J. Electrochem. Soc., 151 (2004) 922-929.

[5] J. Tarascon, and M. Armand, Nature, 414 (2001) 171-179.

[6] L. Zhang, and X. Zhao, Chem. Soc. Rev., 38 (2009) 2520-2531.

[7] C. Du, and N. Pan, J. Power Sources, 160 (2006) 1487-1494.

[8] E. Frackowiak, and F. Beguin, Carbon, 39 (2001) 937-950.

[9] X. Zhao, B. Sanchez, P. Dobson, P. Grant, Nanoscale, 3 (2011) 839-855.

[10] M. Dupont, A. Hollenkamp, S. Donne, J. Electrochem. Soc., 161 (2014) 648-656.

[11] H. Wang, and L. Pilon, J. Phys. Chem. C, 115 (2011) 16711-16719-.

[12] A. Burke, J. Power Sources, 91 (2000) 37-50.

[13] Y. Wang, and Y. Xia, Electrochim. Acta, 51 (2006) 3193-3384.

[14] A. Laforgue, P. Simon, J. Fauvarque, M. Mastragostino, F. Soavi, J. Sarrau, P. Lailler, M. Conte, E. Rossi, S. Saguatti, J. Electrochem. Soc., 150 (2003) 645-651.

[15] A. Rufer, and P. Barrade, IEEE Trans. Ind. Appl., 38 (2002) 1151-1159.

[16] G. Gund, D. Dubal, S. Shinde, C. Lokhande, ACS Appl. Mater. Interfaces, 6 (2014) 3176-3188.

[17] D. Dubal, J. Kim, Y. Kim, R. Holze, C. Lokhande, W. Kim, Energy Technol., 2 (2014) 325-341.

[18] P. Deshmukh, S. Pusawale, R. Bulakhe, C. Lokhande, Bull. Mate. Sci., 36 (2013) 1171-1176.

[19] S. Kulkarni, A. Jagadale, V. Kumbhar, R. Bulakhe, S. Joshi, C. Lokhande, Int. J. Hydrogen Energy, 38 (2010) 4046-4053.

[20] D. Dubal, G. Gund, C. Lokhande, R. Holze, ACS Appl. Mater. Interfaces, 5 (2013) 2446-2454.

[21] G. Gund, D. Dubal, B. Patil, S. Shinde, C. Lokhande, Electrochim. Acta, 92 (2013) 205-215.

[22] J. Wang and X. Sun, Energy Environ. Sci., 5 (2012), 5163-5185.

[23] G. A. Olah, G. K. S. Prakash, A. Goeppert, J. Am. Chem. Soc., 133 (2011) 12881-12898.

[24] A. Woodward, K. Smith, D. Campbell-Lendrum, D. Chadee, Y. Honda, Q. Liu, J. Olwoch, B. Revich, R. Sauerborn, Z. Chafe, U. Confalonieri, A. Haines, Lancet., 383 (2014) 1185-1189.

[25] T. Cook, D. Dogutan, S. Reece, Y. Surendranath, T. Teets, D. Nocera, Chem. Rev., 110 (2010) 6474-6502.

[26] P. Zhang, J. Zhang, J. Gong, Chem. Soc. Rev., 43 (2014) 4395-4422.

[27] P. Katkar, S. Marje, S. Kale, A. Lokhande, C. Lokhande, U. Patil, Cryst. Eng. Comm., 21 (2019) 884-893.

[28] C. Acar, I. Dincer, 1.13 Hydrogen energy, Volume 1: Energy Fundamentals, Comprehensive Energy Systems, Elsevier (2018) 568-605.

[29] P2G System technology development aiming at building a CO_2-free hydrogen society, ECS Meet. Abstr., 37 (2019) 1703.

[30] T. Yoshida, K. Kojima, Toyota MIRAI fuel cell vehicle and progress toward a future hydrogen society, Electrochem. Soc. Interface. 24 (2015) 45-49.

[31] D. Wang, Y. Xu, W. Sun, X. Guo, L. Yang, F. Wang, Z. Yang, Electrochim. Acta, 337 (2020) 1-10.

[32] B. Tan, K. Klabunde, P. Sherwood, J. Am. Chem. Soc., 113 (1991) 855-861.

[33] S. Kale, A. Lokhande, R. Pujari, C. Lokhande, J. Colloid Interface Sci., 532 (2018) 491-499.

[34] S. Pujari, S. Kadam, Y. Ma, P. Katkar, S. Marje, S. Khalate, A. Lokhande, U. Patil, J. Electron. Mater., 49 (2020) 3890-3901.

[35] Z. Lv, N. Mahmood, M. Tahir, L. Pan, X. Zhang, J. Zou, Nanoscale., 8 (2016) 18250-18269.

[36] P. Li, and H. Zeng, Chem. Commun., 53 (2017) 6025-6028.

[37] Z. Wang, D. Xu, J. Xu, X. B. Zhang, Chem. Soc. Rev. 43 (2014) 7746-7786.

[38] N. Suen, S. Hung, Q. Quan, N. Zhang, Y. Xu, H. Chen, Chem. Soc. Rev., 46 (2017) 337-365.

[39] M. Fang, G. Dong, R. Wei, J. Ho, Adv. Energy Mater., 7 (2017) 1700559-1700583.

[40] M. Gong, Y. Li, H. Wang, Y. Liang, J. Z. Wu, J. Zhou, J. Wang, T. Regier, F. Wei, H. Dai, J. Am. Chem. Soc., 135 (2013) 8452-8455.

[41] M. Tahir, N. Mahmood, J. Zhu, A. Mahmood, F. Butt, S. Rizwan, I. Aslam, M. Tanveer, F. Idrees, I. Shakir, C. Cao, Y. Hou, Sci. Rep. 5, (2015) 12389-12399.

[42] J. Montoya, L. Seitz, P. Chakthranont, A. Vojvodic, T. Jaramillo, J. Nørskov, Nat. Mater., 16 (2016) 70-81.

[43] C. Wei, R. R. Rao, J. Peng, B. Huang, I. E. L. Stephens, M. Risch, Z. J. Xu, Y. Shao-Horn, Adv. Mater., 31 (2019) 1806296-1806320.

[44] J. Hu, C. Zhang, X. Meng, H. Lin, C. Hu, X. Long, S. Yang, J. Mater. Chem. A, 5 (2017) 5995-6012.

[45] Y. Guo, J. Tang, Z. Wang, Y. Sugahara, Y. Yamauchi, Small, 14 (2018) 1802442-1802450.

[46] K. Xu, P. Chen, X. Li, Y. Tong, H. Ding, X. Wu, W. Chu, Z. Peng, C. Wu, Y. Xie, J. Am. Chem. Soc., 137 (2015) 4119-4125.

[47] L. Han, S. Dong, E. Wang, Adv. Mater., 28 (2016) 9266-9291.

[48] L. Krishtalik, Electrochim. Acta, 26 (1981) 329-337.

[49] Y. Tong, P. Chen, T. Zhou, K. Xu, W. Chu, C. Wu, Y. Xie, Angew. Chemie Int., 56 (2017) 7121-7125.

[50] C. Ling, L. Qin, L. Zhou, H. Jia, RSC Adv., 4 (2014) 24692-24697.

[51] Y. Li, F. Li, X. Meng, S. Li, J. Zeng, Y. Chen, ACS Catal., 8 (2018) 1913-1920.

[52] T. Wang, M. Liu, H. Ma, Energy technol., 5 (2020) 1900749-1900769.

[53] D. Malavekar, V. Lokhande, D. Patil, S. Kale, U. Patil, T. Ji, C. Lokhande, J. Colloid Interface Sci., 609 (2022) 734-745.

[54] M. Athar, M. Fiaz, M. Asim Farid, M. Tahir, M. Adnan Asghar, S. Hassan, and M. Hasan, ACS Omega, 6 (2021) 7334-7341.

[55] R. Karthika, M. Shafia, S. Chen, R. Sukanya, G. Dhakal, S. Jae-Jin, J Taiwan Inst. Chem. Eng., 126 (2021) 145-153.

[56] X. Du, Q. Shao, X. Zhang, Int. J. Hydrog. Energy, 44 (2019) 2883-2888.

[57] S. Chidambaram, K. Ramachandran, M. Gaidi, K. Daoudi, M. Natarajamoorthy, J. Mater. Sci.: Mater. Electron., 33 (2022) 9134-9143.

[58] M. Nakayama, A. Takeda, H. Maruyamaa, V. Kumbhar, O. Crosnier, Electrochem. commun., 120 (2020) 106834-106840.

[59] S. Swathi, R. Yuvakkumar, P. Senthil Kumar, G. Ravi, D. Velauthapillai, Fuel, 306 (2021) 121781-121789.

[60] V. Srirapu A. Kumar, P. Srivastava, R. Singh, A. Sinha, Electrochim. Acta, 209 (2016) 75-84.

[61] W. Low, P. Khiew, S. Lim, C. Siong, E. Ezeigwe, J. Alloys Compd., 775 (2019) 1324-1356.

[62] M. Denk, D. Kuhness, M. Wagner, S. Surnev, F. Negreiors, L. Sementa, G. Barcaro, I. Vobornik, A. Fortunelli, F. Netzer, ACS Nano, 8 (2014) 347-3954

[63] G. Zhang and X. Lou, Adv. Mater., 25 (2013) 976-979.

[64] J. Zhang, F. Lu, J. Chenq, X. Zhang, ACS Appl. Mater. Interface, 7 (2015) 17630-17640.

[65] G. He, J. Li, W. Li, B. Li, N. Noor, K. Xu, J. Hu, I. Parkin, J. Mater. Chem., A, 3 (2015) 14272-14278.

[66] N. Bretesche, O. Crosnier, C. Payen, F. Favier, T. Brousse, Electrochem. Commun., 57 (2015) 61-64.

[67] D. Cai, D. Wang, B. Liu, Y. Wang, Y. Liu, L. Wang, H. Li, H. Huang, Q. Liu, T. Wang, ACS Appl. Mater. Interfaces, 5 (2013) 12905-12910

[68] S. Ede, A. Ramadoss, U. Nithiyanantham, S. Anantharaj, S. Kundu, Inorga. Chem., 54 (2015) 3851-3863

[69] A. Sobhani-Nasab, M. Rahimi-Nasrabadi, H. Naderi, V. Pourmohamadian, F. Ahmadi, M. Ganjal, H. Ehrlch, Ultrason. Sonochem., 45 (2018) 189-196.

[70] X. Xu, L. Pei, Y. Yang, J. Shen, M. Ye, J. Alloys Compd., 654 (2016) 23-31.

[71] C. Ling, L. Q. Zhou, H. Jia, RSC Adv., 4 (2014) 24692-24697.

[72] M. Zhang, H. Fan, N. Zhao, H. Peng, X. Ren, W. Wang, H. Li, G. Chen, Y. Zhu, X. Jiang, P. Wu, Chem. Eng. J., 347 (2018) 291-300.

[73] A. Li. Y. Tu, Y. Zhu, D. Li, W. Zhou, X. Zhu, L. Feng, Int. J. Electrochem. Sci., 12 (2017) 5646-5656.

[74] A. Patil, G. Lohar, V. Fulari, J. Mater. Sci: Mater Electron., 27 (2016) 9550-9557.

[75] Y. Wang, C. Shen, L. Niu, Z. Sun, F. Ruan, M. Xu, S. Shan, C. Li, X. Liu, Y. Gong, Mater. Chem. Phys., 182 (2016) 1-8.

[76] V. Lokhande and T. Ji, Adv. Sc. Technol. Lett., 139 (2016) 409-413.

[77] S. Chen, G. Yang, Y. Jia, H. Zheng, Chem electro chem, 3 (2016) 1490-1496

[78] A. Li, Y. Tu, Y. Zhu, D. Li, W. Zhou, X. Zhu, L. Feng, Int. J. Electrochem. Sci., 12 (2017) 5646-5656.

[79] K. Ding, X. Zhang, J. Li, P. Yang, and X. Cheng, Chem Electro Chem, 4 (2017) 3011-3017.

[80] Y. Wang, C. Shen, L. Niu, Z. Sun, Mater. Chem. Phys., 182 (2016) 394-401.

[81] H. Naderi, A. Nasab, M. Rahimi-Nasrabadi, M. Ganjali, Appl. Surf. Sci., 423 (2017) 1025-1034.

[82] G. He, J. Li, W. Li, B. Li, N. Noor, K. Xu, J. Mater.Chem. A, 3 (2015) 14272-14278.

[83] X. Xing, Y. Gui, G. Zhang, C. Song, Electrochim. Acta, 157 (2015) 15-22.

[84] X. Xu, J. Shen, N. Li, M. Ye, Electrochim. Acta, 150 (2014) 23-24.

[85] K. Adib, M. Nasrabadi, Z. Rezvani, S. Pourmortazavi, F. Ahmadi, H. Naderi,

M. Ganjali, J Mater. Sci: Mater Electron, 27 (2016) 4541–4550.

[86] M. Zhang, H. Fan, N. Zhao, H. Peng, X. Ren, W. Wang, H. Li, G. Chen, Y. Zhu, X. Jiang, P. Wu, Chem. Eng. J., 347 (2018) 291-300

[87] A. Singh, and A. Ojha, AIP Conf. Proce., 2244 (2020) 1-4.

[88] H. Ma, Z. Shen, Z. Peng, S. Guan, X. Fu, J. Alloys Compd., 845 (2020) 155654-155665.

[89] S. Jha, S. Mehta, E. Chen, S. Sankar, S. Kundu, H. Liang, Mater. Adv., 1 (2020) 2124-2135.

[90] J. Hou, J. Gao, L. Kong, J. Alloys Compd., 3 (2020) 11470-11479.

[91] D. Chu, D. Guo, B. Xiao, L. Tan, H. Ma, H. Pang, X. Wang, Y. Jiang, Chem. Asian J., 15 (2020) 1750-1755.

[92] S. Sanati, Z. Rezvani, R. Abazari, Z. Houc, H. Da, New J. Chem., 43 (2019) 15240-15248.

[93] J. Ge, J. Wu, J. Dong, J. Jia, B. Ye, S. Jiang, J. Zeng, Q. Bao, Chem Electro Chem., 5 (2018) 1047-1055.

[94] M. Ikrama, Y. Javed, N. Shad, M. Sajid, M. Irfan, A. Munawar, T. Hussain, M. Imrang, D. Hussain, J. Alloys Compd., 878 (2021) 160314-160323.

[95] A. Rajpurohit, N. Punde, C. Rawool, A. Srivastava, Chem. Eng. Sci., 371 (2019) 679-692.

[96] B. Huang, H. Wang, S. Liang, H. Qin, Y. Li, Z. Luo, C. Zhao, L. Xie, L. Chen, Energy Storage Mater., 32 (2020) 105-144.

[97] T. Anitha, A. Reddy, R. Vinodh, H. Kimb, Y. Cho, J. Energy Storage, 30 (2020) 101483-101491.

[98] R. Kumar, S. Karuppuchamy, J. Alloys Compd., 674 (2016) 384-391.

[99] W. Low, P. Khiew, S. Lim, C. Siong, E. Ezeigwe, J. Alloys Compd., 775 (2019) 1324-1356.

[100] C. Lamiel, Y. Lee, M. Cho, D. Tuma, J. Shim, J. Colloid Interface Sci., 507 (2017) 300-309.

[101] M. Zhang, H. Fan, X. Ren, N. Zhao, H. Peng, C. Wang, X. Wu, G. Dong, C. Long, W. Wang, Y. Gao, L. Ma, P. Wu, H. Li, X. Jiang, J. Power Sources, 418 (2019) 202-210.

[102] V. Lokhande, S. Lee, A. Lokhande, J. Kim, T. Ji, Mater. Chem. Phys., 211 (2018) 214-224.

[103] H. Azevêdo, R. Raimundo, L. Ferreira, M. Silva, M. Morales, D. Macedo, U. Gomes, D. Cavalcante, Mater. Chem. Phys., 242 (2020) 122544-122577.

[104] M. Mousavi and A. Yangjeh, Mater. Res. Bull., 105 (2018)159-171.

[105] A. Krishnapandi, B. Muthukutty, S. Chen, M. Selvaganapathy, Microchem. J., 159 (2020) 105381-105408.

[106] S. Shanmugapriya, S. Surendran, V. Nithya, P. Saravanan, R. Selvan, Mater. Sci. Eng. B, 214 (2016) 57-67.

[107] Z. Nie, W. Ding, B. Zhou, R. Huang, results in materials, 6 (2020) 100094-100104.

[108] A. Sobhani-Nasab, M. Rahimi-Nasrabadi, H. Naderi, V. Pourmohamadian, F. Ahmadi, M. Ganjali, H. Ehrlich, Ultrason. Sonochemistry, 45 (2018) 189-196.

[109] M. Mohamed, S. Shenoy, D. Bhat, Mater. Chem. Phys., 208 (2018) 112-122.

[110] K. Thiagarajan, D. Balaji, J. Madhavan, J. Theerthagiri, S. Lee, K. Kwon, M. Choi, Nanomaterials, 10 (2020) 2195-2207.

[111] V. Chukwuike, S. Sankar, S. Kundu, R. Barik, Corcon, 1 (2019) 1-9.

[112] S. Prabhu, C. Balaji, M. Navaneethan, M. Selvaraj, N. Anandhan, D. Sivaganesh, S. Saravanakumar, P. Sivakumar, R. Ramesh, J. Alloys Compd., 875 (2021) 160066-160076 .

[113] E. Sohouli, K. Adib, B. Maddah, M. Najafi, Ceram. Int., 48 (2022) 295-303.

[114] V. Srirapu, A. Kumar, N. Kumari and R. Singh, Indian J. Chem**.,** 57A (2018) 1100-1105.

[115] S. Alshehri, J. Ahmed, T. Ahamad, P. Arunachalam, T. Ahmad and A. Khan, RSC Adv., 7 (2017) 45615-45623.

[116] M. Athar, M. Fiaz, M. Farid, M. Tahir, M. Asghar, S. Hassan, and M. Hasan, ACS Omega, 6 (2021) 7334-7341.

[117] S. Kumaravel, P. Thiruvengetam, S. Ede, K. Karthick, S. Anantharaj, S. Sankar, and S. Kundu, Dalton Trans., 48 (2019) 17117-171132.

[118] J. Chen, H. Li, Z. Yu, C. Liu, Z. Yuan, C. Wang, S. Zhao, G. Henkelman, S. Li, Li Wei, and Y. Chen, Adv. Energy Mater., 10 (2020) 2002593-2002604.

[119] J. Wu, R. Xie, X. Hu, Z. Nie, Y. Shi, Y. Yu and N. Yang, J. Mater. Chem. A., 9 (2021) 9753-9760.

[120] F. Luo, R. Xu, S. Ma, Q. Zhang, H. Hu, K. Qu, S. Xiao, Z. Yang, W. Cai, Appl. Catal. B., 259 (2019) 118090-118097.

[121] M. Nakayama, A. Takeda, H. Maruyama, V. Kumbhar, Electrochem. Commun., 120 (2020) 106834-106840.

[122] V. Srirapu, A. Kumar, P. Srivastava, R. Singh, A. Sinha, Electrochim. Acta, 209 (2016) 75-84.

[123] Z. Nie, W. Ding, B. Zhou, R. Huang, Results and materials, 6 (2020) 100094-100104.

[124] H. Jia, J. Stark, L. Zhou, C. Ling, T. Sekito, and Z. Markin, RSC Advances, 2 (2012) 10874-10881.

[125] L. Liu, Y. Ou, D. Sun, Chem. Eng. J., 426 (2021) 130063-130100.

[126] D. Tantraviwat, S. Anuchai, K. Ounnunkad, S. Saipanya, N. Aroonyadet, G. Rujijanagul, B. Inceesungvorn, J. Mater. Sci.: Mater. Electron., 29 (2018) 13103-13111.

[127] H. Xiao, T. Liang, X. Zhang, P. Liao, M. Liu, Nanotechnology, 31 (2020) 1-13.

[128] G. Karkera, T. Sarkar, M. Bharadwaj and A. Prakash, Chem Cat Chem, 9 (2017) 3681-3690.

[129] S. Liao, S. Lu, S. Bao, Y. Yu and L. Yu, Chem Electro Chem, 2 (2015) 2061-2070.

[130] S. Alshehri, J. Ahmad, T. Ahmed, P. Arunachalam, T. Ahamad, RSC Adv., 7 (2017) 45615-45623.

[131] C. Ling, L. Zhou and H. Jia, RSC Adv., 4 (2014) 24692-24697.

[132] W. Shao, Y. Xia, X. Luo, L. Bai, J. Zhang, G. Sun, Nano Energy, 50 (2018) 717-722.

[133] H. Zhang, W. Tian, Y. Li, H. Sun, M. Tadé, and S. Wang, Mate. Che. A, 6 (2018) 6265-6272.

CHAPTER-2

Basic of SILAR Method and Thin Film Characterization Techniques

CHAPTER 2

Basic of SILAR Method and Thin Film Characterization Techniques

2.1 Introduction:

Material science is a branch which deals with the study of properties of materials for various applications. Different properties of materials include their physical, chemical, electrical, electronic, optical and thermal etc. The performance of resultant material greatly rely on these properties in turn seeking considerable research attention from scientific community. As a consequence, development of sophisticated synthesis methods for taking control over these properties as well as required instrumentation to evaluate these properties has accelerated the research in the field of material science [1]. It is well known that last decade has experienced the entrance of various computer based simulations and softwares that have taken the research to the next level which further helps to study the properties of materials through computational method [2]. However, current research trend is vastly focused on the development of various nanostructured materials in the form of thin films with taking control over their physico-chemical characterizations to achieve desired functionalities. The control over these physico-chemical properties have enabled the applications of thin films into almost every application including supercapacitor, electrocatalysis, photocatalysis, sensing, photovoltaic as well as different biological applications [3]. The performance of the specific application depends on the selectivity of the material as well as the synthesis method and the post synthesis treatments. The suitable choice of the material and synthesis method results into the modification of various properties that results into the enhanced performance. Most of technologies make use of the fact that many properties are thickness dependent can be effectively controlled by altering thickness of the thin film. Thickness of thin films range from few nanometers to several micrometers. However, there is no proper defined thickness below which a coating can be called as thin films. This might be because, the thickness dependent properties changes from materials to materials. But the properties of any material at the nanoscale possess far better properties than their bulk counterparts. This is maybe because at nanoscale level the reduction in particle size ultimately affects the structural, morphological, optical as well as electrical properties. One of the effective methods to control the thickness of the thin films is the selection of appropriate deposition method. Specific deposition method helps to induce crystallinity, desired morphology as well as surface area etc [4, 5].

Nanostructured materials have been synthesized by various deposition methods in order to achieve control over the thin film properties. Thin film deposition methods including chemical bath deposition, SILAR, spin coating, dip coating, electrodeposition, sputtering, chemical vapour deposition, physical vapour deposition, electron beam evaporation, hydrothermal, anodization, molecular beam epitaxy, liquid phase epitaxy, sol gel etc. have found considerable attention for the deposition of various materials. These deposition methods are broadly divided into two major groups viz. physical deposition method and chemical deposition methods as shown in chart 2.1. Physical methods mainly rely on the conversion of solid material into gas phase that later deposits on the substrates place at the top of the deposition chamber. These methods require highly sophisticated instrumentation, well maintained environment and highly trained person for the operation eventually increasing the cost effectiveness of the thin film deposition process. On the other hand, chemical deposition methods are based on the reaction of precursors in mostly aqueous media and the deposition of the particles at the solid-liquid interface on the substrate. The chemical methods benefit in terms of inexpensiveness, low working temperature, large area deposition as well as flexibility to use wide variety of substrates etc [6-8].

The deposition process is just half way done. The second important task is to characterize the deposited material using various structural and elemental characterization techniques that supports the theoretical data with experimental proofs. To verify the formation of desired material as well as to study different properties of the materials, number of analytical techniques are available that confirms the material properties. For instance, formation of the material can be confirmed by X-ray diffraction, morphological study can be done using SEM, TEM and AFM, electrical study can be done using two probe or four probe method, chemical study can be carried out using X-ray photoelectron spectroscopy as well as Fourier transform infrared spectroscopy. Surface area can be analyzed by BET technique and Barrett-Joyner-Halenda (BJH) technique. Electrochemical study can be done using electrochemical workstation etc [9].

2.2 Basics of Successive Ionic Layer Adsorption and Reaction (SILAR) method:

The SILAR method is one of the favourable chemical methods for the deposition of variety of thin films. SILAR finds best advantageous due to the excellent control over reaction parameters that helps one to tune the properties of the resultant material. This method was first reported by Ristov et al. in 1985 [10] and the name SILAR was first given by Nicolau et al. [11]. This method allows deposition of various chemical compounds as well as their composite films. This method is also known as modified version of chemical bath deposition method.

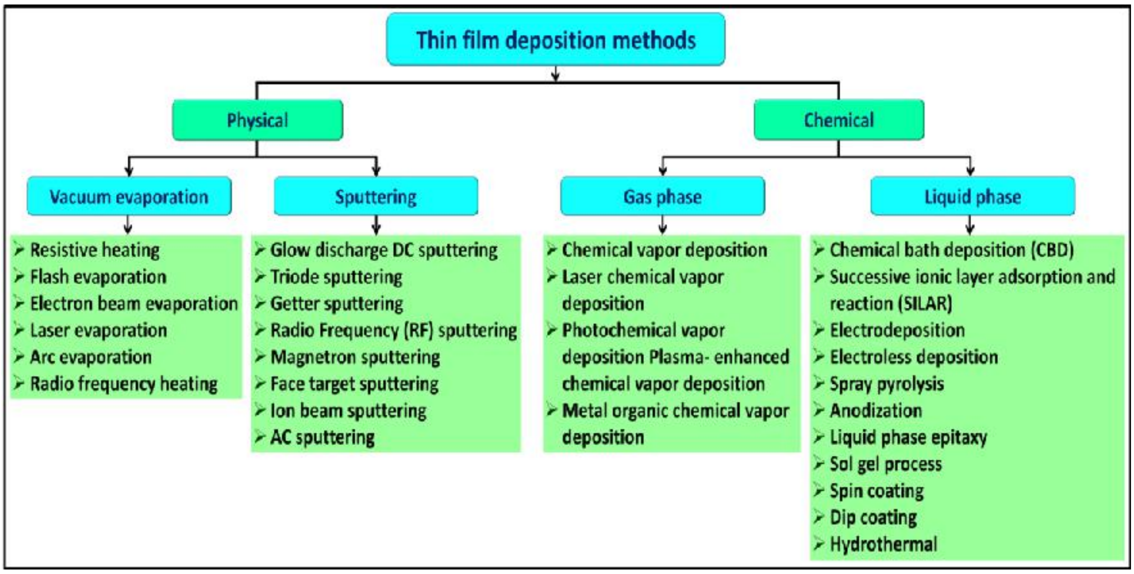

Chart 2.1: General classification of thin film deposition methods.

The basic representation of four beakers SILAR method is shown in Figure 2.1. The different processes involved in SILAR method are elaborated below.

(a) Adsoprtion:

This is the first step of SILAR reaction. The beaker containing cations are placed at the first place where a substrate upon dipping into the beaker adsorbs cations onto its surface. When cations are adsorbed on the substrate, formation of Helmohltz double layer takes place which contains positively charged ions at the inner side and negatively charged ions at the outer side. These layers are loosely bound by Van Der Waals force.

As the acronym implies, the SILAR method is based on the adsorption of a layer of ionic species onto a surface, followed by a reaction triggered by a successive adsorption of a different ionic species. This reaction leads to the formation of an insoluble product, which constitute the thin-film coating. The process is then repeated to increase the thickness of the deposited layer. In order to carefully control the deposition process, a SILAR setup employs a series of steps which are depicted in Figure 2.1.

Solution A is the primary ionic solution which in many instances is an aqueous solution of metal cations, while S_1 and S_2 are containers of pure solvent (usually water). During the formation of the atomic film, an adsorbed monolayer of the primary ionic precursor is crucial in acquiring a homogenous and highly ordered film. Therefore, removal of the excess ions adsorbed on the substrate surface is critical, and this is achieved by immersion into the rinsing solution S_1. A similar action is performed by the rinsing solution S_2, after the desired product layer is formed in the solution B which include the secondary ionic precursor. Following the final rinse at S_2, the deposition cycle comes to a completion, after which the substrate is moved back to A for the initiation of a new deposition cycle. At the start of the process, the substrate needs to be cleaned of any possible contaminants such as organic impurities, adventitious carbons and dust particles. This ensures the optimal contact and interaction between the solution and the surface of the substrate. Furthermore, any surface contamination may lead to film delamination at a later stage. In some cases, cleaning of the surface could be insufficient to obtain good adhesion to the substrate due to weak interactions between film material and substrate surface.

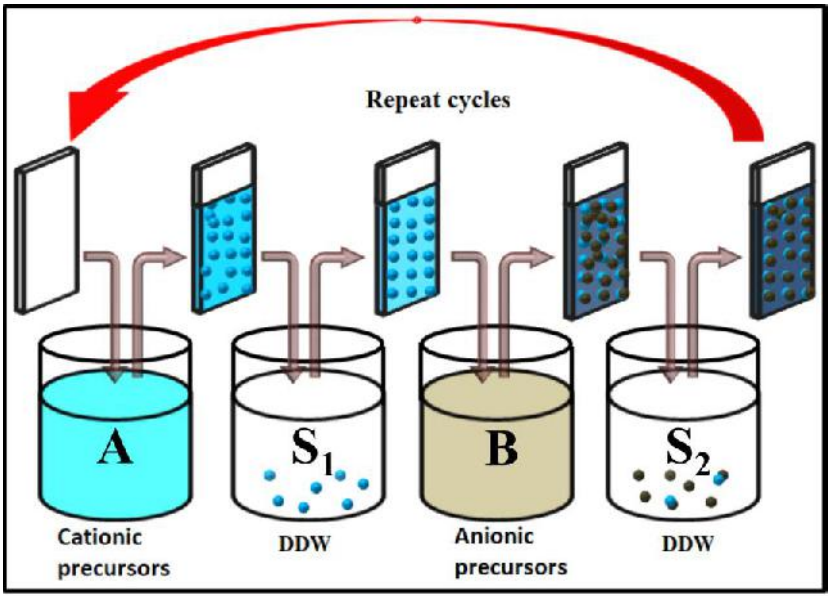

Figure 2.1: Schematic of four beaker SILAR method.

(b) Rinsing:

This is the second step where loosely bound ions are removed by rinsing the substrates into the rinsing solution. This step is crucial as the involvement of this step can significantly affect the morphology, particle size and their agglomeration. For rinsing purpose, generally double distilled water is used. One can avoid this step for their convenience.

(c) Reaction:

This is the third step where beaker containing anions is placed at the third place where anions from the anionic bath reacts with the pre-adsorbed cations due to their rapid reactivity. If the ionic product of cations and anions are well maintained with respect to solubility product, the reaction rate of the anionic bath can be controlled.

(d) Second rinsing:

This is the last step in the deposition process where unreacted species present on the surface of the substrate are removed by means of dipping substrate into the rinsing solution. It also helps to remove the excess species present on the substrate surface. In this step also, mostly DDW is used for rinsing purpose. Some mechanically operated SILAR systems have provision to rotate the substrate into the solution of interest.

(e) Deposition parameters:

The deposition of thin films by SILAR method depends on many experimental parameters that have crucial effect on the quality of the thin film. These parameters include pH of cationic and anionic bath, temperature of the baths, concentration of the cationic and anionic solutions, adsorption reaction and rinsing times, complexing agent and nature of the substrate etc. these parameters are also determines the growth kinetics on the substrate. These parameters are discussed in detail below

(i) Concentration of precursors:

The concentration of precursor plays a crucial role in determining the thickness of the film in all chemical reactions. It is well known that suitable concentration of the precursor results in optimized film thickness that ultimately affects the performance of the material. If the concentration of cationic precursor is higher, the rate of adsorption increases that unnecessarily increases the film thickness, and if the concentration of anionic precursor is higher than the rate of reaction increases that rapidly increases the particle size that again affect the performance of the material. If the application to be tested is thickness dependent, then, the concentration of the precursors can be employed to control the thickness of the film [12].

(ii) pH:

The pH of the solution is the rate determining factor in the chemical reaction. The main role of pH lies in the hydrolysis of cations in the cationic solution that ultimately determines the final phase formation of the material. Also pH of anionic solution is maintained to control the rate of reaction and to control the film formation. Another effect of pH is observed in tuning the microstructure or morphology of the material that can be altered by altering the pH of the cationic and anionic solutions. However, one should keep in mind that, highly acidic pH can result in the corrosion of metallic substrates.

(iii) Temperature:

The temperature given to the cationic and or anionic solution results in the crystallization of the material during its formation. It is well known that, crystallinity largely depends on thermodynamical energy received during the reaction. Most of the SILAR reactions do not employ heat treatment that results in the formation of amorphous phase. However, crystallinity can be retained by providing heat treatment to the required solutions. Most importantly, in case of using complexing agent, the breaking of complex is done by providing heat to the proper solution.

(iv) Complexing agent:

The concentration of metal ions in the solution and their release into the solution decides the kinetics and growth of the material. At many instances, one needs to control the rapid hydrolysis of the metal ions with their continuous release. To achieve this condition, complexing agents can be used that possess donor which form coordination bond with the cations thus restraining their rapid adsorption. Adding complexing agent provides an additional kinetics step in the reaction that provide surface relaxation time that facilitates regular growth. The complexing agents form the complex with the cations which can be further removed by heating the solution. This results in avoiding the rapid precipitation as well as larger thickness. Different chemicals can be used as a complexing agent including ethylenediamine tetraacetic acid (EDTA), ammonia, triethanolamine (TEA), ethylenediamine etc.

(v) Number of cycles:

It is well known that thickness of the film increases upon increasing the number of cycles during a SILAR reaction. Therefore, it is necessary to optimize the cycle number to achieve better performance. Less number of cycles results in irregular and non-uniform growth of the material and higher number of cycles can cause cluster formation as well as peeling off of the thin film.

(vi) Rinsing time:

Rinsing process can avoid the unnecessary formation of clusters as well as remove the loosely bounded counter ions in the material that can cause impurity.

Therefore, it is important to experimentally optimize the rinsing time of the reaction in order to obtain a uniform film thickness.

(f) Advantages of SILAR method:

The SILAR has proved to be much economical and feasible deposition method that one can use at any lab without any sophisticated instrumentation. Apart from these benefits, other advantages of SILAR as listed below-

- It is an inexpensive, and easy deposition method that allows deposition over large area.
- In this method wastage of material avoiding.
- Being a low temperature deposition process, variety of substrates can be used for the deposition which prevents corrosion of the metallic substrate.
- This method is very applicable for doping any foreign atom into the material with the required proportion.
- The preparative parameters can be controlled easily to achieve desired thickness that ultimately affects the physicochemical properties of the material.
- A comparatively uniform thin film can be deposited on any kind of substrate having a complex configuration.

2.3 Thin film characterization techniques:

2.3.1 Structural and elemental characterization techniques:

The physicochemical properties such as chemical composition, crystal structure, surface morphology, specific surface area, and conductivity are strongly correlated with their electrochemical characteristics. Therefore, the characterization and analysis of thin film material by various techniques results to explain the relationship between different properties. This helps to decide proper thin film material and its various application. These methods also make it easier to check modifications in thin film materials. Thus, the thin films in the present investigation were analysed via various characterization techniques. The comprehensive elaboration of the basic principle, instrumentation, and working of these techniques are described in this chapter.

2.3.1.1 X-ray diffraction (XRD):

In materials science field, XRD is a well significant, and mostly used characterization technique to obtain information on the atomic scale structure of different substances in a different of states [13]. This technique also provides information on unit cell dimensions. The XRD is an important and common technique used to the determine crystallite size (D) and to calculate lattice strain, and phase analysis as well.

Working principle:

The XRD analysis depends on constructive interference of monochromatic X-rays from sample. The interatomic distance (d) in materials is on the order of few Angstroms (Å) which corresponds to wavelength of X-rays (energy between 3-8 keV). Therefore, the crystalline materials are revealed to the X-rays, both constructive and destructive interference patterns are observed. When the intensity of diffracted X-rays measured as a function of scattering angle, a diffraction pattern is obtained. In Bragg's condition (Figure 2.2), the constructive interference of diffracted X-rays observed when path difference ((AC+CB)-AB) equals to the wavelength of X-rays (λ). The bragg condition can be written mathematically as [14],

$$d\sin\theta + d\sin\theta = n\lambda \text{ Or } 2d\sin\theta = n\lambda \qquad 2.1$$

where n, θ and d are the order of diffraction, glancing angle or Bragg's angle, and interplaner distance, respectively.

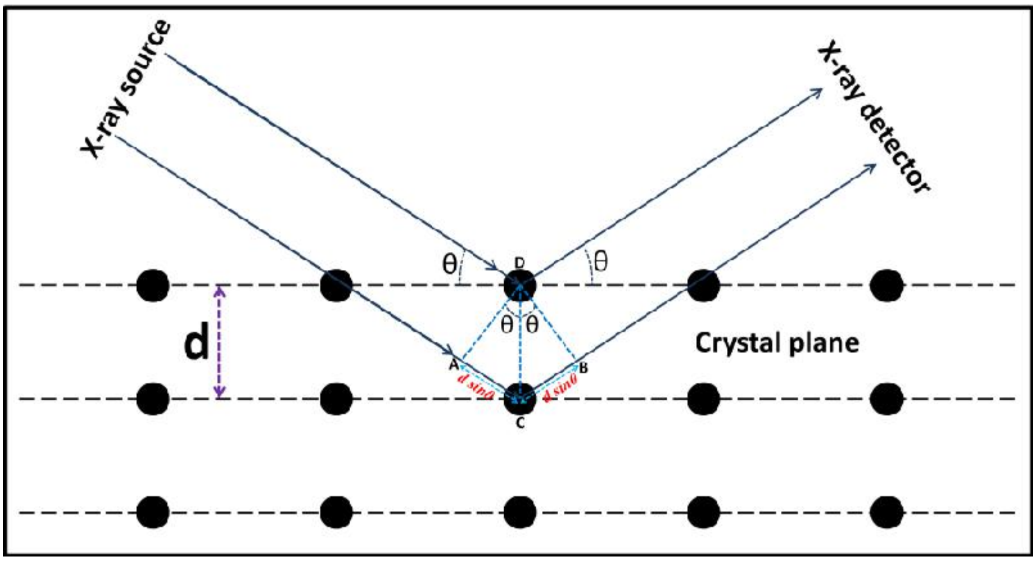

Figure 2.2: Bragg's diffraction.

Working of instrument:

The X-Ray diffractometer incorporate three major components; first is a monochromatic source of X-ray, second is specimen holder and third is X-ray detector. The X-ray generator is known as cathode ray tube, which is made of a cathode, monochromator and target material enclosed in glass or ceramic container at vacuum (Figure 2.3). The cathode is heated to generate electrons; generally it is of tungsten filament. These electrons are accelerated towards target material (Cu, Fe, Mo, Cr) by applying high voltage. If electrons have sufficient energy to emit inner shell electrons from the target element, the outer electrons jump into inner shells and to compensate energy difference the radiation is emitted, which is the characteristics of target material. For copper as a target material, radiation including K_α and K_β lines are emitted.

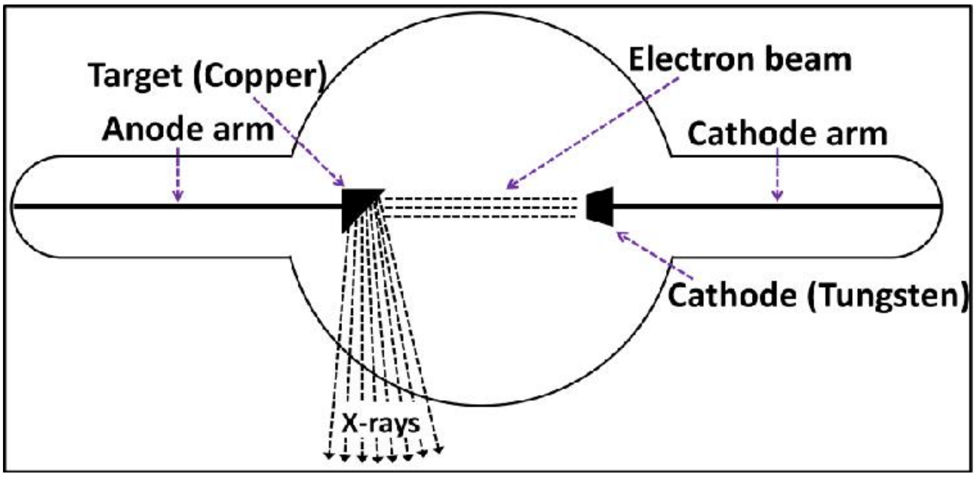

Figure 2.3: Schematic of X-ray tube.

These radiations undergo filtering process to generate monochromatic X-rays. The wavelength of copper radiation is CuK_α = 1.5406 Å. Now, monochromatic X-rays are collimated and directed towards preferred specimen to be characterised. As detector and specimen are rotating, when Bragg's condition satisfy, peaks in the X-ray intensity is recorded. The Figure 2.4a shows the schematic of X-ray instrument. The detector records the signals and converts it into count rate and a provide to output instrument (computer) for further process.

Three methods are available to determine the crystal structure of sample i) Laue method, ii) rotating crystal, and iii) powder method.

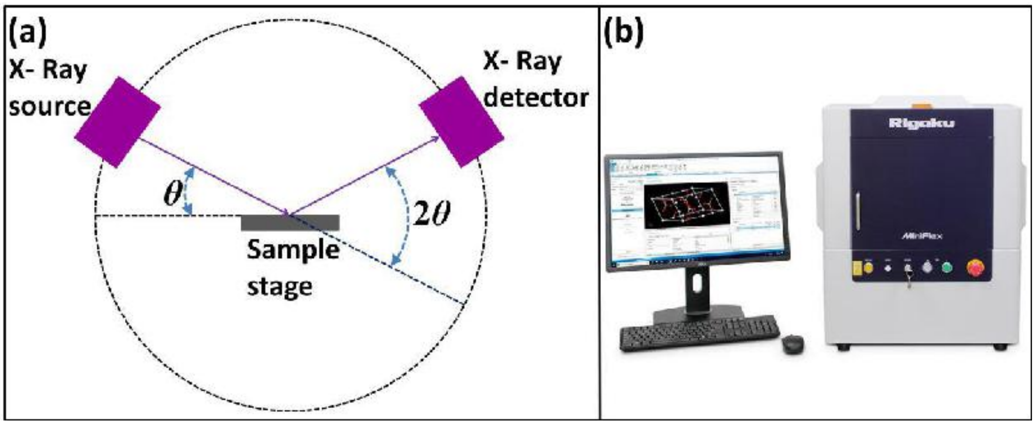

Figure 2.4: a) Schematic of X-ray instrument [15], and b) photograph of RIGAKU Mini Flex 600 diffractometer [16].

Laue is the oldest method for the determination of crystal structure, where continuous spectrum of X-ray is used and angle of incidence (θ) is fixed. This method gives faster diffraction than other methods in which monochromatic X-rays used. Therefore, it is used to observe dynamic process in crystal structure. If the angle of incidence (θ) is fixed and wavelength (d) is variable then that method is known as rotating crystal method. In rotating crystal method, a monochromatic beam of hard X-rays allowed to fall on sample which is rotated at a constant angular velocity. In order to easy analysis the crystal structure of sample, powder method is mostly used. In case of powder method, wavelength (λ) is taken as a fixed and angle of incidence (θ) is variable. Figure 2.4b shows the photograph of Bruker D_2 phaser X-ray diffractometer. One very crucial use of XRD when dealing with nanocrystals is to determine crystallite dimension using the Scherrer formula [17]:

$$D = \frac{0.9\lambda}{\beta\cos\theta} \qquad 2.2$$

where β *and* θ *are the* full width at half maximum (FWHM) of the diffraction peak, and peak position in radians, respectively.

2.3.1.2 Fourier transforms infra-red spectroscopy (FT-IR):

The FT-IR spectroscopy provides qualitative information about the chemical bonding in materials which is a non-destructive analysis. FT-IR technique can be used for analysis of solids, liquids and gases. FT-IR stands for Fourier transforms infra-red and the technique is highly sensitive photo spectroscopic method for the identification of chemical bonding between the species present in the material. It is also known as structural finger prints of the chemical nature of the material.

Working principle:

Molecular bonds vibrate at fixed frequencies which are depending on the texonomy of bond and elements included in bonding. According to quantum mechanics, these frequencies correspond to the several excited states and ground state. When these bonds absorb light energy of fixed frequency they can be exited to upper possible state of energy. For any given transition between two states the light energy should be equal or greater than the difference in the energy between first excited state and ground state. The wavelength absorbed via the bond is the properties of chemical bond which can be seen in spectrum. The range of mid-infrared part is

200 to 4000 cm^{-1}. Figure 2.5 illustrates the schematic of FT-IR instrument with Michelson interferometer [18].

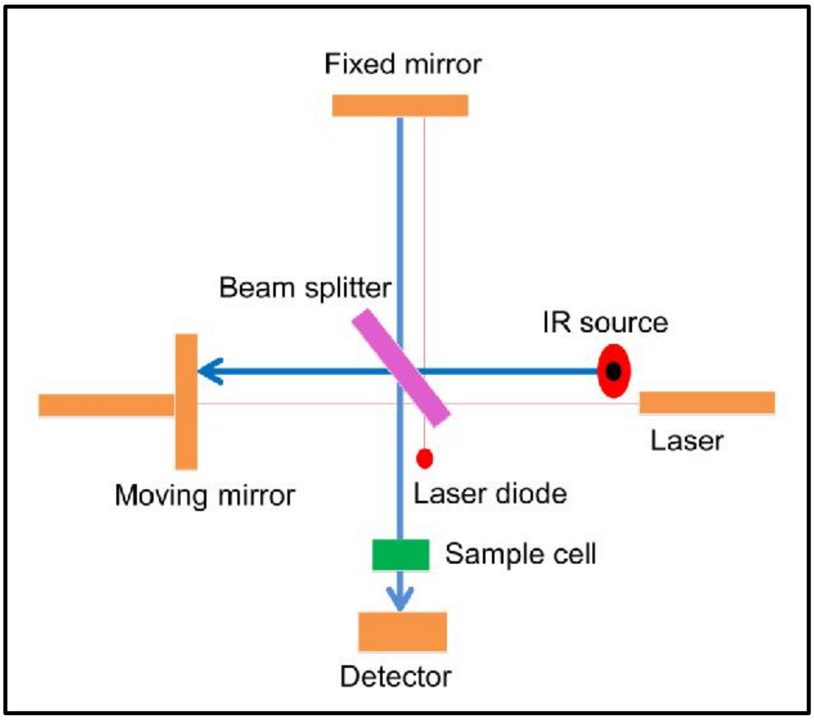

Figure 2.5: Basic schematic of FT-IR with Michelson interferometer.

Working of instrument:

A common FT-IR spectrometer consists of an IR source, sample compartment interferometer, detector, A/D convertor, amplifier, and a computer. The photograph of ALPHA II compact FT-IR spectrometer is depicted in Figure 2.6a. Figure 2.6b shows the schematic diagram of the basic FT-IR system coupled with amplifier and necessary electronics for conversion of acquired data. The IR spectrum is a graph of infrared light absorbance via the substance on the vertical axis and the frequency (wavenumber) on the horizontal axis. Silicon carbide rod, kanthanl and nichrome wire coils, carbon arcs and Nernst glowers are used as the source of IR radiation. The beam splitter is made of a material that reflects half of the radiation striking it while transmits the other half. Out of these two beams, one is transmitted to stationary and other to moving mirror. Again, these beams reflected back and undergo splitting and only one beam directed towards sample with other to source. The stationary mirror is made of highly reflecting material. The simplicity of FT-IR design lies in moving mirror which mirror creates path length difference between two beams from moving mirror and stationary mirror and forms interference pattern.

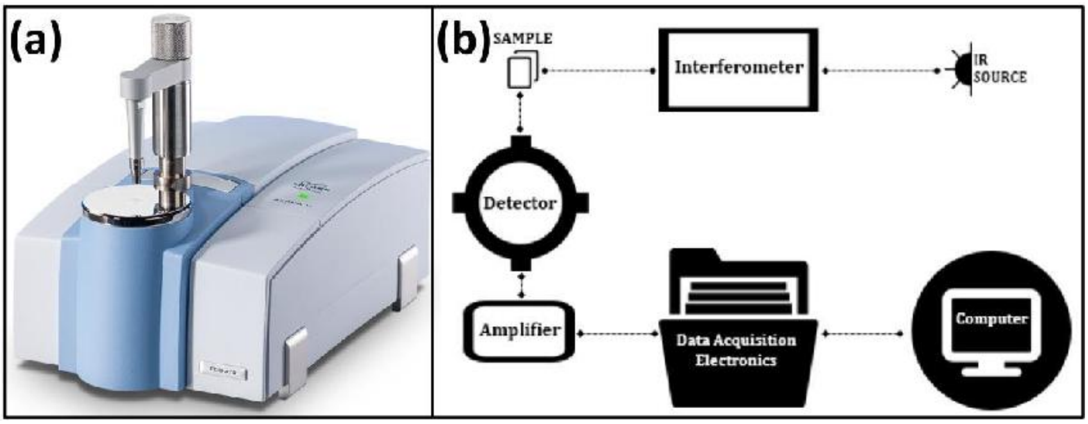

Figure 2.6: a) Photograph of ALPHA II compact FT-IR spectrometer [19], and b) the basic ray diagram of FT-IR system [20].

For FT-IR characterization the sample must be thin so the IR radiations must pass easily through it. This serves as one of the merit of FT-IR analysis as it needs very tiny sample. When IR radiation is passed through a sample, few of the radiation is absorbed by the sample and remaining is transmitted. There are two types of detector one is thermal and other is quantum detectors. Thermal detectors treat received light as heat, while quantum detector as light. Therefore, quantum detectors are highly sensitive. After that obtained data in terms of intensities are processes via Fourier transform and plotted against wavenumber. For an analysis purpose, observed data is compared with available reference spectrum. There are no two unique molecular structures, that can yield similar infrared spectrum. Therefore the infrared spectroscopy is helpful for several types of analysis. The following information is obtained using the FT-IR spectroscopy [21],

Identification of unknown materials.

(a) Determination of the quality or consistency of a thin film sample.
(b) Determination of nature of bond between the species.

2.3.1.3 Raman spectroscopy:

Raman spectroscopy technique is a highly versatile technique that offers a simple, fast and nondestructive analysis of inorganic and organic materials [22]. It uses the interaction of light with the material to gain insight into properties of material and its constituents. It measures different modes of molecules like vibrational, rotational and other low frequency modes [23].

Working principle:

Raman scattering is a two photon process. Electrons have different vibrational levels and they are defined via specific energy differences (Figure 2.7). When an incident monochromatic light interacts with an electron in the sample, after that electron absorbs energy from an incident photon and electron goes to a higher energy state. The electron falls back to an energy level via losing energy. When the energy lost equal to the energy of the incident photon, electron falls back to its initial level and loses one photon. Therefore the molecule doesn't have any Raman active modes. This secondary photon has the same frequency as the incident photon and Rayleigh scattering occurs.

However, sometimes electrons while losing energy from the virtual state can fall back to a different vibrational level. In this case, the energy lost by the electron is different than the energy absorbed from the incident photon. As a result, the emitted photon has energy different than the incident photon. In this case, the frequency of the emitted photon is not equal to the incident photon. This gives the Raman scattering. Depending on the final vibrational level of electron Raman scattering is separated into stokes line and antistokes lines. The radiation having lower energy as compared to the incident radiation is known as stokes lines, while the radiation having higher energy than incident radiations are known as antistokes line [24].

The Raman shift Δυ is negative for anti-stokes and positive for stokes and it is a characteristic feature of material undergoing Raman shift. It gives the molecular fingerprint and it is different for different molecules. By studying the Raman spectra one can identify the rotational levels and thus a particular molecule. This helps to analyse the sample qualitatively.

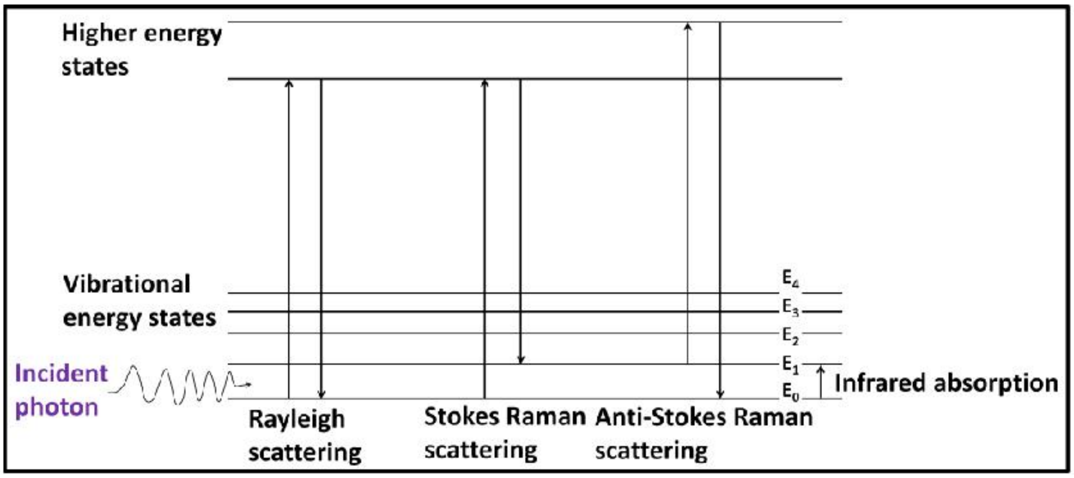

Figure 2.7: Energy level diagram showing the states involved in Raman spectrum.

Working of instrument:

Raman spectrometer consists of three primary components: An excitation source, a sampling apparatus, and a detector. Figure 2.8 demonstrates the basic block diagram of Raman spectrometer. In Raman spectroscopy a monochromatic excitation source is used. Generally, a laser with extremely narrow and stable bandwidth used as an excitation light source. The laser source must have particular properties like, small form factor, low power consumption, narrow line width, a stable power output and a stable wavelength output. For organic molecules it is important to shift the laser wavelength into the near infrared to minimize fluorescence while not exceeding CCD spectral detection limits. Owing to availability and the maximum fluorescence reduction without the sacrifice of spectral range or resolution 785 nm diode lasers have become more favourable, highly colored or strong fluorescence samples, suitable for 1064 nm laser is a good choice. For inorganic molecules, 532 nm laser is the most suitable choice as it provides increased sensitivity. Sample interface is the second component where fibre optic probe is used. It usually offers the flexible sampling interface. The flexibility afforded via fibre optics not only allows for the probe to be taken to a solid sample, but also allows it to be immersed in liquids slurries in environment as well as laboratory process.

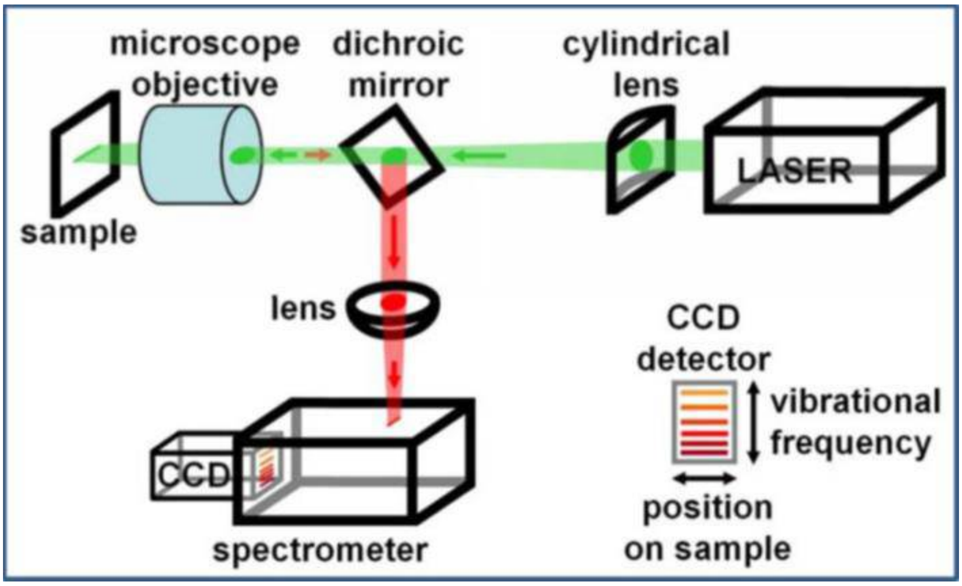

Figure 2.8: The basic block diagram of Raman spectrometer [28].

It can also be connected to microscopes and cuvette holders. Third component is spectrometer which has some property such as low noise, small form factor, low power consumption, and high resolution to detect very weak Raman scattering [25].

Further, the desired detector is needed and is based on the type of excitation laser being used. Mostly, charge coupled device (CCD) is used as the detector for Raman spectroscopy. For low concentrations weak Raman scatters, it may be required to use a back thinned CCD to further boost the spectrometer sensitivity [26, 27].

2.3.1.4 Field emission scanning electron microscopy (FE-SEM):

To find out surface morphology at high resolution FE-SEM microscope is a dominant instrument. It employs electrons instead of photons for imaging process. These electrons are liberated through a field emission source. The FE-SEM provides topographical and elemental information at magnifications of 10 X to 300,000 X, with virtually unlimited depth of field.

Working principle:

The FE-SEM images a sample surface via raster scanning over it with a high energy beam of electrons. The primary electrons liberated from a field emission source are accelerated in the electric field. Using electromagnetic lenses, a narrow beam is created via focusing these primary electrons. The beam is allowed to strike the sample. After interaction, primary electrons lose their energy inside the sample, due to which; various type of electrons are ejected from the sample as illustrated in Figure 2.9. This is because of an emission of secondary electrons from the sample. The electrons interact with the atoms comprising the sample to produce secondary electrons that contain information about surface topography, and composition. By processing these electrons, detector generates an electric signal which is further amplified and transformed into an image.

Working of instrument:

The schematic diagram of the FE-SEM instrument is illustrated in Figure 2.10a. An electron gun, magnetic lenses, an anode (accelerator), sample holder and detector are the main parts of a FE-SEM instrument. Overall assembly is mounted on a desk. For operation, the gun head, specimen and column chamber have to be evacuated. Column chamber valve remains closed until the detected pressure is not ready for operation. After vent command, column chamber valve closes and N_2 gas flows into the specimen chamber through vent valve. Sample preparation is also one of the parts of FE-SEM characterization technique. The sample should be conductive. Before mounting on a special holder, the samples are first made conductive by coating them with ultrathin layer electrically conducting metal such as gold (Au), platinum (Pt), gold/palladium (Au/Pd), silver (Ag), chromium (Cr), or iridium (Ir) [29]. The conductive layer of metal on the sample prevents charging of the specimen, decreases thermal damage and rises the amount of secondary electrons hence increases the signal to noise ratio.

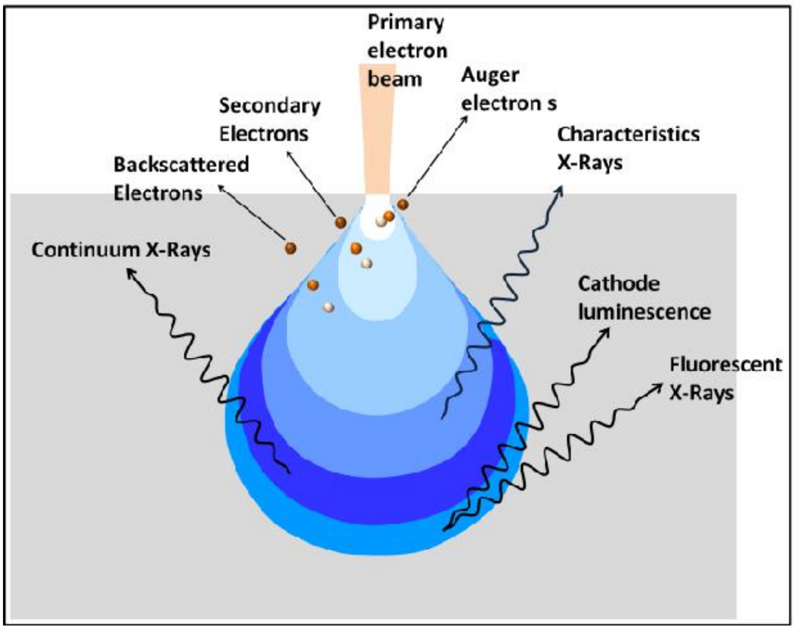

Figure 2.9: Ray diagram for the emission of different types of electrons after the interaction of primary electrons from source with sample.

In FE-SEM, high-energy electrons (termed as primary electrons) are generated via placing a filament of tungsten fashioned into a sharp point; in a high electrical potential gradient (cathode). The voltage difference between anode and cathode allows generated electrons to accelerate towards the sample. The voltage is in the order of magnitude of 0.5 to 30 kV, and the high vacuum ($\sim 10^6$ Pa) in the column of the microscope is maintained. The electron beam is focused by the electromagnetic lenses to a small sharp spot. The condenser lens controls the amount of magnification. Objective lens focuses the electron beam onto the specimen. Objective lens includes of electrostatic and electromagnetic lens. Deflection system consists of a set of scan coils to move the electron beam in a point-to-point scan process. Once the focused electron beam bombards on the sample surface, it penetrates the sample up to a few microns and interacts in different ways [30]. The scattering of electrons and volume of interaction based on the atomic number, the energy of primary electrons, and the concentration of atoms of sample. The high energy of primary electrons rises scattering process and interaction volume. While the high concentration of atoms and the atomic number will decrease the interaction volume and scattering.

All these signals are gathered via a detector and separated based on their energy values. The secondary and backscattered electrons are used to produce a sample image via transforming and amplifying the signals. When primary electrons interact with electrons at the inner shell and knock it out, the electron from a higher energy level jumps to lower energy via losing some energy. This extra energy is lost in the form of X-rays. Hence, every element in the sample creates a characteristic X-ray. All these characteristic X-rays from all elements are used to identify the elemental composition of the sample by energy-dispersive X-ray spectroscopy (EDAX) coupled to the FE-SEM instrument [31]. Figure 2.10b demonstrates photograph of FE-SEM instrument.

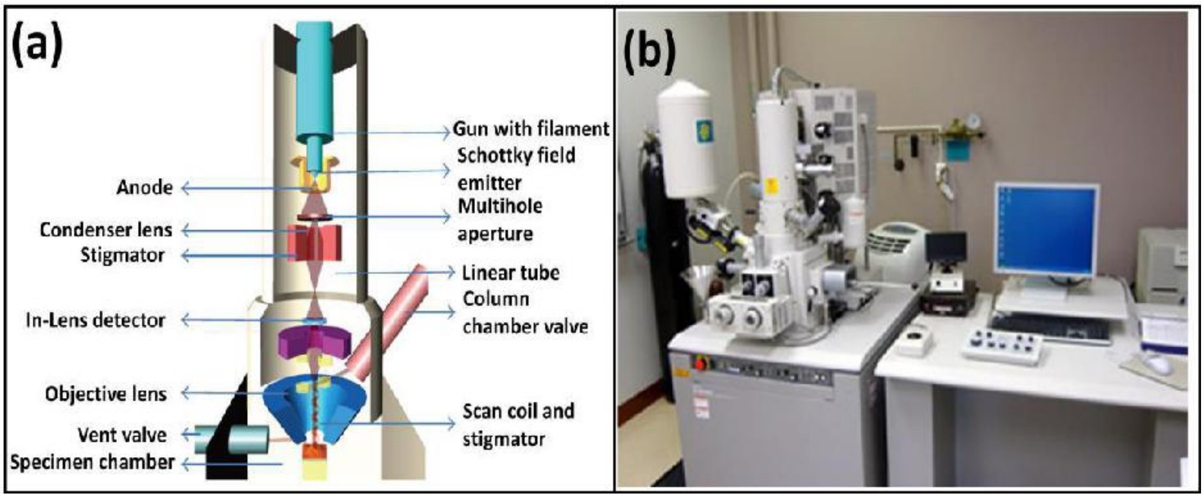

Figure 2.10: a) Schematic of FE-SEM [32], and b) photograph of FE-SEM instrument [33].

2.3.1.5 X-ray photoelectron spectroscopy (XPS):

XPS in an effective analytical technique for the determination of chemical composition as well as oxidation states present in a compound. The XPS can study only surface of the specimen as it can go upto the depth of only 10 nm. This technique is primarily based on the photoelectric effect which states that when a metal is bombarded by highly energetic electrons, photoelectrons are ejected from the inner shell of the metal atoms.

Working principle:

When an X-ray having sufficient energy is made to fall on the specimen, the X-rays ejects the inner shell electrons from the specimen (Figure. 2.11) atoms and the kinetic energy of the ejected electrons are recorded. If the energy of the incident X-ray is known, one can calculate the binding energy of the ejected electrons using following relation

$$E_{binding} = E_{photon} - (E_{kinetic} + \varphi) \qquad 2.3$$

Where φ is the work function of the element.

Photoelectrons coming out of the specimen are counted and depending their kinetic energy, the composition and chemical states of the elements are determined.

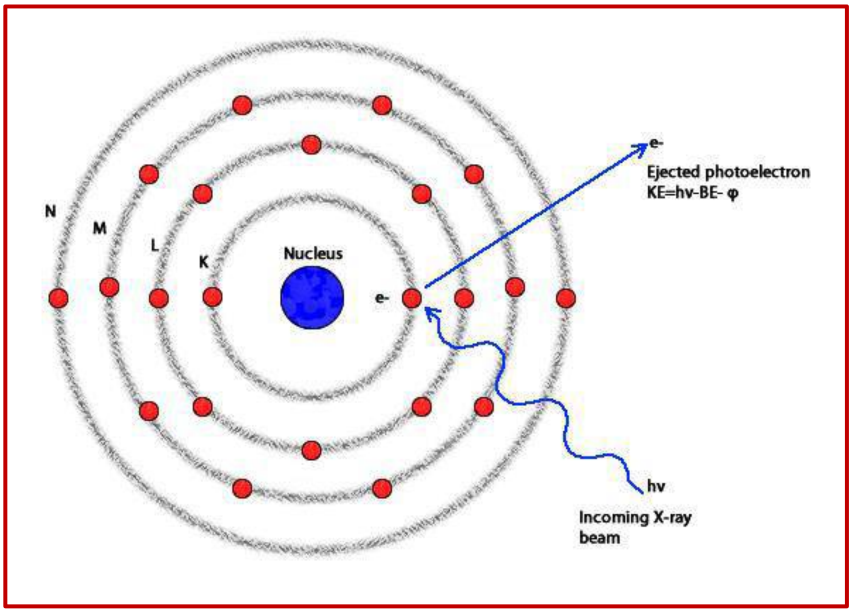

Figure 2.11: Ejection of photoelectron after bombardment of Mg Kα (hν = 1253.6 eV) or Al Kα (hν = 1486.6 eV) radiations in the XPS measurements.

Working of instrument:

In XPS, X-rays of typically MgKα or AlKα are emitted that are monochromatized using a monochromator. These monochromatized X-rays ejects the photoelectrons from the specimen upon their interaction and the electron detectors detects the number of photoelectrons as well as their kinetic energy. The software connected to the XPS instrument converts the kinetic energy of the electron into its binding energy. This data is then represented as a spectrum that shows the electron counts with respect to their binding energy. As every element possess specific binding energy, one can differentiate the element present in the compound upon the binding energy showed by the results. The X-ray photoelectron spectroscope, K-alpha XPS system of Thermo Fisher Scientific, U. K. is used in the present study.

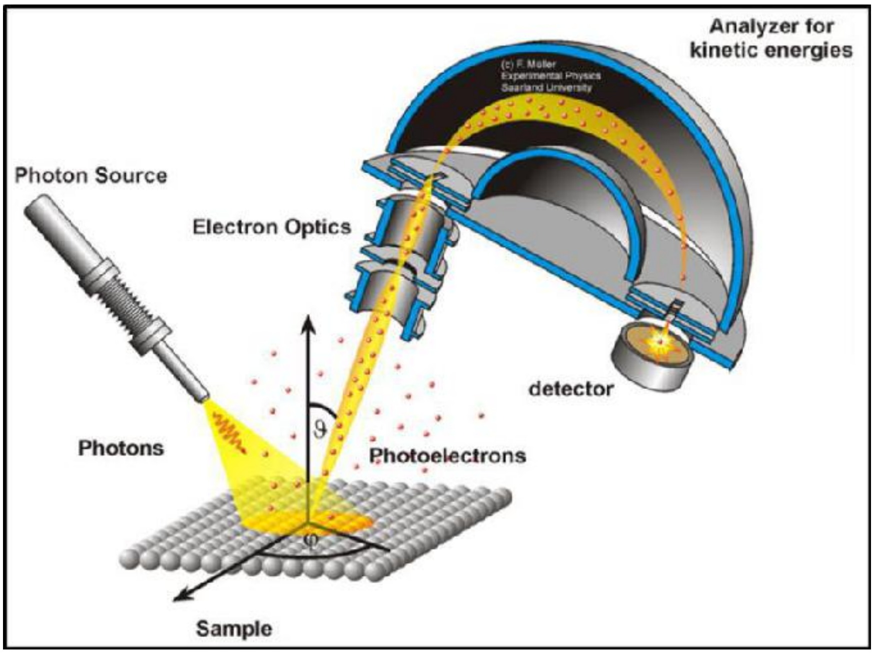

Figure 2.12: Schematic diagram of an XPS instrument [34].

2.3.1.6 Contact angle measurement:

Contact angle measurement enables one to study the contact angle between the solid surface and the liquid present over the surface of the solid. It is also useful to study surface wettability. Surface wettability helps to understand the nature of solid sample for the interaction with liquid, in addition, it is used to calculate the surface free energy. Figure. 2.13a displays the Rame-Hart contact angle measurement instrument and Figure. 2.13b shows the contact angle measurement of an unknown sample.

Contact angle is the angle between the liquid placed on a solid surface when tangent is drawn to the liquid and angle is measured from inside the liquid. The hydrophobicity and hydrophilicity study of the material can be confirmed using this instrument. For many applications, hydrophobicity or hydrophilicity and surface wettability study is important. If the angle between liquid and solid surface is greater than 90° it confirms the hydrophobic nature that means its surface is less wettable. If the angle exceeds 170° that means the surface is superhydrophobic [36]. These kinds of surfaces are very applicable in manufacturing self-cleaning materials. On the contrary, if the contact angle between liquid and solid surface is less than 90° that means the surface is hydrophilic. That means the surface can interact well with the liquid. Likewise, if the material shows contact angle less than 5° that means the surface is superhydrophilic and highly wettable. These kinds of surfaces are required for applications like supercapacitor or OER where ions from liquid electrolyte needs to intercalate in the material. The contact angle (θ) is calculated by the Young's relation [37].

$$\gamma_{s,\upsilon} = \gamma_{s,l} + \gamma_{l,\upsilon} \cos\theta \qquad 2.4$$

Where $\gamma_{s,\upsilon}$ is the solid-vapour, $\gamma_{s,l}$ is the solid-liquid and $\gamma_{l,\upsilon}$ is the liquid-vapour interfacial energies.

In the present study, contact angle images of deposited thin film electrodes are recorded using Rame-Hart goniometer (modal 260).

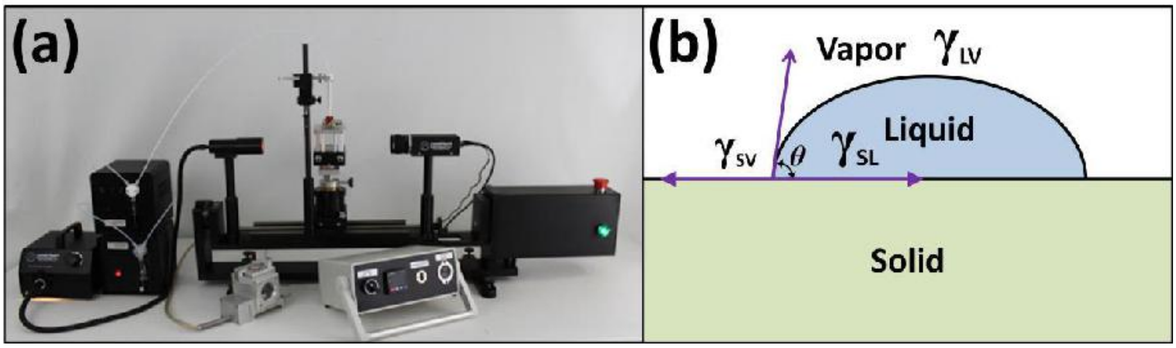

Figure 2.13: a) Photograph of Rame-Hart NRL contact angle meter [35], and b) contact angle of a liquid drop in contact with solid sample.

2.3.1.7 Brunauer-Emmett-Teller (BET) analysis:

This technique is basically used to measure the surface area and pore volume available for a particular material. This is done by pouring N_2 gas on the surface of the material at different relative pressures. After sometime the gas is taken out and the difference in the amount of gas sent inside and retrieved is measured. The result in m^2 g^{-1} provides the surface area of the sample of interest.

Working principle:

There are two different working principles for the surface area measurements viz. volumetric and gravimetric. In both the methods, first sample is put inside the chamber, heated upto required temperature and N_2 gas is poured in it at various relative pressures. In case of volumetric method, the change in the relative pressure is measured with respect to the reading taken without putting material into the chamber. In gravimetric method, the amount of N_2 adsorbed onto the surface and the difference between amount of N_2 sent inside and retrieved is measured and based on the calculation, surface area and pore volume are determined [38]. The isotherm is a plot of the amount adsorbed versus the adsorptive pressure. The pressure is expressed as a ratio of the adsorptive pressure (P) to the saturated vapour pressure (P_0). Volumetric measurement is generally employed due to its less cost and simple mechanism. However, uncertain results of the volumetric analysis limit their wide use. In that context, gravimetric analysis is much precise and accurate. Depending on the interaction of adsorbent with adsorbate, there are 5 different isotherms. The different isotherms and their significance are given below. Five types of adsorption isotherms in BET analysis is shown in Figure 2.14.

1. Type I isotherm- chemisorption or physisorption on a material with very fine pores.
2. Type II isotherm- if energy of adsorption is high in non-porous or microporous materials.
3. Type III isotherm- if energy of adsorption is low in non-porous or microporous materials.
4. Type IV isotherm- if energy of adsorption is high in mesoporous materials.
5. Type V isotherm- if energy of adsorption is low in mesoporous materials.

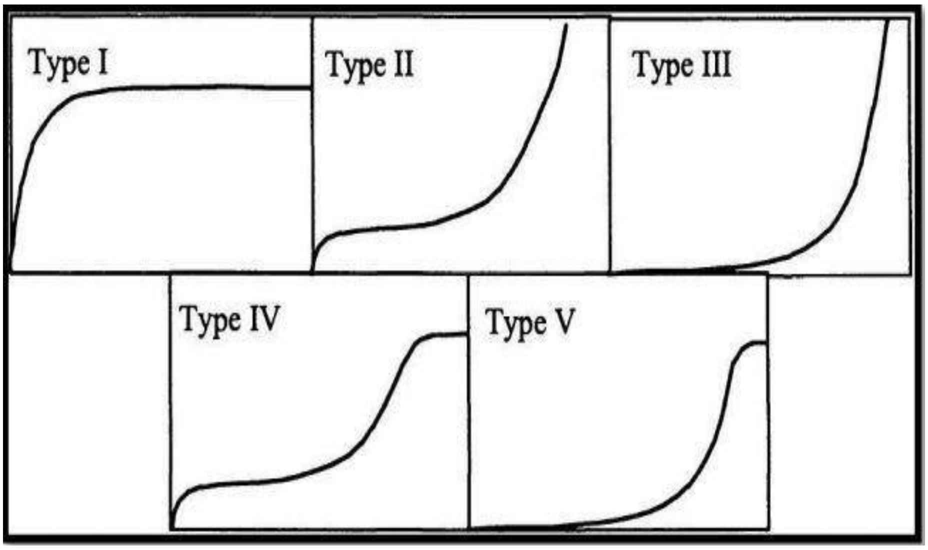

Figure. 2.14. Five types of adsorption isotherms in BET analysis.

The concept of desorption is bit different from adsorption and is called as hysteresis. As per IUPAC system, 4 distinct hysteresis curve are present. The 4 hysteresis loops are termed as H_1, H_2, H_3 and H_4. The hysteresis does not take place below relative pressure of 0.42 in case of N_2 adsorption. To evaluate specific surface area (As) from cross sectional area of adsorbate molecule (a) and number of mole of adsorbate in a monolayer (nm),

$$A_s = n_m N_A a \qquad 2.5$$

where $a = \left(\frac{M}{P}\right)^{\frac{2}{3}} N_A^{1/3}$, M is the molar mass (g mol^{-1}), ρ is the liquid density (gm^{-3}), and NA is Avogadro's number (6.022×10^{-23} mol^{-1}).

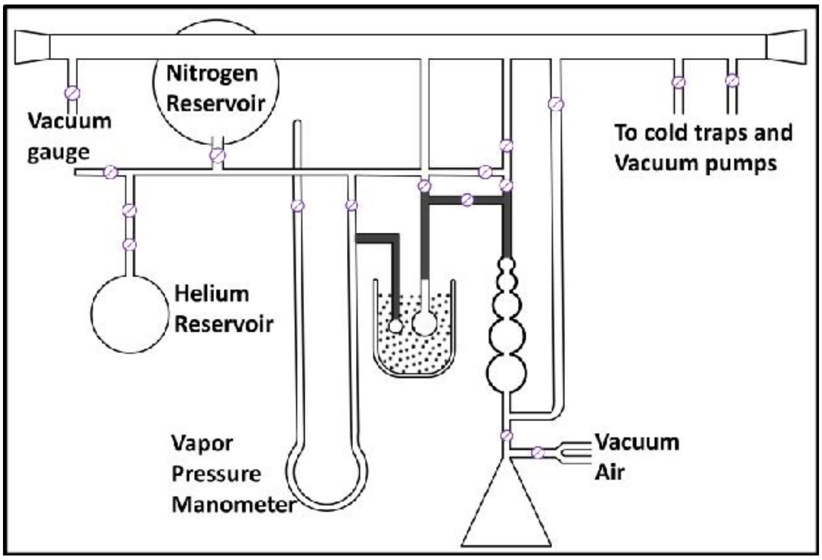

Figure 2.15: Schematic diagram of the dynamic flow method apparatus [39].

Working of instrument:

As discussed above, the surface area of a material can be determined either by volumetric method or gravimetric method. The typical working of the instrument rely on the assumption that the N_2 adsorbs on the surface of the material. The adsorbed gas is measured as a function of temperature and pressure which is then converted to give specific surface area and pore size distribution of the material. The schematic of volumetric method is shown in Figure 2.15. System parts are not to scale. Sample chambers are usually constructed from Pyrex [40].

2.3.2 Electrochemical characterization techniques:

Need of development of diverse electrical energy storage devices specifically designed for certain purposes such as wearable and portable electronics, health care systems, etc., have increased interest of scientific community in electrochemical energy storage. Ragone plot (Figure 1.1) showing performance of electrochemical energy storage devices suggests S_E of fuel cells are very high and S_P of capacitors are higher compared to batteries and SCs. Along with batteries, SCs bridge the gap between fuel cell and capacitors [41]. Taking in to account that diversity of electrode materials, electrolytes, and ability to support various designs according to requirement in many fields (aerospace, medical, military, transportation etc.) SCs, often called supercapacitors have attracted research interest globally. The SCs are classified according to mechanism of charge storage or configuration or physical state of electrolyte into various classes. Based on charge storage mechanism, SC electrodes are classified as EDLCs (non-Faradic mechanism), pseudocapacitors (Faradic mechanism), and battery type. The SCs are classified as symmetric and asymmetric in which configuration is considered and second one is liquid-state and solid-state, based on physical state of electrolytes [42]. Generally, SC consists of two conducting electrodes separated by porous membrane immersed in relevant electrolytes. The specific capacitance (C_s) of such device are determined by the following relations;

$$\text{Specific capacitance} = \frac{1}{m\upsilon\Delta V}\int_{v_1}^{v_2} I(V)dV \qquad \text{(CV study)} \qquad 2.6$$

$$\text{Specific capacitance} = \frac{I \times t}{m \times \Delta V} \qquad \text{(GCD study)} \qquad 2.7$$

where $\int_{V_1}^{V_2} I(V)dV$ is the area enclosed in a CV curve, m (g) is deposited mass of material on both electrodes, v (V s^{-1}) is the potential scan rate, Δ (V) is an operational potential window, and I (A) is the current response. To better understand the electrochemical properties of the electrode material, the measurements such as CV, ECSA, GCD, Tafel slope and EIS are necessary. Consequently, for application of thin films as an active electrode for SC devices, the electrochemical features are significant.

The energy density (ED) and power density (PD) of $CoWO_4$ electrodes are calculated using following equations,

$$\text{ED} = \frac{0.5 \times C_s \times \Delta V}{3.6} \qquad 2.8$$

$$\text{PD} = \frac{E \times 3600}{T_d} \qquad 2.9$$

where, ΔV is the potential window in (Volt).

To achieve higher values of *ED* and *PD*, the working voltage and C_s of SC must be large with lower interfacial resistance [43]. However, C_s and working voltage depend on the combination of electrode and electrolyte used in SC fabrication.

Generally, EDLC type materials can operate up to 1 V in water based electrolytes, while in organic electrolytes potential window can be extended to 2.5 V (sometimes up to 3.0 V). In EDLCs, the electrically conducting electrode and ionically conducting electrolyte, in which electric double layer is formed at the interface. The electric charge storage in EDLCs type SC shown in Figure 2.16a can be written as,

$$E_{s1} + E_{s2} + K^{+} + A^{-} \leftrightarrow E_{s1}^{-}//K^{+} + E_{s2}^{+}//A^{-} \qquad 2.10$$

where E_{s1} and E_{s2} are corresponding to the specific surface area of negative and positive electrodes. The symbol // indicates the electric double layer, where charges are stored on either side and $K^{+}$and A^{-} are cations and anions present in the electrolyte, respectively. The process of adsorption and desorption is accountable for charging and discharging of EDLCs, consequently no charge transfer occurs around the interface. Hereafter, the active electrodes are chemically inert; so this process is called as non- Faradaic [44]. The fast and reversible redox reactions with double layer capacitance give pseudocapacitance. The charge stored in pseudocapacitor is due to the Faradaic reaction at an interface of electrode and electrolyte. The schematic of different charge storage mechanisms observed in the pseudocapacitive materials is shown in Figure 2.16b-d. In Faradaic process, during charging discharging, the charges are transmitted on the electrode material as well as in the bulk of electrode material [45]. The charge storage in pseudocapacitor is done by two way process. In the first step accumulation of charges on the electrode material surface takes place. In second process, the redox reaction takes place in electrode surface as well as in the bulk of electrode material. Above two processes are mainly dependent on the applied potential, so the pseudocapacitance is also dependent on potential. To better understand the electrochemical properties of the electrode material, the measurements such as CV, GCD and EIS are necessary. Consequently, for application of thin films as an active electrode for SC devices, the electrochemical features are significant.

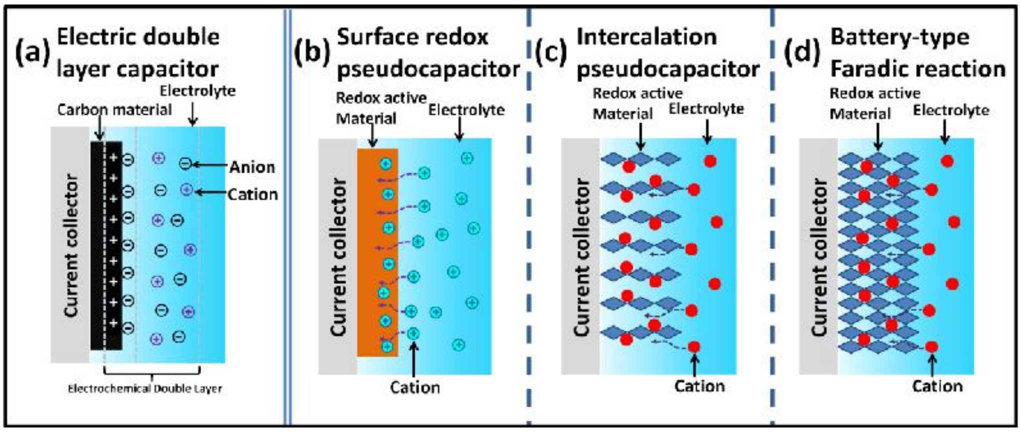

Figure 2.16: Schematics of charge-storage mechanisms for a) an EDLC [46] and (b−d) different types of pseudocapacitive electrodes: b) surface redox pseudocapacitor, c) intercalation pseudocapacitor, and d) battery-type Faradaic reaction [47].

2.3.2.1 Cyclic voltammetry (CV):

The CV offers a plentiful experimental information and insights into both thermodynamic and the kinetic details of many chemical systems. This is a fundamental characterization technique which provides information about electroactivity of electrode in various electrolytes. The reversal linear scan voltammetry carried out by switching direction of the scan at certain potentials is called CV. In CV measurement, the stationary electrode with 1 cm^2 area is used, which immersed in an electrolyte solution. The three electrode system is beneficial for minimization of ohmic resistance of electrode. The potential is applied between the working electrode and reference electrode, simultaneously the current measured between the working electrode and counter electrode.

In CV measurement, the potential is swept between given potential range, nevertheless, when the voltage reaches maximum potential limit then scan is reversed and the voltage is swept back to the minimum voltage range. Figure 2.17 illustrates CV curve for a reversible single electrode transfer reaction in the potential limit of V_2 to V_1. The I_{pc} and I_{pa} are cathodic and anodic peak currents, while E_{pc} and E_{pa} are cathodic and anodic peak voltages of the electrode material. In CV measurement, the selection of potential limit is important due to the oxidation and reduction positions of CV curve. One state of electrode material change to another during charging, while at reverse direction the electrode material achieves an initial state with reduction process.

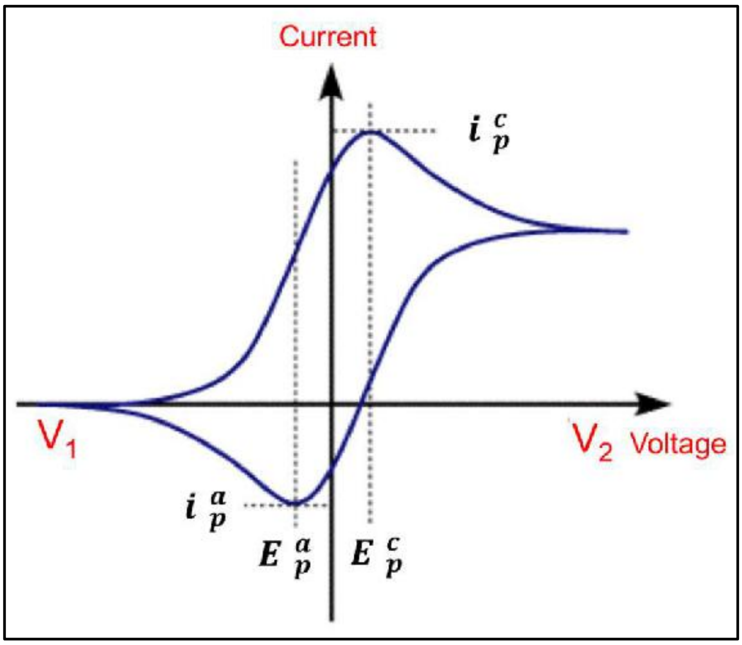

Figure 2.17: The typical cyclic voltammogram for a reversible single electron transfer reaction [44].

There are many fields in which CV technique is used extensively. These include metal-ligand interaction, in which electron pair transfer to form complex compound. Other applications include analysis of solids [45], solutions, polymers media with and without added supporting electrolyte, membrane [46], frozen solutions [47], emulsions and suspensions [48], and liquid-liquid systems [49], and biological systems such as enzymes [50]. Cyclic voltammetry (CV) is a potentiodynamic electrochemical measurement technique. In CV, the potential of the working electrode is ramped forward and backward through a predefined range with a constant sweep rate and the corresponding current is measured. Figure 2.17 shows a typical CV curve when the potential of the working electrode is ramped between V_1 and V_2. As the potential increases, the current increases and the anodic peak is obtained. This anodic peak is called an oxidation peak. As the potential comes back the current decreases at a certain potential cathodic peak is obtained which is called a reduction peak.

As the CV begins from V_1 the negative ions from the electrolyte get adsorbed on the surface of working electrode. As the potential of the working electrode increases slowly the concentration of positive charge also increases and resultantly more and more negative ions get adsorbed. Hence, a double layer of charge is formed on the surface of the electrode. This is called charge storage by double layer or non-faradic mechanism. But when the potential of the working electrode further increases, at a potential value the current suddenly starts to increase and an anodic peak is obtained. This positive current is due to the oxidation of the electrode material. After reaching V_2, the direction of ramping reversed from V_2 to V_1. In this reverse scan, the oxidized material gets reduced and the cathodic peak is obtained. This oxidation and reduction of material in a higher potential region are combined called a redox reaction of a material and the charge storage through this process is called a redox or faradic mechanism [51]. The capacitance of material due to the non-faradic mechanism is called a double layer capacitance (C_{dl}) and the potential range in which it is measured is called a non-faradic potential region.

To better understand the origin of electrocatalytic performance, the electrochemically active surface area (ECSA) of thin film electrocatalysts prepared in the present study is estimated from the C_{dl} values. The CVs are recorded at different scanning rates in the non-faradic region of potential. The difference between anodic and cathodic current density at a fixed potential is plotted as a function of scan rate. The slope of linear fitting to the measured values represents the double-layer capacitance (C_{dl}). ECSA is directly related to the C_{dl} of the material. For that purpose, one should record CV curves in the region of potential, where the faradaic process cannot be happening. Generally, that region is around the open circuit potential (OCP), hence the CV can be measured in the potential range with the OCP is at the middle of that window, where Faradic reactions not occurred. C_{dl} is calculated by plotting the anodic charging currents (i_{c}) at OCP of each CV curve against the scan rate by the equation:

$$\mathrm{i_c} = \mathrm{V}\, c_{\mathrm{dl}} \qquad 2.11$$

where, V is the scan rate. It yields a straight line with a slope equals to C_{dl}.

The 'C_{dl}' can be further converted into ECSA using the specific capacitance value of a standard 1 cm^2 flat surface, which is normally between 0.02-0.06 mF cm^{-2} for an alkaline medium [52]. Therefore, an average value of 0.04 mF cm^{-2} is used for the estimation [53]. Therefore, the ECSA for an electrode is estimated through C_{dl} value using the relation,

$$ECSA = \frac{c_{dl}}{0.04(mFcm^{-2})} \qquad 2.12$$

2.3.2.2 Galvanostatic charge-discharge (GCD):

In GCD technique, constant current is applied to the working electrode. The corresponding potential is measured against the reference electrode as a function of time. At initial the potential is suddenly changed because of the potential drop afterwards slowly changes in potential. Figure 2.18 shows charge discharge curve of SC. This is due to the concentration of the reactant exhausted at the electrode surface [54, 55].

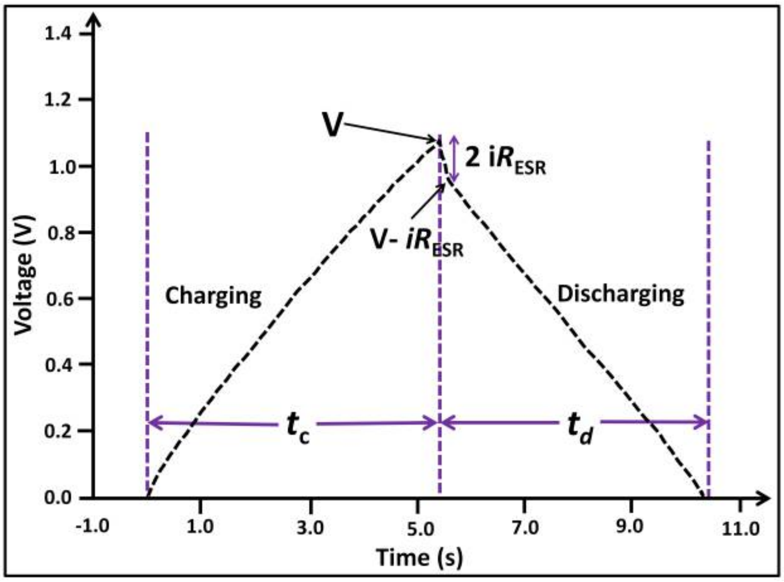

Figure 2.18: Charge discharge curve of a SC [56].

During discharging potential drop due to the solution and interfacial resistance, which can be corrected through the constant potential offset. From the nature of the charge discharge curve, the type of charge storage mechanism for sample electrode is confirmed. The symmetric shape of the charge discharge curve indicates the charge storage mainly due to the double layer mechanism if not then charge storage due to the pseudocapacitive mechanism [57, 58]. Additionally, GCD analysis is important to determine the S_E and S_P of the SC.

2.3.2.3 Linear sweep voltammetry (LSV):

Linear sweep voltammetry is a voltammetry method where current at the working electrode is measured while the potential between the working electrode and a reference electrode is swept linearly in time. The only difference between CV and LSV is that, in CV the potential is ramped between V_1 and V_2 in a cyclic manner ($V_1 \rightarrow V_2 \rightarrow V_1$) while in LSV potential is ramped from V_1 to V_2 in a linear way ($V_1 \rightarrow V_2$) as shown in Figure 2.19 (a). Hence LSV is nothing but the forward scan of CV (Figure 2.19 (b)).

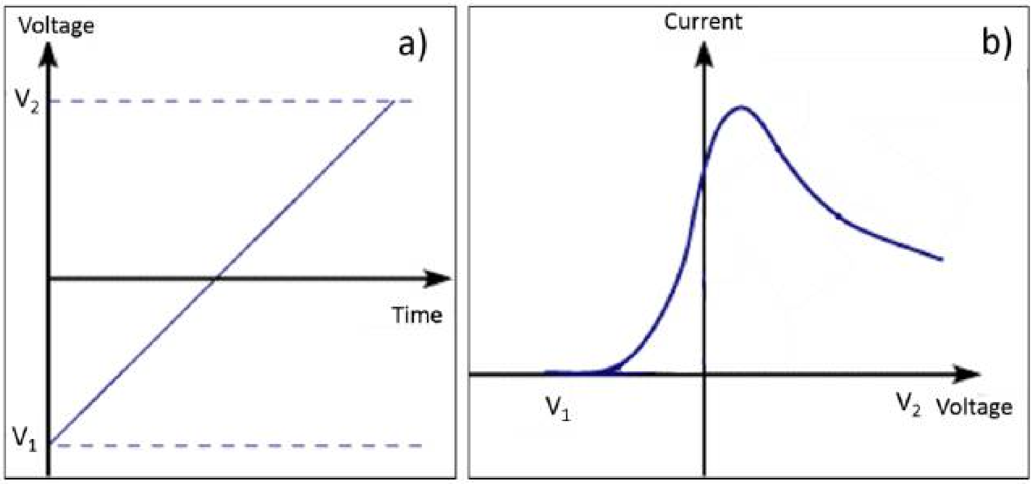

Figure 2.19: a) Potential sweep between V_1 and V_2 with time in LSV and b) corresponding current response as a function of voltage.

As discussed in CV, the peak occurs due to the oxidation of the material. After the peak potential, the oxidized species get saturated hence no material can oxidize on further increasing potential. Now if we further increased the potential of the working electrode the water oxidation reaction starts to occur at active sites. As we discussed in chapter 1, four electrons are removed in the evolution of one oxygen molecule (O_2). Hence current starts to increase. The scan rate during LSV measurement makes a great impact on the current response. The current increases with increasing scan rate. Hence while examining and comparing the LSV of more than two electrodes the scan rate must be similar. In the present study, all LSVs are measured with a scan rate of 2 mV s^{-1}. All the potentials measured (in SCE scale) in the present study converted to a reversible hydrogen electrode (RHE) scale by the Nernst equation:

$$E_{RHE} = E_{SCE} + 0.059 \times \text{pH} + E^0_{SCE} \qquad 2.13$$

where 'E_{RHE}' is the converted potential vs. RHE, 'E_{SCE}' is experimentally measured potential versus reference electrode (SCE), and 'E^0_{SCE}' is the standard redox potential of SCE at 298 K (0.244 V ± 0.002 V). From the polarization curve, overpotential, η at current density, j (mA cm^{-2}) is estimated through the relation,

$$\eta_{@j} = E_{RHE} - 1.23\ V$$

2.14 2.3.2.4 Tafel slope:

The current in electrochemistry is related exponentially to the overpotential as shown in equation 2.12.

$$I = a'\ e\eta/b' \qquad 2.15$$

where I is current, η is overpotential and a' and b' are constants. By taking logarithmic scale, the above equation can be written as,

$$\eta = a + b \log (I) \tag{2.16}$$

where a and b are constants. The above equation (2.16) is nothing but the Tafel equation. Tafel equation relates the rate of an electrochemical reaction to the overpotential. The low value of Tafel slope suggests the high rate of reaction or fast reaction kinetics while a high value of Tafel slope suggests the low rate of reaction or slow reaction kinetics [60]. To determine the Tafel slope first the Tafel plots are plotted from LSV curves for each electrode and then the linear component of the Tafel plot is fitted with the above Tafel equation.

2.3.2.5 Electrochemical impedance spectroscopy (EIS):

The charge storage mechanism at an electrode electrolyte interface is studied using EIS technique which is also called as an AC impedance spectroscopy. EIS works on a wide range of frequencies beneficial for accurate determination of resistances at an electrode electrolyte interface. The small AC signal (5 to 10 mV) is applied to the SC cell over a wide range of frequency from 1 mHz to 1 MHz. The output signals are the current response to the applied AC signals. The plot of imaginary impedance against real impedance is called as the Nyquist plot [61, 62]. A SC behaves as a pure resistor and capacitor at low and high frequencies, respectively. Moreover, in the medium frequency range, the physical and morphological properties of electroactive material play a crucial role in achieving the capacitance value and serving as an association of resistors and capacitors.

Figure 2.20 illustrates a Nyquist plot with equivalent circuits and involves the following circuit elements: R_s: ohmic resistance, R_s+R_{ct}: charge transfer resistance, CPE: constant phase element and W: Warburg impedance element. The EIS technique is essential because it determines the frequency dependent and independent electrical components from Nyquist plot. Equivalent circuit models based on basic electric circuit elements such as capacitors and resistors are used to simulate complicated electrochemical processes near the electrode-electrolyte interface **[68]**. Components of equivalent circuits and the equations of their current-voltage relationships are illustrated in **Table 2.1**.

Table 2.1: Common electrical elements.

Component	Current Vs. Voltage	Impedance
Resistor	E= IR	Z = R
Inductor	E = L di/dt	Z = jωL
Capacitor	I = C dE/dt	Z = 1/jωC

The oxygen evolution reaction (OER) is considered to occur with numerous elementary multi-step reactions such as adsorption, dissociation, charge-transfer and desorption. Each of these elementary reactions is expected to contribute some particular resistance to the overall operation, also called polarization. To perform an insightful analysis of the oxygen evolution reaction at the thin film electrocatalysts in the present study, electrochemical impedance spectroscopy (EIS) is employed. Impedance is nothing but the AC resistance of the cell, which consists of imaginary and real parts. The electrochemical cell contains resistive, capacitive and inductive properties. Resistive properties involve in the real part, while capacitive and inductive properties involve in the imaginary part. Figure 2.20 represents a typical Nyquist plot obtained from EIS. Where Z' and Z" represent the real and imaginary parts of EIS, respectively. The intercept of Nyquist plot to the X-axis (i.e. real part) in the lower frequency region represents the solution resistance (R_s). While the intercept in the higher frequency region represents the sum of a solution resistance (R_s) and charge transfer resistance (R_{ct}). Hence the diameter of the semicircle is nothing but R_{ct}. EIS in present study is measured with a nominal root-mean-square amplitude potential (V_{rms}) of 10 mV, in the frequency range of 0.1 MHz to 10 mHz. The Warburg impedance is smaller at higher frequencies, because the diffusing reactant does not need to go very far. Also, real-axis intercept (at high frequencies) corresponds to the ohmic resistance. At lower frequencies, the reactors have to diffuse more distance, increases the Warburg-impedance. In Nyquist plot, Warburg impedance described by diagonal line with an inclination of 45° arises due to mass transport of ions.

All electrochemical tests mentioned above (section 2.3.2) were analysed using ZIVE MP_1 electrochemical workstation. The EIS measurement was performed at AC amplitude of 5 mV in between frequency range of 0.01 Hz to 0.1 MHz at bias potential of open circuit potential.

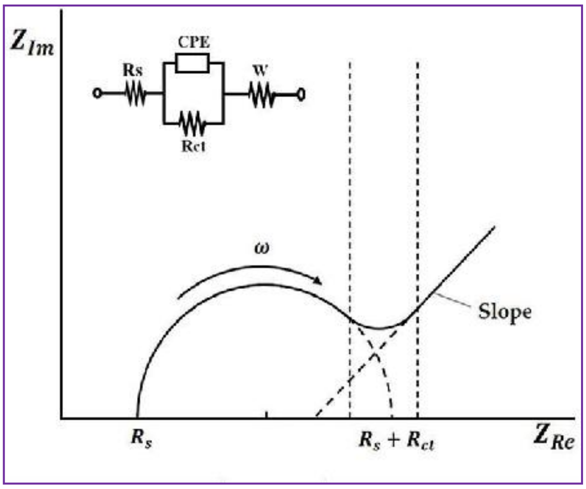

Figure 2.20: A Nyquist plot with electrical equivalent circuit.

2.4 References:

[1] W. Zhang and K. Zhou, Small, 13 (2017) 1700806-1700824.

[2] L. E. Murr, Handbook of materials structures, Properties, Processing and Performance, Switzerland: Springer International Publishing, (2016) 1-13. https://link.springer.com/978-3-319-01815-7.

[3] M. Benelmekkia, and A. Erbe, Nanostructured thin films-Fundamentals and applications, 14 (2019) 1-24, https/bookseries/frontiers-of-nanoscience/vol/14/suppl/C

[4] I. Gurrappa, L. Binder, Sci. Technol. Adv. Mater. 9 (2008) 43001 (1-11), https://doi.org/10.1088/1468-6996/9/4/043001.

[5] L. B. Freund and S. Suresh: Thin Film Materials: Stress, Defect Formation and Surface Evolution (Cambridge University Press, Cambridge, U.K., 2004), DOI:10.1017/CBO9780511754715.

[6] K. Chopra, and I. Kaur, Thin film Device Application, Plenum Press, New York (1983), pp. 101.

[7] C. Lokhande, Mater. Chem. Phys., 27 (1991) 1-43.

[8] Z. Cao, Thin Film Growth, Woodhead publishing series in electronic and optical materials, (2011) 185-210.

[9] J. L. Robins, Appl. Surf. Sci., 33 (1988) 379-394.

[10] M. Ristov, G. J. Sinadinovski, I. Grozdanov, Thin solid films, 123 (1985) 63-67.

[11] Y. Nicolau and J. Menard, J. Cryst. Growth, 92 (1988) 128-142.

[12] Y. Nicolau, Appl. Surf. Sci., 22 (1985) 1061- 1074.

[13] M. Birkholz, P. F. Fewster, C. Genzel, Thin film analysis by X-ray scattering,

Wiley-VCH, 71 (2006) 1-30.

[14] V. Petkov, Mater. Today, 11 (2008) 28-38.

[15] http://xrd.co/component-parts-x-ray-diffractometer.

[16] https://www.rigaku.com/products/xrd/miniflex.

[17] B. Cullity, “Elements of X-rays Diffraction”, Second ed., Addison-Wesley, London (1978).

[18] https://www.findlight.net/blog/2019/03/27/ftir-principles-applications/

[19] https://WWW.sigmaaldrich.com/technical-documents/articles/biology/ir-spectrumtable.html#ir-table-by-compound.

[20]https://www.bruker.com/products/infrared-near-infrared-and-manspectroscopy/ft-ir-routine-spectrometers/compact-ftir-alpha-ii.html.

[21] A. Munajad, C. Subroto, Suwarno, Energies, 11 (2018) 364-376.

[22] https://en.wikipedia.org/wiki/Raman_spectroscopy.

[23] I. Ebenezar, S. Ramalingam, C. Raja, P. Prabakar, J. Nano. Adv. Mat., 2 (2014) 11-25.

[24] J. Breier, S. White, C. German, Phil. Trans. R. Soc. A, 368 (2010) 3067-3086.

[25] A. Downes, A. Elfick, Sensors, 10 (2010) 1871-1889.

[26] https://bwtek.com/raman-components-of-a-raman-spectrometer/

[27] https://www.mt.com/in/en/home/applications/L1_AutoChem_Applications/Raman-Spectroscopy.html

[28] H. Vašková, International journal of mathematical models and methods in applied sciences, 5 (2011) 1205-1212, https://www.naun.org/main/NAUN/ijmmas/17- 120.pdf.

[29] https://www.thermofisher.com/blog/microscopy/sputter-coating-for-sem how this sample-preparation-technique-assists-your-imaging/.

[30] A. Mayeen, L. Shaji, A. Nair, N. Kalarikkal, Morphological Characterization of Nanomaterials, Advances and key technologies, micro and nano technologies, (2018) 335-364.

[31] Y. Jusman, S. C. Ng, N. A. A. Osman, Sci. World J., (2014) 1-11, DOI: 10.1155/2014/289817.

[32] http://mcff.mtu.edu/acmal/electronmicroscopy/FE_Form_Function.html.

[33] Y. Jusman, S. C. Ng, N. A. A. Osman, Sci. World J., (2014) 1-11, DOI: 10.1155/2014/289817.

[34] https://epm.univie.ac.at/fileadmin/user_upload/p_epm/xps-machine.png.

[35] http://www.ramehart.com/790.htm.

[36] M. Vadiyar, S. Bhise, S. Patil, S. Kolekar, A. Shelke, N. Deshpande, J. Chang, K. Ghule, A. Ghule, Chem. Commun., Chem. Commun., 52 (2016) 2557-2560.

[37] T. Chau, W. Bruckard, P. Koh, A. Nguyen, Adv. Colloid Interface Sci., 150 (2009) 106-115.

[38] P. Sinha, A. Datar, C. Jeong, X. Deng, Y. G. Chung, L. Lin, J. Phys. Chem. C, 123 (2019) 20195- 20209.

[39] http://www.pharmacopeia.cn/v29240/usp29nf24s0_c846.html.

[40] D. Lapham, J. Lapham, Int. J. Pharm., 568 (2019) 118522-118566.

[41] A. Forse, C. Merlet, J. Griffin, C. Grey, J. Am. Chem. Soc., 138 (2016) 5731-5744

[42] A. Afif, S. M. Rahman, A. T. Azad, J. Zaini, M. A. Islan, A. K. Azad, J. Energy Storage, 25 (2019) 100852-100876.

[43] Y. Wu, C. Cao, Sci. China Mater., 61 (2018) 1517-1526.

[44] V. Climent, J. M. Feliu, Annu. Rev. Anal. Chem., 13 (2020) 201-222.

[45] M. Portales, A. Fraga, A. García, O. García-Zaldívar, A. Barranco, M. Frutis, J. Solid State Electrochem., 22 (2018) 471–478.

[46] A. Wardak, and H. Tien, Bioelectrochem. Bioenerg., 24 (1990) 1- 11.

[47] H. Qu, M. Harada, T. Okada, Chem Electro Chem, 4 (2017) 35-38.

[48] C. Peng, G. Snook, D. Fray, M. Shaffer, G. Chen, Chem. Commun., 44 (2006) 4629-4631.

[49] R. Bushby, O. Lozman, L. Mason, N. Taylor, S. Kumar, Mol. Cryst. Liq. Cryst., 410 (2004) 171-181.

[50] D. Qazzazie, O. Yurchenko, S. Urban, J. Kieninger, G. Urban, Nanoscale, 9 (2017) 6436-6447.

[51] C. Zoski, Handbook of electrochemistry, Elsevier Science, Netherland, (2006) 1-934, DOI:10.1016/B978-0-444-51958-0.X5000-9

[52] C. McCrory, S. Jung, J. Peters, T. Jaramillo, J. Am. Chem. Soc. 135 (2013) 16977–16987.

[53] C. Ray, S. C. Lee, K. Sankar, B. Jin, J. Lee, J. Park, S. Jun, ACS Appl. Mater. Interfaces., 9 (2017) 37739–37749.

[54] R. Salunkhe, Y. Kaneti, Y. Yamauchi, ACS Nano, 11 (2017) 5293-5308.

[55] P. Veerakumar, A. Sangili, S. Manavalan, P. Thanasekaran, K. Lin, Ind. Eng. Chem. Res., 59 (2020) 6347- 6374.

[56] http://www.michaelsharris.com/electronics/images/capRCcurve.gif.

[57] K. Kumar, N. Choudhary, Y. Jung, J. Thomas, ACS Energy Lett., 3 (2018) 482-495.

[58] K. Breitsprecher, C. Holm, S. Kondrat, ACS Nano, 12 (2018) 9733-9741.

[59] N. Chodankar, H. Pham, A. Nanjundan, J. Fernando, K. Jayaramulu, D. Golberg, Y. Han, D. Dubal, Small, 16 (2020) 2002806-2002841.

[60] C. Mccrory, S. Jung, J. C. Peters, T. Jaramillo, J. Am. Chem. Soc., 135 (2013) 16977–16987.

[61] B. Mei, O. Munteshari, J. Lau, B. Dunn, L. Pilon, J. Phys. Chem. C, 122 (2018) 194- 206.

[62] D. K. Kampouris, X. Ji, E. P. Randviira, C. E. Banks, RSC Adv., 5 (2015) 12782- 12791.

CHAPTER-3

Synthesis, characterization, supercapacitive and electrocatalytic performance of cobalt tungsten oxide thin film electrode

CHAPTER 3

Synthesis, characterization, supercapacitive and electrocatalytic performance of cobalt tungsten oxide thin film electrode

SECTION-A

Synthesis and characterization of $CoWO_4$ thin films

SECTION -B

Supercapacitive evaluation of $CoWO_4$ thin films

SECTION -C

Electrochemical characterizations of $CoWO_4$ thin films for OER

3.1 Introduction:

The upcoming global energy crisis requires moderated solutions in terms of energy storage and conversion that can lift the continuously increasing energy demands. As of now, supercapacitors are being considered the face of the energy storage solution which possess ability to fulfill energy demands. In addition, the portable electronic devices and many new generation systems are being investigated which requires the energy storage system to have safety and long cycle life. Therefore, different materials are being studied vastly for the supercapacitor application [1].

There are basically EDLC type and pseudocapacitive type materials which mainly differs by their charge storing mechanism. However, current global supercapacitor market largely rely on the supercapacitors based on EDLC type material. Though, EDLC type materials have good stability, they do not reach up to capacitance showed by pseudocapacitive materials. Therefore, it is needed to study and develop an asymmetric device having EDLC as well as pseudocapacitive type material that could exhibit high capacitance, moderated energy density, high stability as well as long cycle life [2].

On the other hand, energy conversion also plays an important role for the generation and supply of clean energy. In that context, H_2 generated through electrolysis possess potential application towards the large scale production. The side product of the electrolysis is O_2 which is also very useful in medical as well as other fields. The O_2 is generated through oxygen evolution reaction (OER) in which electro-oxidation takes place at the anode that generates O_2. However, this OER can be accelerated by using suitable catalyst that can enhance the rate of electrolysis. The performance of a catalyst is measured on the basis of overpotential required for the generation of O_2. Therefore, a suitable electrocatalyst plays a crucial role in the generation of O_2 through electrolysis [3].

The literature illustrates vast materials for the purpose of supercapacitor as well as OER. Several inorganic materials have shown their promising applicability towards the respective applications. Many ELDC and pseudocapacitive type materials are employed for supercapacitor while RuO_2 and IrO_2 have proved their excellent usage for OER. In addition, different synthesis strategies have been employed to prepare various nanostructured materials including CBD, SILAR, hydrothermal etc. that have significantly changed the structural, morphological and electrical properties of the material in order to enhance the performance [4]. However, scarce literature on a single material can be found showing good applicability towards supercapacitor as well as OER applications. Therefore, it is important to find a material that can shows good performance for both the applications. In that context, $CoWO_4$ material has recently gained much attention due to its favorable physico-chemical properties for both the applications. Literature shows the synthesis of $CoWO_4$ by various methods for the application of supercapacitor as well as OER.

Among the metal tungstates, $CoWO_4$ is a p-type semiconductor compound which exhibit outstanding catalytic and electrochemical properties [5]. It shows high chemical stability and possesses narrow size distribution with excellent phase composition. Due to optical features, it has been utilized as an efficient photocatalyst for environmental restoration. It exhibits superior electrochemical properties than Co_3O_4material owing to the multiple valence states of Co, and W as well as higher electrical conductivity [6]. Thus, $CoWO_4$ is favorable electrode supercapacitor. Li et al. [7] reported the preparation of $CoWO_4$ nanoparticles via hydrothermal method in the mixture of deionized water and ethylene glycol as a solvent and achieved Cs of 1817.14 F g^{-1} at a current density of 1 A g^{-1}. Lokhande and Ji [8] prepared $CoWO_4$ by hydrothermal process and reported C_s of 1372 F g^{-1} at a scan rate of 5 mV s^{-1}. Chen et al. [9] used hydrothermal method to deposit $CoWO_4$ on nickel foam substrate and 1 M KOH as an electrolyte used to study of supercapacitor properties The C_s found to be 1127.6 F g^{-1} with energy density 48 Wh Kg^{-1} and power density 365 kW $kg^{-1.}$ Stability was found to be 92.4 % for 3000 cycles. Ding et al. [10] prepared $Co_3O_4/CoWO_4$ powder by hydrothermal method and reported C_s of 331.6 F g^{-1} with 70.2 % stability for 2000 cycles.

The $CoWO_4$ is quite competitive material to metal oxide and metal hydroxide due to its electrochemical properties. Cobalt tungsten oxide has been investigated for its catalytic activity for OER. Karkera et al. [11] formed Cobalt– Manganese Tungstate on Ni mesh by hydrothermal a novel oxygen evolution anode in basic media. It needs overpotential of 400 mV to drive current density of 10 mA cm^{-2} and its Tafel slope is 84 mV dec^{-1}. Luo et al. [12] deposited $CoWO_4$ on carbon paper using electrodeposition method and obtained an overpotential 306 mV with 72 mV dec^{-1} Tafel slope. Rani et al. [13] formed mixed metal tungstate XWO_4 (X= Co, Mn) and reported an overpotential 310 mv for $CoWO_4$. The present chapter deals with the synthesis of $CoWO_4$ thin films by SILAR method and their characterization.

SECTION - A

Synthesis and characterization of $CoWO_4$ thin films

3.2A.1 Introduction:

To be considered as a good electrochemical electrode, the electrode material must be inexpensive, scalable processing, high performance with high power density, energy density and good electrochemical rate capability. From these point of view, $CoWO_4$ electrodes are synthesized by simple, binder–less and low temperature SILAR method.

The SILAR is also an effective method for deposition by layer-by-layer assembling of material with easily control over the thin film thickness and large scale area of on any type of substrate without use of binders [14]. It is based on successive reaction on the substrate surface using different reacting precursor and hence unnecessary bulk precipitation is avoided. In SILAR method, rapid growth rate results into inappropriate thickness, therefore reaction rate should be controlled.

3.2.A.2. Experimental details:

3.2.A.2.1 Cleaning substrate:

A substrate with an impurity is responsible for the uncontrolled growth of material and results in the deposition of a non-uniform thin film. Therefore, substrate cleaning is critical for uniform film deposition. In this work, stainless steel (SS) is as used as a substrate.

The procedure used for the SS substrate cleaning is as follow,

Step 1: The SS substrate is wiped with acetone to remove the dirt,

Step 2: The SS substrate is mirror polished using zero grade polish paper,

Step 3: After polishing, the substrate is cleaned with double distilled water (DDW); and

Step 4: Finally, the substrate is ultrasonically cleaned in DDW for 15 minutes and dried at room temperature.

3.2.A.2.2 Chemicals:

Analytical grade cobalt chloride ($CoCl_2 \cdot 6H_2O$), sodium tungstate ($Na_2WO_4.2H_2O$) and potassium hydroxide (KOH) were purchased from S. D. Fine Chem. Ltd. and used without further purification. The SS substrates of thickness 0.5 mm (purchased from a local supplier) were used for film deposition. The KOH (Sigma Aldrich, USA) was used to prepare an aqueous electrolyte. The DDW was used throughout the experiment.

3.2.A.2.3 Synthesis of $CoWO_4$ thin films using SILAR method:

The $CoWO_4$ thin films were synthesized using AR grade cobalt chloride hexahydrate ($CoCl_2.6H_2O$) and sodium tungstate ($Na_2WO_4.2H_2O$) chemicals using SILAR method on SS substrate of 1 × 5 cm^2 dimensions. Solutions of 0.1 M $CoCl_2.6H_2O$ and 0.1 M Na_2WO_4 were employed as cationic and anionic precursors, respectively. The SS substrate was first dipped into Co^{2+} ion containing solution for adsorption process for 15 s. Then, the substrate was rinsed in DDW for 15 s to remove loosely adsorbed Co^{2+} ions. Furthermore, the substrate was dipped in anionic precursor for 15 s, where WO_4^{2-} ions reacted with preadsorbed Co^{2+} ions to form $CoWO_4$ layer. Again, SS substrate was rinsed in DDW for 15 s to remove loosely bounded $CoWO_4$ molecules. Ideally in SILAR process, only a single layer of material is deposited on the substrate in one cycle of deposition. Thus, a single SILAR cycle forms a layer of $CoWO_4$; and such 120 cycles results in uniform and adherent thin film. Figure. 3.1A shows photograph of SILAR machine used to deposit thin film electrodes in the present study.

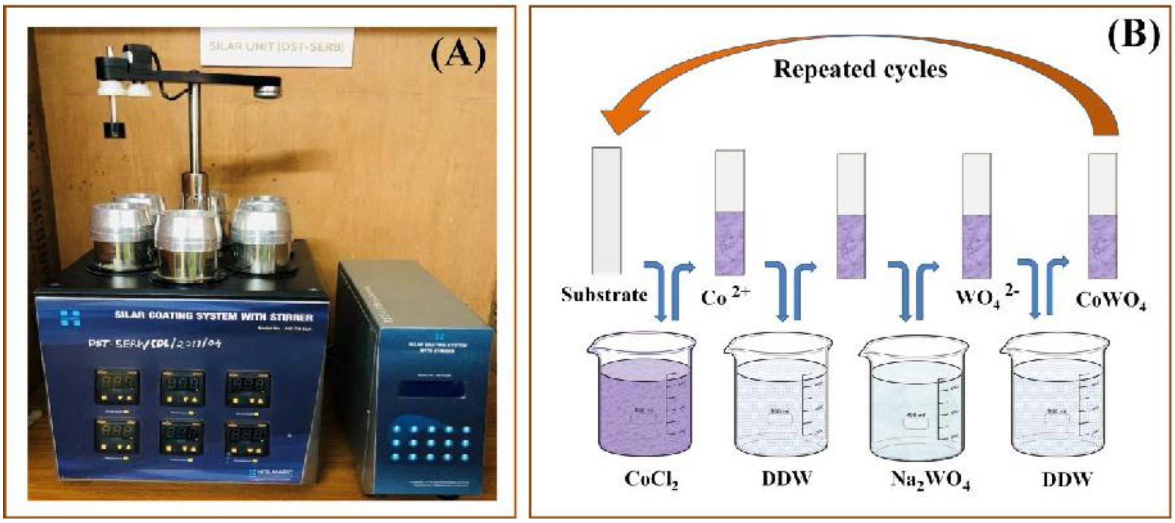

Figure 3.1: A) Photograph of SILAR unit used to deposit thin film electrodes in the present study, and B) schematic of SILAR method deposition of $CoWO_4$ thin film.

Further, Figure 3.1B shows schematic of deposition of $CoWO_4$ thin film by SILAR method. In $CoWO_4$ thin film formation, ion-by-ion type deposition occurs via nucleation sites over the substrate surface. The optimized preparative parameters; such as concentration of anionic and cationic solutions, adsorption, rinsing and reaction time periods, and total number of deposition cycles are summarized in Table 3.1.

Table 3.1: Optimized preparative parameters for deposition of $CoWO_4$ thin film by SILAR method.

Cationic solution	**0.1M $CoCl_2$ (pH = 4.60)**
Anionic solution	**0.1M Na_2WO_4 (pH = 10.00)**
Adsorption time in cationic solution (cobalt chloride)	**15 s**
Reaction time in anionic solution (sodium tungstate)	**15 s**
Rinsing time in 2nd and 4th beakers	**15 s**
Number of deposition cycles	**60, 90, 120, 150**

3.2.A.2.4 $CoWO_4$ Film formation mechanism:

The thin film growth process in SILAR method is ion-by-ion adsorption at nucleation sites on the immersed surface [4]. $CoWO_4$ thin film was developed by immersing the substrate in individually placed cationic and anionic precursors with rinsing between every immersion. The thin film growth is ion-by-ion adsorption at nucleation sites on the immersed surface. The first precursor consists of Co^{2+} ions with pH ~ 4.6. The formation of Co^{2+} can be represented as,

$$CoCl_2 \rightarrow Co^{2+} + Cl^{2-} \qquad 3.1$$

When SS substrate is immersed in cobalt chloride ($CoCl_2$) solution, Co^{2+} ions are adsorbed onto SS surface due to adhesive force and van der valls force on the surface of a substrate. In the next step, a substrate is rinsed in DDW for removal of loosely adsorbed Co^{2+} ions. Further reaction is followed by immersion of the substrate in Na_2WO_4 anionic solution consisting of WO_4^{2-} ions. The formation of WO_4^{2-} ions can be represented as,

$$Na_2WO_4 \rightarrow Na^{2+} + WO_4^{2-} \qquad 3.2$$

The chemical reaction between Co^{2+} and WO_4^{2-} ions leads to the formation of $CoWO_4$ thin film as,

$$Co^{2+} + WO_4^{2-} \rightarrow CoWO_4 \qquad 3.3$$

Then $CoWO_4$ thin film was rinsed in DDW to remove loosely bounded $CoWO_4$ molecules from the substrate.

In SILAR method, thin film deposition proceeds in four different successive steps viz. nucleation, aggregation, coalescence and growth of particle. In the first step, nucleation takes place by the adsorption and reaction of Co^{2+} ions with WO_4^- ions on the substrate which forms the nuclei required for the nucleation. This process facilitates the nucleation process by providing enough ions to form the crystallites. Further, these nucleation sites act as platform for the aggregation of particles by attracting other cobalt and tungstate ions present in the solutions. In the next step, these particles are merged with each other to form the larger particles. This process is known as coalescence where all the small particles gather to form a large crystallites of cobalt tungsten oxide. In the last step, the film formation takes place by the stacking of layers of cobalt and tungstate ions giving rise to the growth of $CoWO_4$ in thin film form.

3.2.A.2.5 Thickness measurement:

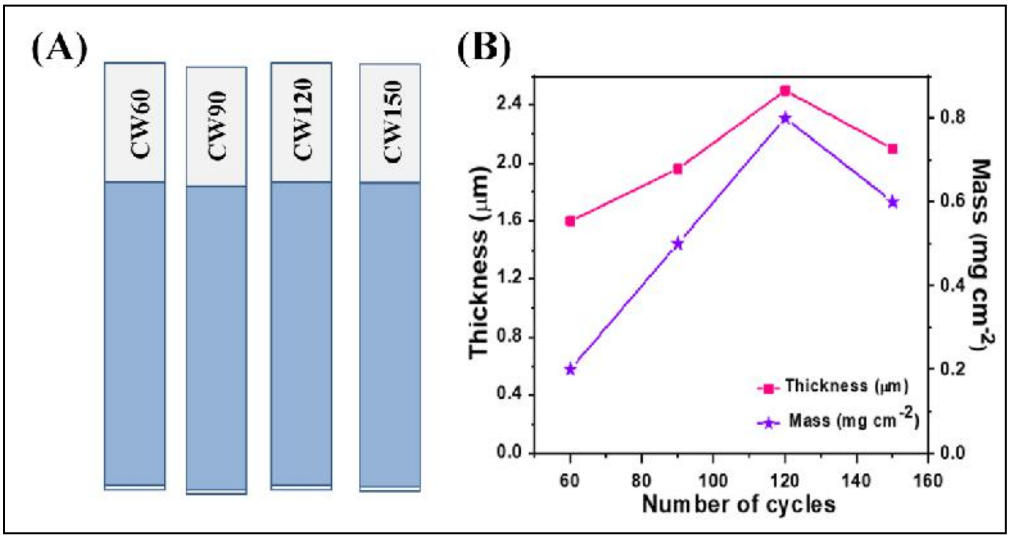

Figure 3.2: A) Photograph of cobalt tungstate thin film electrodes prepared at different SILAR deposition cycles, and B) Graphical representation of thickness variation with mass deposited of $CoWO_4$ on SS substrate at 60 (CW60), 90 (CW90), 120 (CW120) and 150 (CW150) SILAR deposition cycles.

The thickness of the film is important since it influences electrochemical properties of thin film electrode. The accurate measurement of $CoWO_4$ film thickness was not possible due to the rough morphology and porosity. The thickness of $CoWO_4$ thin film was determined by weight difference method using bulk density of $CoWO_4$

as (8.42 g.cm^{-3}). Photograph of cobalt tungstate deposited using different SILAR cycles shown in Figure 3.2A. The graphs of thickness and mass loading of $CoWO_4$ with deposition cycles are illustrated in Figure 3.2B.

The loaded mass of $CoWO_4$ material was measured for 60, 90, 120, and 150 cycles as 0.2, 0.5, 0.8, 0.6 mg cm^{-2}, respectively. Consequently, the film thickness increases up to 0.8 µm for 120 cycles and decreases after 150 cycles due to the formation of nonadherent particles on the surface. The thickness of film increases with the number of cycles; however, once the thickness reaches its threshold value, it decreases. In thin films, the adherency of the film tends to decrease upon certain thickness due to overgrowth [15].

3.2.A.2.6 $CoWO_4$ thin film Characterization:

For determination of crystal structure of synthesized material, X-ray diffraction (XRD) technique (Rigaku 600 miniflex) was used. The valence states and chemical composition of $CoWO_4$ film were studied using X-ray photoelectron spectrometer (XPS). The Fourier transform infrared (FT-IR) spectrum was recorded using Alpha (II) Bruker unit. The surface morphology of film was observed using field emission scanning electron microscope (FE-SEM) unit. The electrical resistivity was measured using two point probe method. The surface area and pore size distribution of film material were analyzed using Brunauer-Emmett-Teller (BET) and Barrette-Joyner-Halenda (BJH) techniques, respectively. The Rame-Hart instrument was used to find out water contact angle of thin film electrode. The electrochemical performance of $CoWO_4$ thin film electrode was studied in 1 M KOH electrolyte using ZIVE MP1 electrochemical workstation.

3.2.A.3 Results and discussion:

3.2.A.3.1 XRD analysis:

The X-ray diffraction patterns of bare SS substrate and $CoWO_4$ thin films deposited on SS substrates at different SILAR deposition cycles are shown in Figure 3.3A. All the samples have a similar diffraction patterns. The diffraction peaks at are well matched to the (110), (011), (-111), (002), (-102), (-202), (-113) and (-311) planes of monoclinic structure of $CoWO_4$ (JCPDS card no. 01-072-0479). The peaks shown by an asterisk (*) in the pattern are of SS substrate. The thickness of $CoWO_4$ thin films increases with an increase in the number of deposition cycles. Therefore, with an increase in deposition cycles, the intensity of the diffraction peaks of SS substrate gradually decreases while the intensity of diffraction peaks from $CoWO_4$

increases. The presence of sharp and intense diffraction peaks in XRD pattern of CW120 indicates its high crystallinity. Also, the absence of any other additional peaks demonstrates the high purity of $CoWO_4$.

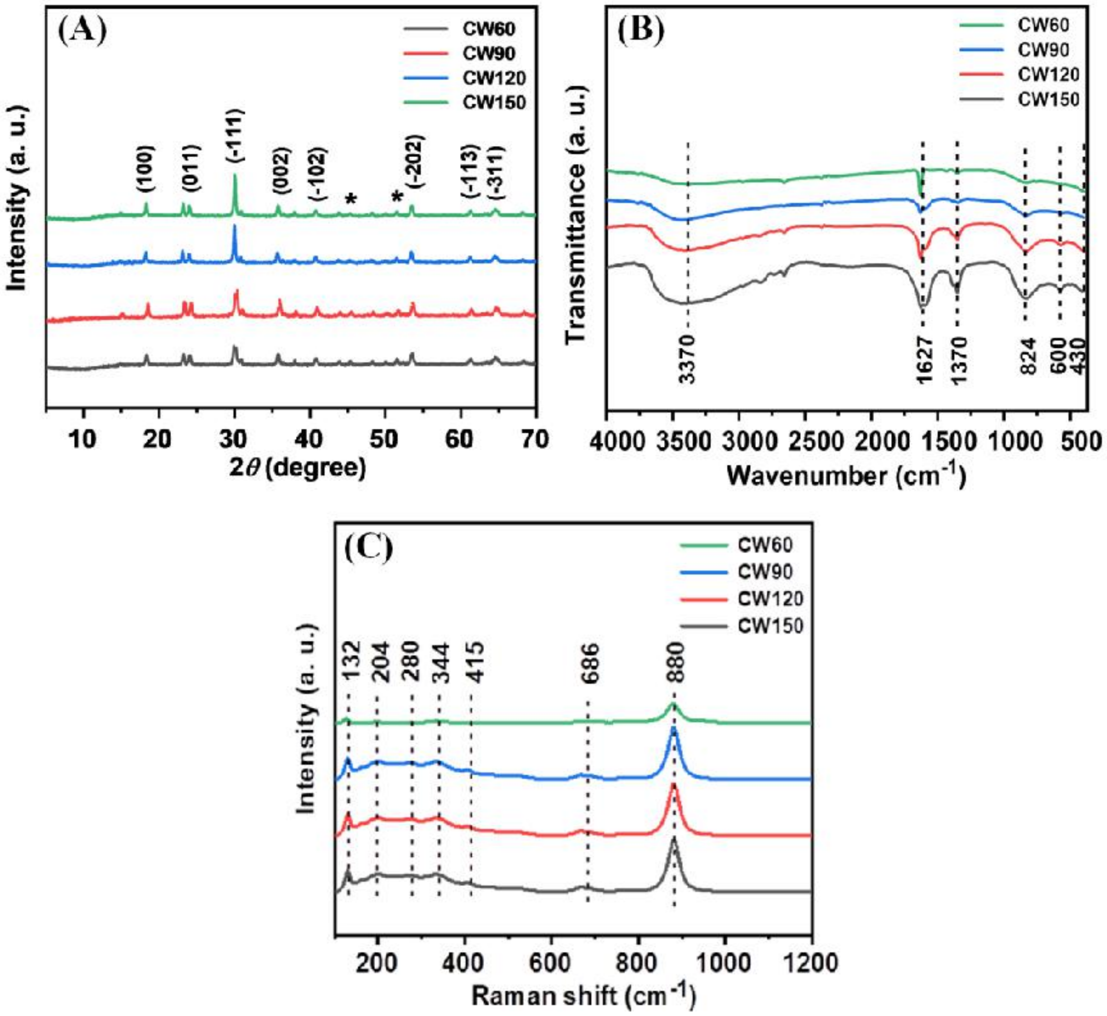

Figure 3.3: A) The XRD patterns, B) FT-IR spectra, and C) Raman spectra of $CoWO_4$ series thin films prepared at different deposition cycles.

3.2.A.3.2 FT-IR study:

The molecular bond vibrations in $CoWO_4$ thin films deposited at 60, 90, 120, and 150 cycles were investigated using FT-IR. The FT-IR absorption spectra in the wavenumber range of 4000-400 cm^{-1}of $CoWO_4$ are shown in Figure 3.3B. The narrow bands of Co–O along with W–O and W–O–W observed in the low frequency region (400–1000 cm^{-1}) [16]. The absorption bands at 450 cm^{-1} belong to the deformation modes of W-O bands in WO_4. The band at 604 cm^{-1} represents Co-O stretching mode whereas the adsorption band at 822 cm^{-1} highlights W-O-W stretching vibrational mode [17]. The presence of moisture leads to the band formation at 1388 cm^{-1}

corrosponding to the –OH group. The peak at 1633 cm^{-1} is due to the bending mode of H–O–H from structural water. The strong intense band of the -OH stretching vibration observed between wavelength of 3000–3800 cm^{-1} is due to surface adsorbed and structural water [18]. Thus, FT-IR spectrum analysis confirms formation of hydrous $CoWO_4$ material on the substrate.

3.2.A.3.3 Raman analysis:

The structure of cobalt tungstate material was studied using Raman spectrum. The strength of bonding between the molecular structure and constituent atoms were evaluated from Raman spectrum. In the case of $CoWO_4$, Co-O bonds have the same bond length and W-O bonds have an asymmetric nature. The distorted crystal structure forms due to asymmetric bonds. Therefore, the Raman spectrum is influenced by tungstate octahedron peaks [19]. Figure 3.3C displays Raman spectra of $CoWO_4$ series revealing seven peaks confirming the formation of $CoWO_4$ on SS substrate. All peaks correspond exactly to the characteristic monoclinic $CoWO_4$ active modes reported in the literature [20]. The main peak at 880 cm^{-1} resembles to W=O bond originated due to symmetrical stretching vibration. The peak of 686 cm^{-1} depicts O–W–O bond originated due to asymmetric stretching vibration. The weak peaks observed at 415 and 344 cm^{-1} shows deformation and rotation indicating bridging W–O bonds. The stretching vibration of Co–O bond is observed at 280 cm^{-1} [21]. The lowest wavelength peak seen at 204 cm^{-1} is related to the off-plane vibration. Therefore, the formation of $CoWO_4$ nanostructures is supported by Raman spectra studies [22].

3.2.A.3.4 Field emission scanning electron microscopy:

It is known that, the performance of active material extensively depends on morphology of electrode material. The material with microstructured morphology may improve specific surface area allowing easy adsorption/desorption of electrolytic ions that enhances electrochemical performance of the electrode. Figure 3.4 shows FE-SEM images of $CoWO_4$ thin films at two magnifications (10,000X and 25,000X). The images show the correlation between the deposition cycles and morphology of surface. The irregular arrangement of particles took place due to higher reaction kinetics at alkaline baths where grain growth as well as nucleation occur together. The FE-SEM images of CW60 film exhibited in Figure 3.4A and B, illustrate sponge-like porous structure containing uniform nanoparticles. FE-SEM micrographs of CW90 thin film shown in Figure 3.4C and D indicate that the microstructure of thin film is

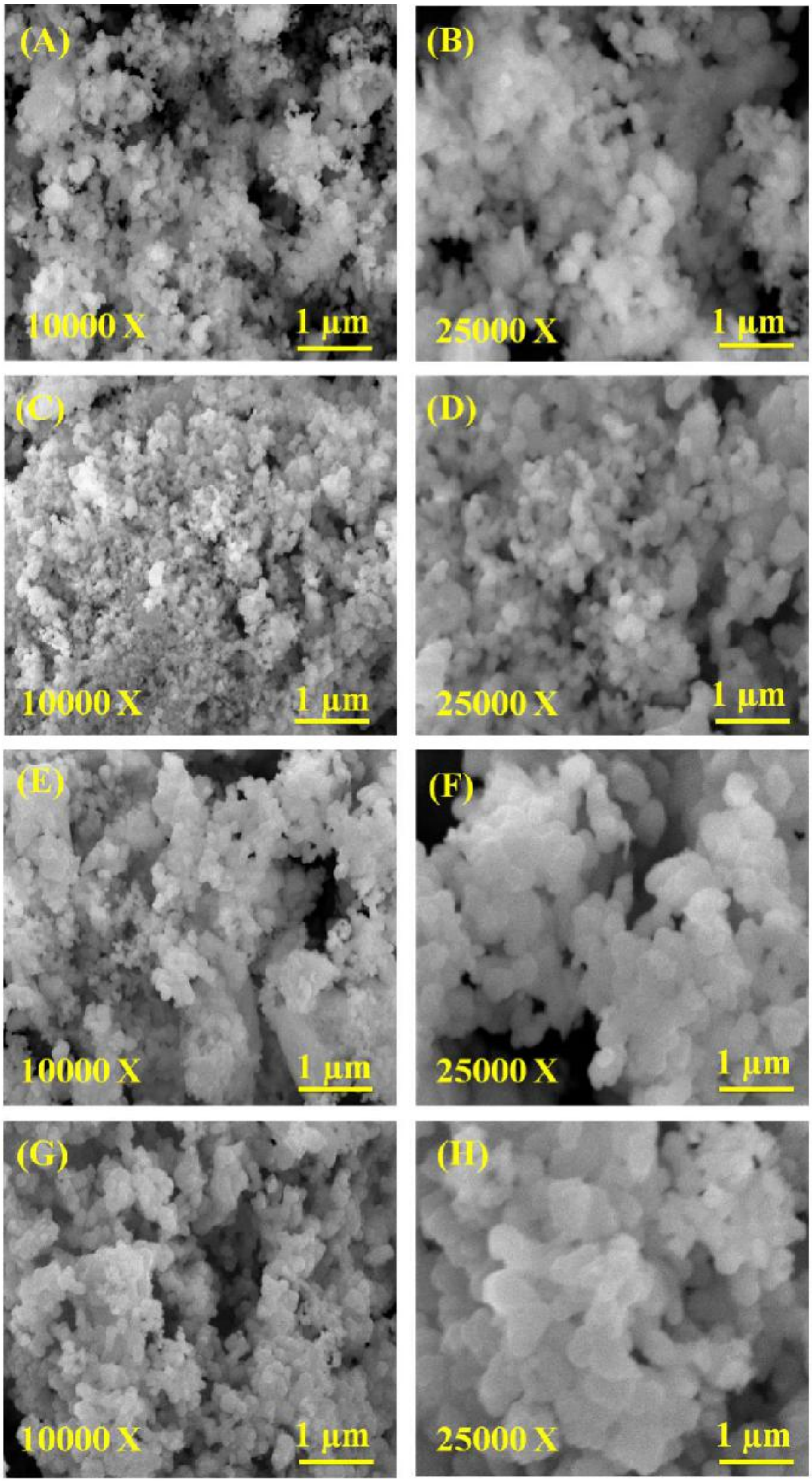

Figure 3.4: The FE-SEM images of $CoWO_4$ thin films deposited at different SILAR cycles, (A, B) CW60, (C, D) CW90, (E, F) CW120 and (G, H) CW150 at 10,000 X and 25,000 X magnifications.

affected with deposition cycles. Figure 3.4E and F represent spongy nanospherical-like structures connected to each other. As the deposition cycle of $CoWO_4$ (CW120 thin film) increases, morphologically similar spherical nanoparticles are obtained with some individual hypertrophic particles showing overgrown nanoparticles with a compact morphology. Most crucially, spherical nanoparticles are connected to each other, which efficiently help to carry electrons through the active material to the current collector.

Similarly, CW150 thin film (Figure 3.4G and H) indicates a cluster of nanoparticles, indicating that the sample consists of overgrown nanoparticles with an uneven porous structure having compact morphology. Most importantly, the spherical nanoparticles are interconnected with each other, which help efficiently to carry electrons from active material to the current collector.

3.2.A.3.5 EDAX study:

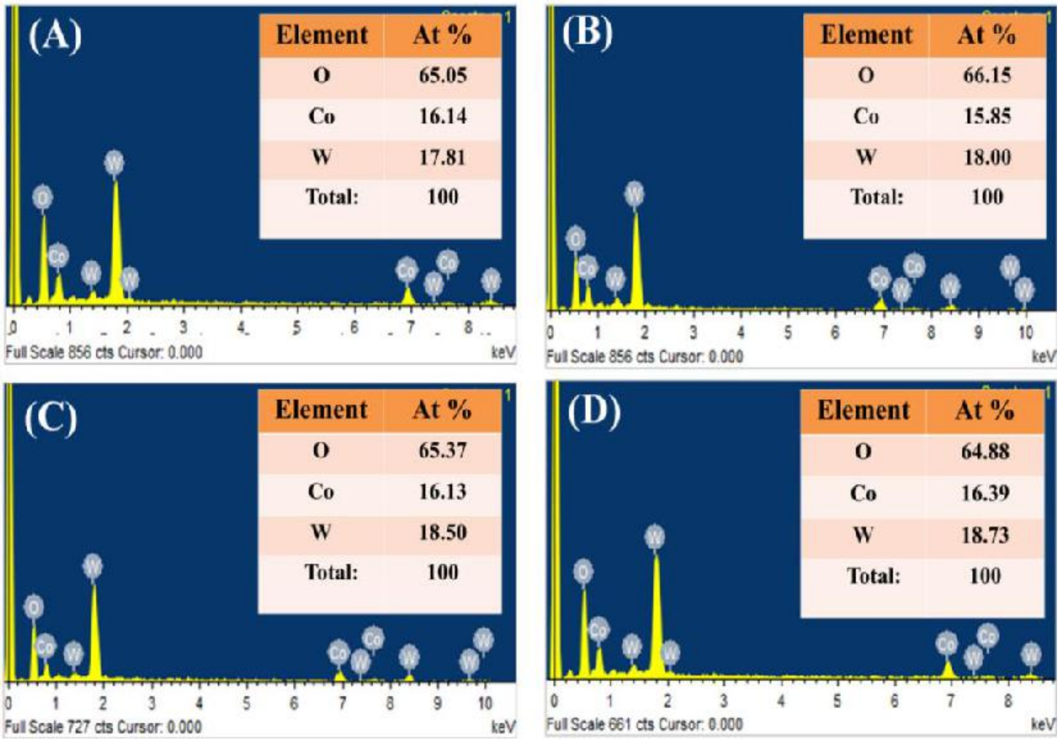

Figure 3.5: The EDAX spectra of A) CW60, B) CW90, C) CW120, and D) CW150 thin films (Insets show atomic percentages of constituting elements of $CoWO_4$ thin film).

The energy dispersive X-ray analysis (EDAX) plays an important role to find out composition in the thin film material. The chemical composition of $CoWO_4$ thin films was investigated by EDAX and presented in Figure 3.5A-D. The EDAX spectra confirm the presence of Co, W and O elements in a material without any other impurity. The atomic percentage of Co in CW120 thin film is 16.13%, O is 65.37%, and that of W is 18.50%. The atomic percentage of constituting elements for $CoWO_4$ thin films is shown in inset of each image, shows uniform distribution of each elements in the thin film. The $CoWO_4$ thin film formation was confirmed from the EDAX analysis.

3.2.A.3.6 Contact angle measurement:

The surface wettability is one of the important parameter that affects the electrocatalytic performance of an electrode. Therefore, the wettability study of the $CoWO_4$ thin films was carried out using contact angle measurement. The contact angles vary according to thin film content, surface morphology, particle size, cleanliness, porosity, and surface roughness [23].

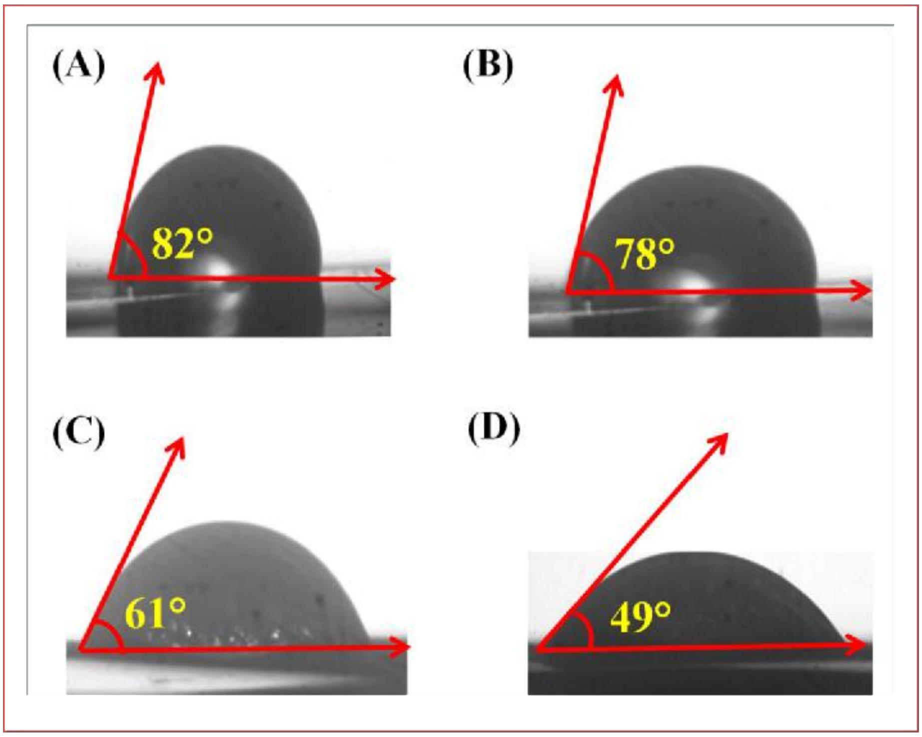

Figure 3.6: Contact angle images of A) CW60, B) CW90, C) CW120, and D) CW150 thin films.

The images showing contact angles for CW60, CW90, CW120, and CW150 are displayed in Figure 3.6 having values of 78, 61, 45 and 30°, respectively. Because of the diverse morphologies, diverse contact angles are obtained. The material nature keeps effective contact at electrode electrolyte interface that leads to minimal resistance for transfer of charge. The rough morphology of $CoWO_4$ thin film brings about higher hydrophilicity. In general, maximum interaction between electrode and electrolyte is desirable for optimal performance in case of electrochemical established applications [24]. Therefore, superior supercapacitive and electrocatalytic behavior can be forecasted for film presenting at small contact angle (sample CW120).

3.2.A.3.7 BET study:

The high specific surface area of the material enhances the rate of reactions owing to increased number of reaction sites on materials surface [25]. The specific surface area of $CoWO_4$ nanoparticles along with pore size distribution was examined at 77 K using BET and BJH techniques, respectively. The N_2 adsorption isotherms of CW120 in the relative pressure between 0 to 1.0 are shown in Figure.3.7A. The nature of isotherm (type IV) suggests the presence of mesopores structure of $CoWO_4$. The specific surface area of CW120 is 60 $m^2 g^{-1}$ signifies the applicability of SILAR method for the preparation of $CoWO_4$ electrode material with high surface area. Zhang et al. [26] prepared $CoWO_4$ by hydrothermal method and reported specific surface area of 49.3 $m^2 g^{-1}$. The BJH curve presenting pore size distribution curve of CW120 is shown in Figure 3.7B. The observed average pore radius 1.8 nm is smaller than the previous reports of $CoWO_4$; such as Taneja et al. [27] reported an average pore radius (12.68 nm) for $CoWO_4$ material synthesized by hydrothermal method. Room temperature synthesis and precise control over reaction in SILAR method enable preparation of microporous $CoWO_4$ material. Lower average pore size and higher specific surface area are beneficial for electrochemical reactions which provide more electroactive sites.

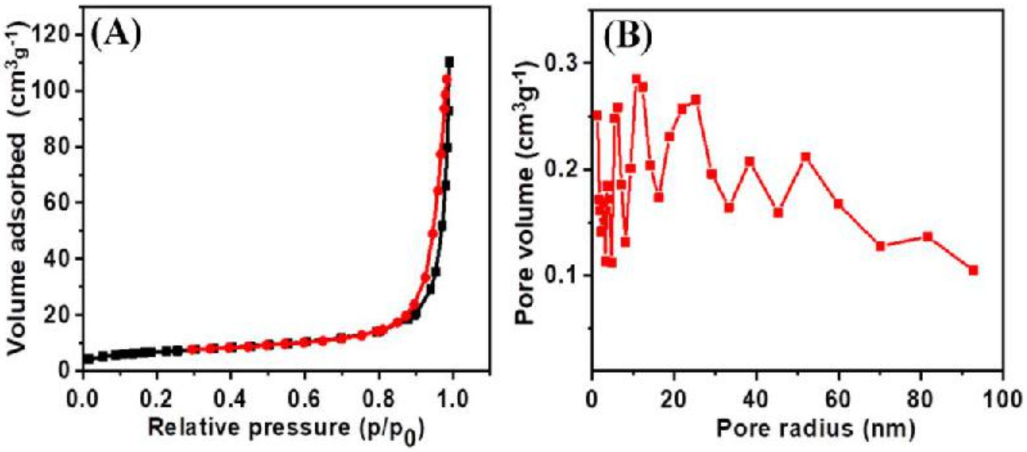

Figure 3.7: A) Nitrogen adsorption – desorption isotherms, and B) pore size distribution curve of CW120 thin film.

3.2.A.3.8 XPS study:

The oxidation states and chemical components in CW120 thin film were identified using XPS technique. The wide survey scan of CW120 thin film is presented in Figure 3.8A. The presence of Co2p, O1s, and W4f peaks in the spectrum confirms possible formation of $CoWO_4$. The deconvoluted spectrum of Co2p is shown in Figure3.8B.For Co2p, the binding energies for Co $2p_{1/2}$ and Co $2p_{3/2}$ are noted at 796.87 and 780.71 eV, respectively. The difference between the binding energies (BE) of Co $2p_{1/2}$ and Co $2p_{3/2}$ is characteristic of the chemical state of the cobalt ion. For instance, Co $2p_{1/2}$ − Co $2p_{3/2} \approx 16$ eV resembles the presence of Co^{2+} ions, whereas a BE difference of ∼15 eV signifies that the presence of Co^{3+} ions.

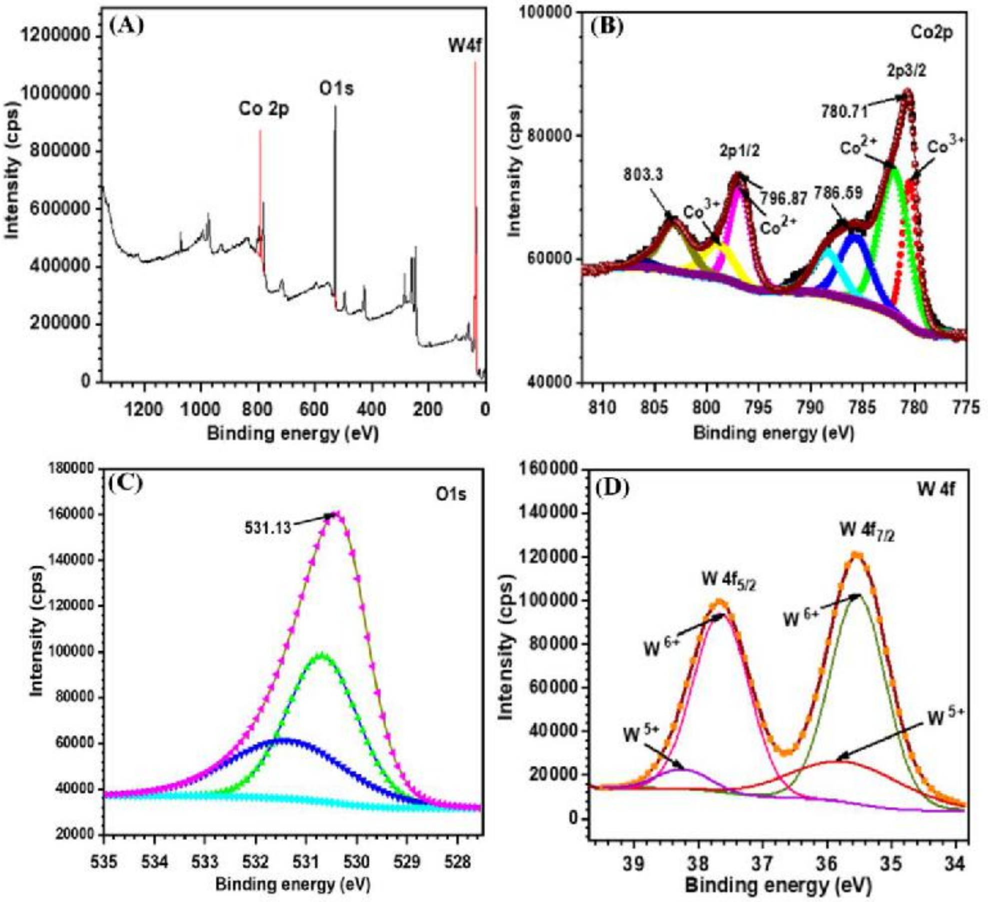

Figure 3.8: The XPS spectra of CW120 thin film: A) survey spectrum, B) Co2p spectrum, C) W4f spectrum, and D) O1s spectrum.

In this study, the difference in BE is noted to be ∼16 eV, revealing the existence of Co^{2+} ions. In addition, the corresponding satellite peaks appeared at 803.3 and 786.59 eV for Co $2p_{1/2}$ and Co $2p_{3/2}$, respectively, which further confirms the presence of Co^{2+} ions [28, 29]. As illustrated in Figure 3.8C, the spectrum of O1s shows major peak at 531.13 eV corrosponding to the metal oxygen bond [30]. Figure 3.8D shows W4f spectrum which is disassembled in to four peaks correspond to W^{6+} and W^{5+} state. The binding energies of 37.65 and 35.53 eVs refering to the $W4f_{5/2}$ and $W4f_{7/2}$ states of W^{6+}, while the peaks at 36.01 and 38.26 eV correspond to W^{5+}. The binding energy values observed for tungsten are close to those reported for WO_3, confirming tungsten to be in a hexavalent state. The spin orbits separation of 2.09 eV indicates good arrangement for W with +6 valance in the compound [31]. The formation of $CoWO_4$ is thus confirmed by XPS results.

SECTION – B

Supercapacitive evaluation of $CoWO_4$ thin films by SILAR method

3.2. B. 1 Introduction

The present section deals with the electrochemical measurements of SILAR prepared $CoWO_4$ thin films in 1 M KOH. This section includes the CV, GCD and EIS measurements. These electrochemical tests are essential to decide the superior electrode material for fabrication of supercapacitor device. Moreover, the effect of scan rate, current density and electrochemical durability of $CoWO_4$ thin films are investigated.

3.2.B.2 Experimental setup for supercapacitative measurements:

For investigation of electrochemical measurements of $CoWO_4$ thin films, the three electrode system was used which includes $CoWO_4$ thin film, platinum plate and saturated calomel electrode (SCE) as a working electrode, counter electrode and reference electrode, respectively in 1 M KOH electrolyte. The working electrode area was 1 cm^2. Figure 3.9 (A, B) show the actual experimental set up and schematic for the electrochemical study, respectively. The supercapacitive properties of $CoWO_4$ electrode such as C_s, E_D, P_D, and electrochemical stability were studied using CV, GCD and EIS techniques. The CV and GCD studies were conducted using ZIVE MP1 electrochemical workstation in the range of frequency from 0.001 Hz to 1 MHz with AC amplitude of 10 mV.

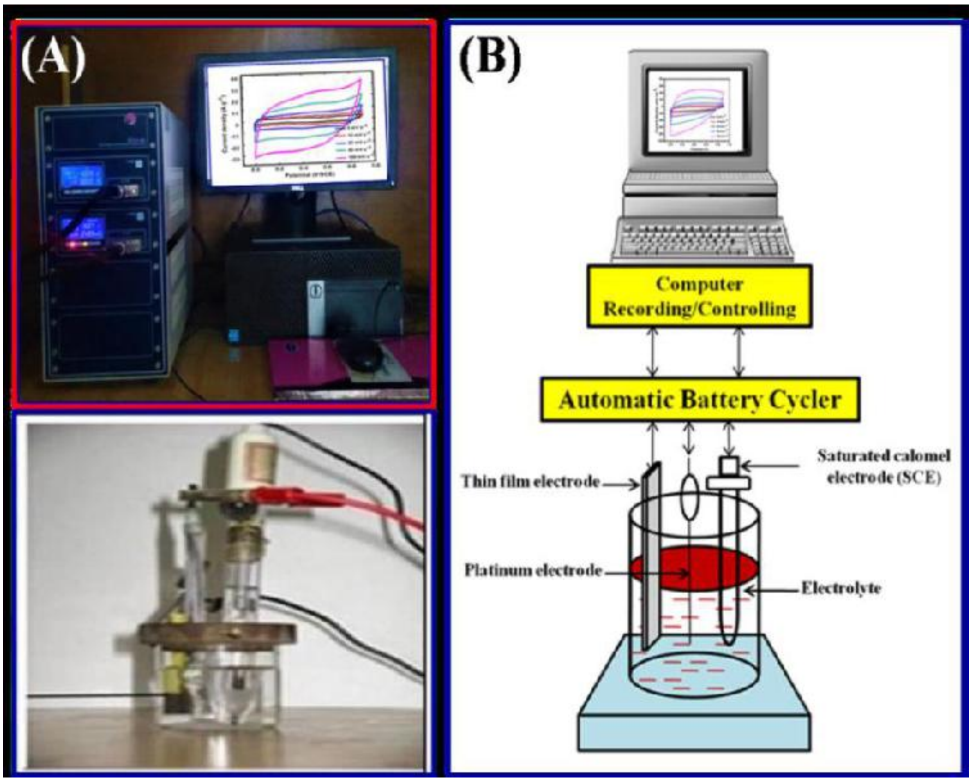

Figure 3.9. A) Experimental setup consisting of (up) automatic battery cycler with CV cycles graph on monitor and (down) three electrode system and B) schematic representation of three electrode system.

3.2.B.3 Results and discussion:

3.2.B.3.1 The CV study:

Figure 3.10A shows the CV curves of CW60, CW90, CW120, and CW150 electrodes at scan rates of 100 mV s^{-1} in the potential window of 0 to +0.65 V/SCE. The shape of all CV curves reflects a nearly symmetric and rectangular shape, similar to the ideal capacitive behavior. From CV curves, it is seen that strong oxidation and reduction peaks for $CoWO_4$ arise at a potential of -0.57 and -0.79 V/SCE, respectively. The area under CV curves is directly proportional to the scan rate. The current response of CW120 film electrode in CV curves is more, indicating CW120 may facilitate fast electronic and ionic transport. The increase in current passing through the scan rate exhibits the exceptional use of electrode substance with electrolyte owing the electrochemical reaction [32].

The effect of scan rate on specific capacitance is illustrated in Figure 3.10 B**.** The maximum values of C_s observed for CW60, CW90, CW120, and CW150 electrodes are 304, 482, 714 and 590 F g^{-1}, respectively at 5 mV s^{-1} scan rate. At a lower scan rate, K^+ ions from KOH electrolyte take more time for intercalation/deintercalation reaction, which gives more charge transfer during a low scan rate compared with higher scan rates.

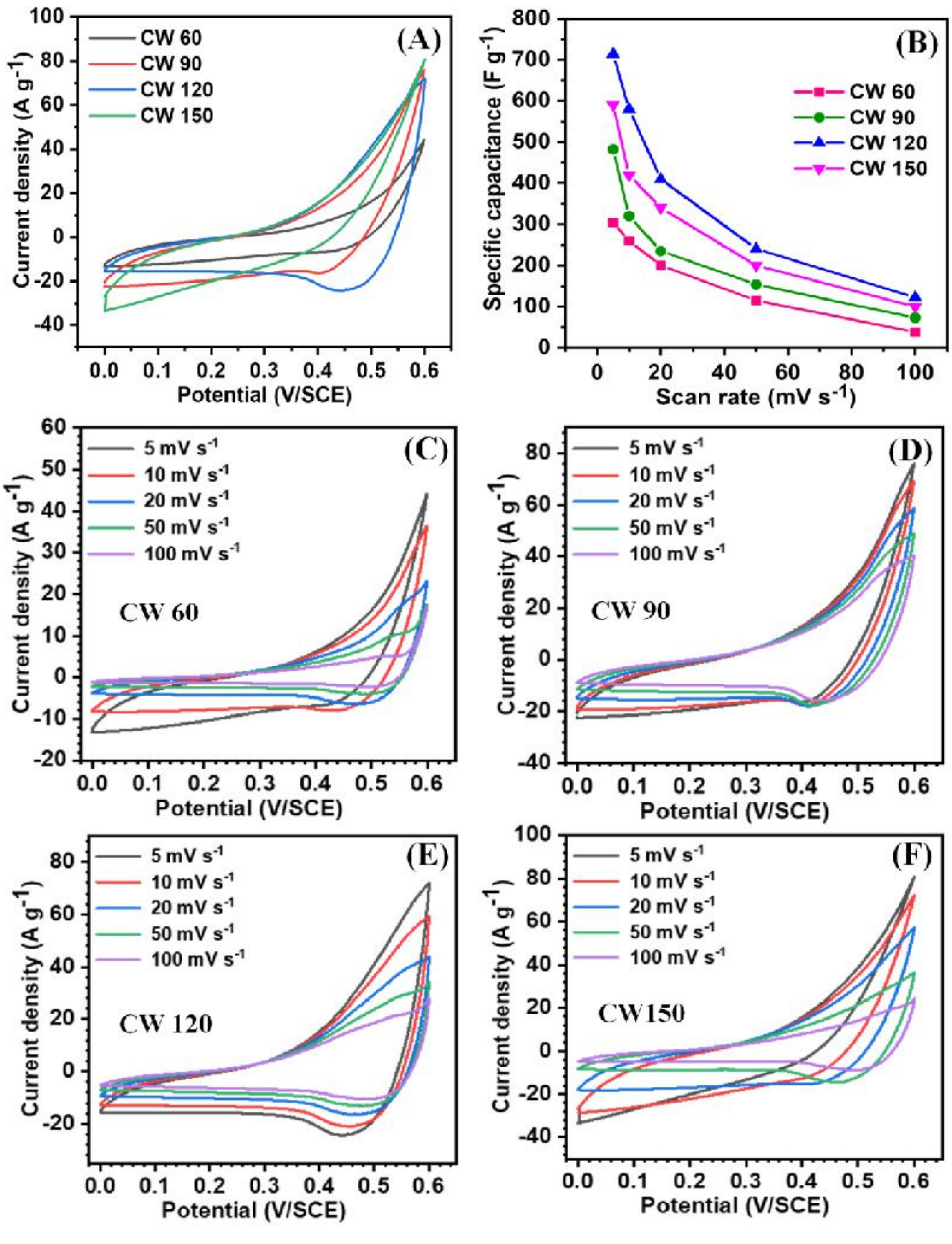

Figure 3.10. A) Comparative CV curves of $CoWO_4$ thin films at a scan rate of 100 mV s^{-1}, B) variation of C_s with the scan rates, and the CV curves at various scan rates from 5- 100 mV s^{-1} of C) CW60, D) CW90, E) CW120, and F) CW150 thin film electrodes.

The decrease in C_s with a rise in a scan rate is due to the least time available for reversible redox reactions at higher scan rate. At higher scan rate, all the electrolyte ions do not undergo reversible redox reaction due to time constraint so C_s decreases with the scan rate. The increase in current response with the scan rate is observed for all thin film electrodes. From the CV curves it is concluded that $CoWO_4$ thin film electrodes may be used as an electrode material at various current ratings. The CV curves of CW60, CW90, CW120, and CW150 thin film electrodes at different scan rates from 5 to 100 mV s^{-1} are shown in Figure 3.10C-F. The increase in current response with the scan rate is observed for all thin film electrodes. From the CV curves one can conclude that $CoWO_4$ thin film electrodes can be used as an electrode material at various current ratings.

3.2.B.3.2 The GCD study:

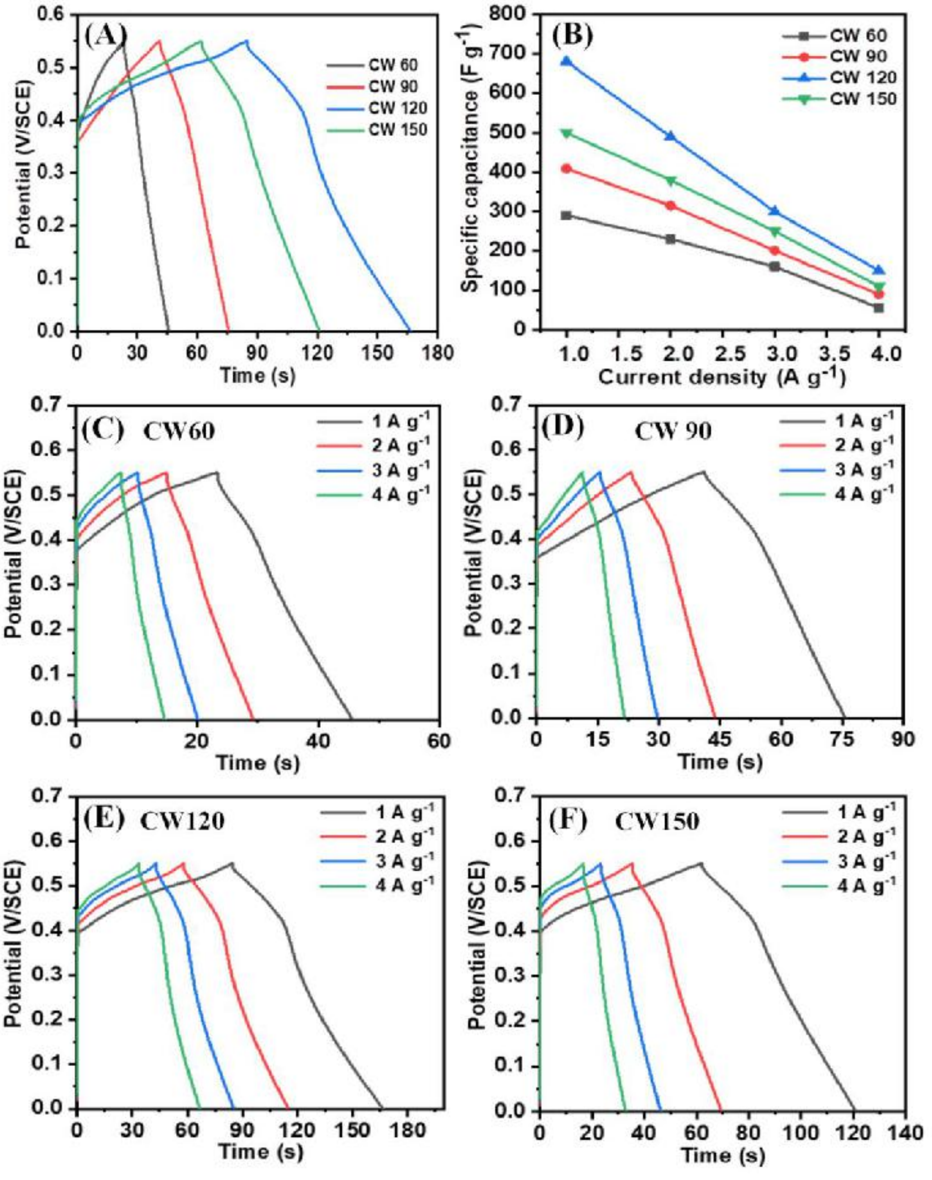

Figure 3.11: A) Comparative GCD curves of $CoWO_4$ thin film electrodes at a current density of 1 A g^{-1}, B) variation of C_s with the current densities, and the GCD curves at

various current densities from 1-5 A g^{-1} C) CW60, D) CW90, E) CW120, and F) CW150 thin film electrodes.

The GCD curves at a current density of 1 A g^{-1} for $CoWO_4$ electrodes deposited at 60, 90, 120, and 150 cycles are shown in Figure 3.11A. The GCD profile of $CoWO_4$ film electrode is nontriangular indicates charge storage from the surface redox reactions [33]. The values of C_s calculated using Eq. 2.7 are 290, 409, 680 and 500 F g^{-1} for CW60, CW90, CW120, and CW150 film electrodes at charge discharge current density of 1 A g^{-1}. The easy ion transfer path is delivered by the surface of the electrode, which changes the intercalation/deintercalation rate by decreasing the internal resistance (IR) of material [34]. Variation of C_s with the current density is shown in Figure 3.11B.

An increase in IR and time constraint for the reversible redox reactions at higher applied current densities cause a decrease in C_s with rising applied current density. The GCD plots of CW60, CW90, CW120, and CW150 electrodes at different current densities are shown in Figures 3.11C-F. The nontriangular GCD profiles suggest that charge storage is of the pseudocapacitive type. The highest discharge time is observed for CW120 electrode compared with other electrodes, which indicate excellent electrochemical performance.

3.2.B.3.3 Stability study:

The stability was investigated for all $CoWO_4$ electrodes over 3000 GCD cycles at a current density of 5 A g^{-1} and the capacitive retention plot for CW120 is presented in Figure 3.12. The capacitive retention for CW120 electrode is 94%. As the thickness of film electrode increases, more electrochemical stability of the film electrode was observed.

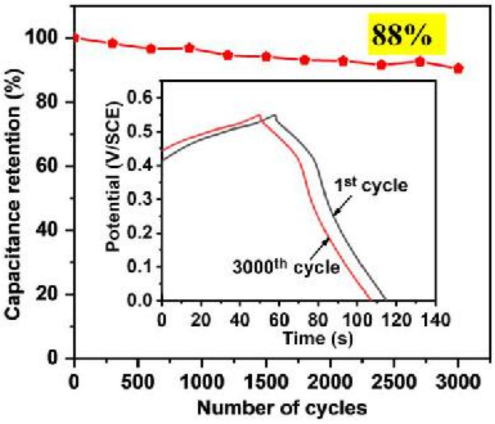

Figure 3.12: Capacitance retention for CW120 electrode for 3000 repeated GCD cycles (Inset GCD curves at 1st and 3000th cycles).

SECTION – C

Electrochemical characterizations of $CoWO_4$ thin films for OER

3.2.C.1 Introduction:

The present section deals with the electrochemical measurements of SILAR prepared $CoWO_4$ thin films in 1 M KOH. This section includes the LSV, Tafel slope, ECSA, and EIS measurements. These electrochemical tests are essential to decide the superior electrode material for electrocatalytic performance. Moreover, the effect of overpotential, current density and electrochemical durability of $CoWO_4$ thin films are investigated.

3.2.C.2 Electrochemical characterization:

3.2.C.2.1 LSV and Tafel slope:

The OER activity of $CoWO_4$ thin film electrodes was evaluated by performing linear sweep voltammetry (LSV) in 1 M KOH solution. The potential of working electrodes was swept linearly from 1.1 to 1.7 V vs RHE at a 2 mV s^{-1} scan rate. The LSV of bare SS substrate was also measured at similar conditions, to compare the performance of $CoWO_4$ thin film electrodes. The obtained LSV curves are shown in Figure 3.13A. The catalytic activity is measured in terms of overpotential, calculated using equation (2.9) (given in the previous chapter), required to achieve a current density of 10 mA cm^{-2}. The overpotential required for bare SS substrate to reach 100 mA cm^{-2} current density is 500 mV. The absence of any active material, hence catalytically active sites, bare SS substrate requires such high overpotential to reach benchmarking current density. The value of overpotential further decreases with an increase in deposition cycles. $CoWO_4$ deposited with 60 and 90, 120, and 150 SILAR cycles i.e., CW60 and CW90, CW120, and CW150 require 420, 370, 320 and 340 mV overpotential to reach 100 mA cm^{-2} current density is shown in Figure 3.13B. For the $CoWO_4$ thin film electrode deposited with 120 deposition cycles, 320 mV overpotential is required to reach 100 mA cm^{-2} current density. When compared with bare SS substrate, there is a decrement in overpotential due to the deposition of $CoWO_4$.

Hence, the electrochemical OER activity increases with an increase in the number of SILAR cycles. The high overpotential of bare SS substrate than $CoWO_4$ thin film electrode suggests poor catalytic activity of bare SS substrate. Therefore, it can be concluded that SS substrate does not contribute to the catalytic performance of thin film material. It is observed in the LSV curves, as the number of deposition cycles increases, the current density at higher potentials (> 1.48 V vs RHE) also increases. The mass loading of $CoWO_4$ has increased with increase in the number of SILAR cycles. Also, at a scan rate of 2 mV s^{-1}, the electrolyte gets sufficient time to interact with electrode material, as well as the diffusion of electrolyte into electrode is maximum.

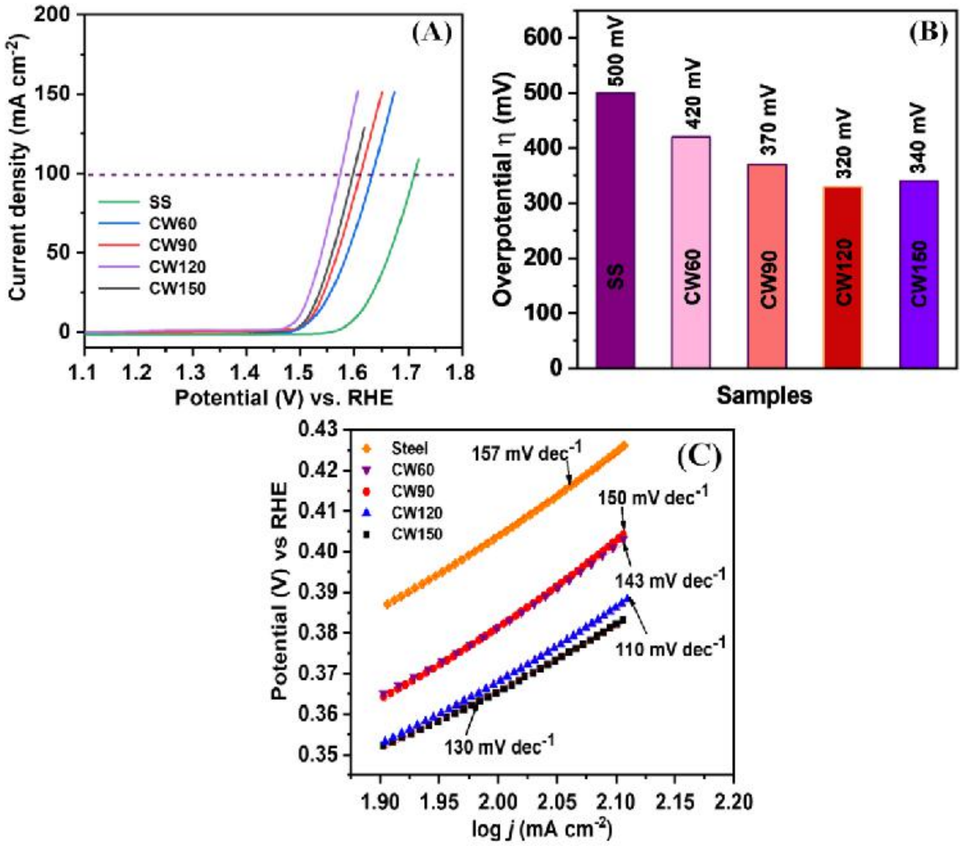

Figure 3.13: A) The polarization curves at the scan rate of 1 mV s^{-1}, B) overpotential values for CW catalyst at 100 mA cm^{-2}, and C) Tafel plots extracted from LSV curves of $CoWO_4$ thin film electrocatalysts prepared at different deposition cycles.

Hence, the interaction of electrolyte and electrode material increases with the increase in the number of deposition cycles. Therefore, the current density increases with number of deposition cycles of $CoWO_4$. These results suggest the importance of optimization of mass loading of active material on substrate. To extract the Tafel slope from LSV curve, the current density is first converted into a logarithmic scale. The log of current density is then plotted against overpotential (by subtracting 1.23 V from measured values). The resultant graph is called the Tafel plot. The Tafel plots for all $CoWO_4$ thin film electrodes are shown in Figure 3.13C. The slope of these Tafel plots is nothing but the corresponding Tafel slope. The bare SS substrate possesses a Tafel slope of 157 mV dec^{-1}. While, A**)** CW60, B) CW90, C) CW120, and D) CW150 electrodes possess 150, 143, 110 and 130 mV dec^{-1} Tafel slopes, respectively. This indicates fast reaction kinetics with increasing deposition cycles. The large Tafel slope of bare SS substrate than $CoWO_4$ thin film electrocatalysts may be due to the absence of any catalytically active material and hence catalytically active sites. Hence, $CoWO_4$ thin film electrocatalysts deposited with 120 SILAR cycles i.e. CW120 required low overpotential and have fast reaction kinetics than others. A rough and porous surface of CW120 might have provided more catalytically active sites open to the electrolyte, due to which the total OER reaction increases than other electrodes.

3.2.C.2.2 Electrochemical active surface area:

The electrochemically active surface area (ECSA) of $CoWO_4$ thin film electrocatalysts is estimated from the electrochemical double-layer capacitance (C_{dl}). To obtain C_{dl}, cyclic voltammetry (CV) at varied scan rates (25-125 mV s^{-1}) is performed in a narrow potential window of +1.0 to +.1.15 V vs RHE, where no faradic reaction is observed. The obtained CV curves at different scan rates for all electrocatalysts are shown in Figure 3.14 (A-D). In this potential window, the current is generated only for charging of a double layer. From CV curves, the current density is measured @ 1.31 V vs. RHE and plotted as a function of scan rate, as shown in Figure 3.15. The plots show linear nature and slope of it is nothing but the 'C_{dl}' [35].

The 'C_{dl}' can be further converted into ECSA using the specific capacitance value of a standard 1 cm^2 flat surface which is normally between 0.02-0.06 mF cm^{-2} for alkaline medium [34]. Therefore, an average value of 0.04 mF cm^{-2} is used in the calculation by equation (2.3). The values of ECSA obtained for samples CW60, CW90, CW120, and CW150 are 2.8, 6.15, 8.22, 11.36 and 12.16 cm^2, respectively. Hence, cobalt tungsten oxide thin film electrocatalyst deposited with 120 SILAR cycles i.e. CW120 possess higher ECSA. The higher ECSA value of sample CW120 compared to other electrodes can be attributed to the surface roughness. The rough and porous morphology of CW120 probably has more open sites than the smooth texture which acts as catalytic active sites. Figure 3.15 shows current density vs. scan rate plots obtained from CV curves for A) CW60, B) CW90, C) CW120 and D) CW150. The values of C_{dl} are 0.10, 0.13, 0.24, and 0.17 mF cm^{-2} or CW60, CW90, CW120, and CW150 thin film electrodes, respectively.

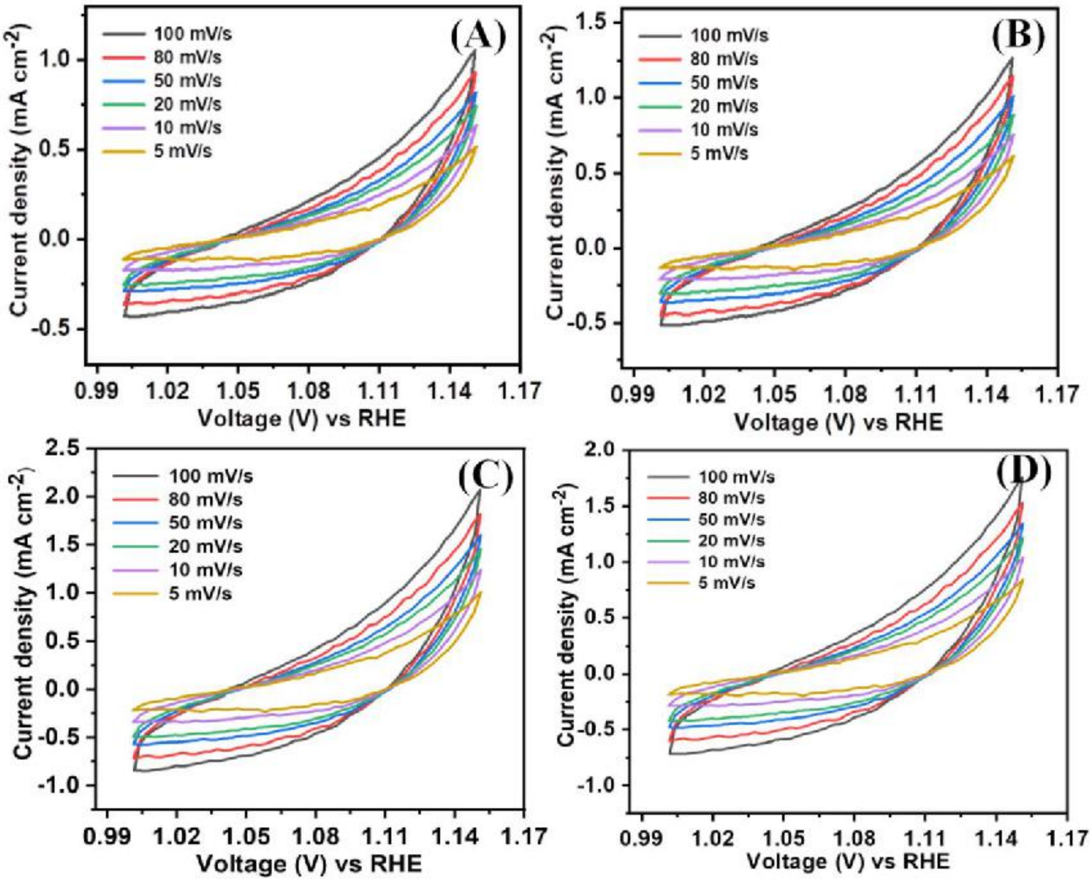

Figure 3.14: The CV curves in a potential window of +1.1 to +1.15 V vs RHE for A) CW60, B) CW90, C) CW120 and D) CW150.

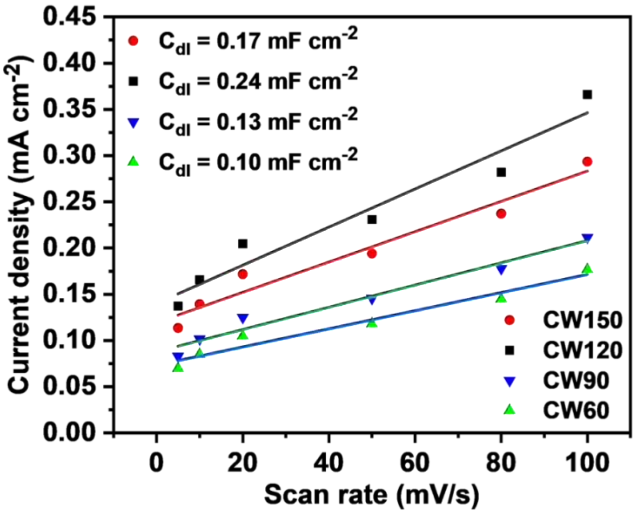

Figure 3.15: Current density vs. scan rate plots obtained from CV curves for A) CW60, B) CW90, C) CW120 and D) CW150.

3.2.C.2.3. Electrochemical impedance spectroscopy and stability:

The electron and charge transferability during the electrochemical process is studied using the electrochemical impedance spectroscopy (EIS) technique. The Figure

3.16 shows the Nyquist plots of A) CW60, B) CW90, C) CW120 and D) CW150 electrodes in frequency range of 0.1 kHz to 1 MHz with bias potential 10 mV. All Nyquist plots consists of partial semicircle in high frequency region and straight line in low frequency region. The slope of straight line in the low frequency region at 45º gives Warburg resistance (W). The Nyquist plots of $CoWO_4$ display the small semicircle in the high frequency region indicating the low series resistance (R_s) and charge transfer resistance (R_{ct}). This is mainly ascribed to its good diffusion rate due to higher surface area. The solution resistance (R_s) values of 0.69, 0.65, 0.67, and 0.70 Ω cm^{-2} and charge transfer resistance (R_{ct}) of 44.98, 48.71, 55.90 and 83.80 Ω cm^{-2} are observed for CW60, CW90, CW120 and CW150 electrodes, respectively. The Zview EIS data analysis software was used for experimental data fitting and the fitted values are provided in Table 2. The smaller R_{ct} values signify faster charge transfer between electrode and electrolyte. As known, the smaller R_{ct} means faster charge transfer rate in the reversible reaction between electrode and electrolyte. Therefore, being a CW120 electrode of smaller R_{ct} among all samples has superior charge transfer rate. The high specific surface area can increase charge transfer rate, enhance contact area between electrode and electrolyte, so as to decrease the charge transfer resistance [20].

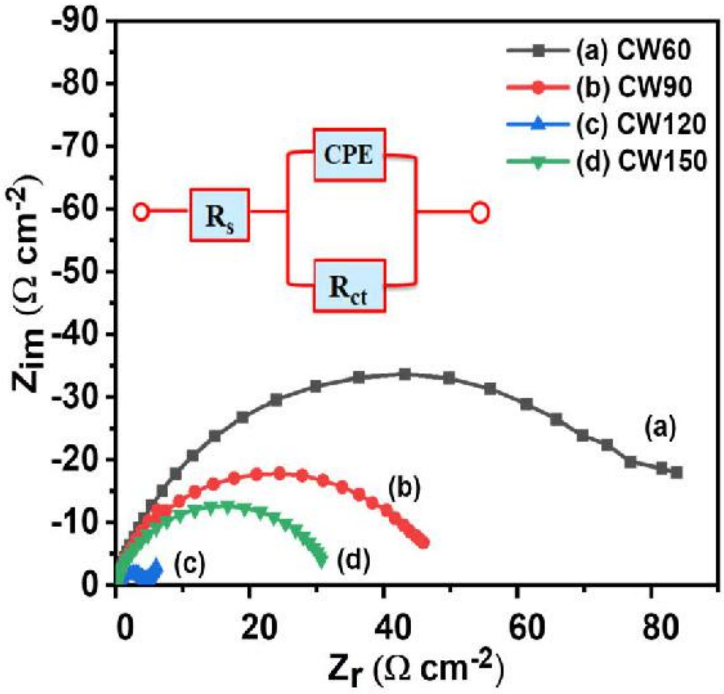

Figure 3.16: Nyquist plots (obtained from EIS) of $CoWO_4$ electrode prepared at different deposition cycles.

Table 3.2: Electrochemical impedance spectroscopic fitted circuit parameters for Nyquist plots of $CoWO_4$ thin film electrodes.

Parameters	Electrocatalysts			
	CW60	CW90	CW120	CW150
R_s (Ω cm^{-2})	0.69	0.65	0.67	0.70
R_{ct} (Ω cm^{-2})	44.98	48.71	55.90	83.80
CPE (F)	13.80	6.20	6.80	7.00

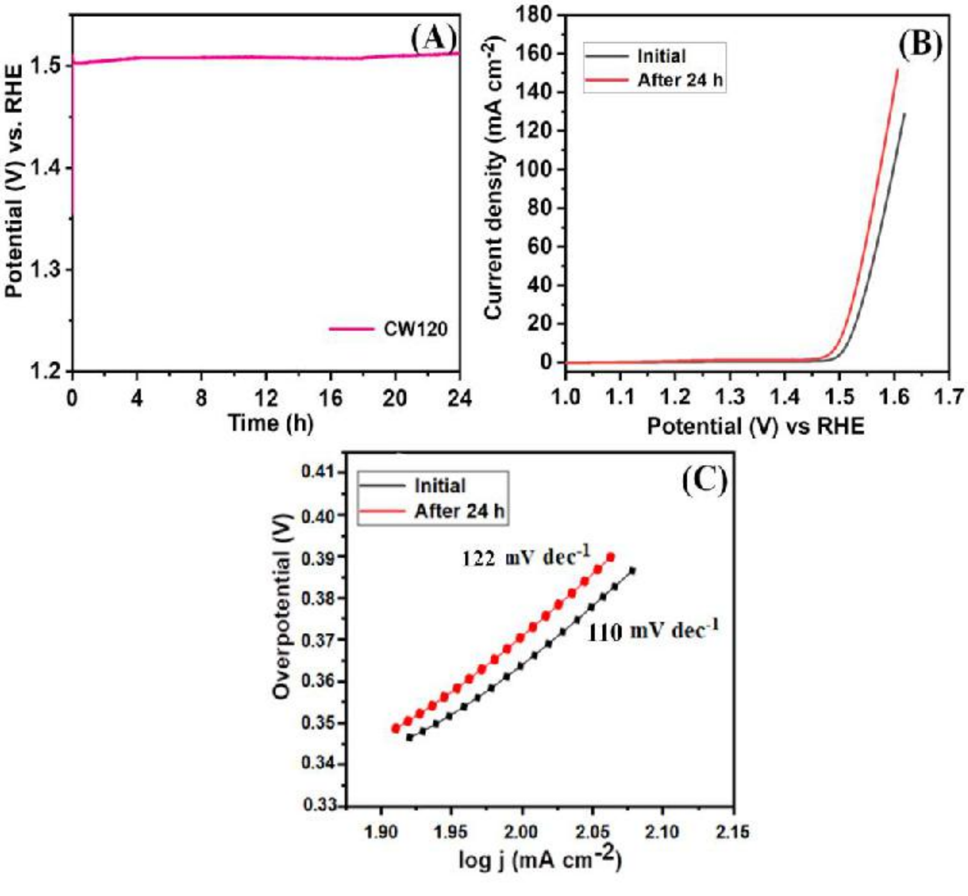

Figure 3.17: A) 24 h stability test of CW120 electrode at 10 mA cm^{-2}, B) The LSV curves measured before and after stability study, and C) Tafel plots extracted from LSV curves before and after stability study.

The stability of electrocatalyst is also an important criterion to assess the performance of the catalyst in practical applications. Herein, the electrochemical stability of CW120 electrocatalyst towards OER is measured by chronopotentiometry mode at a constant current density of 10 mA cm^{-2} for 13 h (Figure 3.17A). The

CW120 electrocatalyst displays a negligible change in the polarization curve after 24 h of continuous oxygen evolution, as shown in Figure 3.17B, indicating good stability towards the OER. Figure 3.17C shows Tafel slope of CW120 electrocatalyst, extracted from LSV graphs, before and after stability test. The value of Tafel slope increased from 110 to 122 mV dec^{-1}. This may be due to the blocking of some catalytically active sites during the long term OER.

3.3. Conclusions:

In conclusion, SILAR method is developed to prepare nanocrystaline $CoWO_4$ film electrodes directly on SS substrate. The mass loading of $CoWO_4$ as thin film electrodes is significantly changed with the number of deposition cycles which influenced the surface morphology. CW120 showed maximum C_s of 590 F g^{-1} at the scan rate of 100 mV s^{-1} in 1 M KOH electrolyte. The surface texture of thin film was like nanospheres, possessing a specific surface area of 49.3 cm^2 g^{-1} and an average pore radius of 12.68 nm. The mesoporous surface showed a hydrophilic nature. Lower resistive parameters such as R_s (0.88 Ω cm^{-2}) and R_{ct} (4.5 Ω cm^{-2}) as well as capacitive retention of 88 % after 3000 GCD cycles of CW120 thin film electrode are ascribed to its nanostructured morphology consisting of nanospheres that provides easy access for electrolyte ions. The present strategy provides a new opportunity for promoting further development of *SCs* by enhancing the involvement of the nanocrystalline and mesoporous materials. As an impact of change in morphology and mass loading, CW20 (deposited at 120 SILAR cycles) thin film electrode exhibited an efficient electrocatalytic OER performance with 320 mV overpotential at 10 mA cm^{-2} and Tafel slope 110 mV dec^{-1}. The rough, porous surface and binder free synthesis are the main reasons for high ECSA (47 F cm^{-2}) and low R_{ct} values (4.5 Ω) which enhance OER performance of CW120 thin film electrode. Also, this study gives the importance of optimization of mass loading of catalyst material on the substrate. As the SILAR method is useful for large scale deposition, it can be scaled up for the large scale production of $CoWO_4$ films.

3.4 References:

[1] Y. Jiang and J. Liu, Energy Environ. Mater., 2 (2019) 30-37.

[2] X. Xing, Y. Gui, G. Zhang, C. Song, Electrochim. Acta, 157 (2015) 15-22.

[3] C. Qiu, L. Ai, J. Jiang, ACS Sustain. Chem. Eng., 6 (2018) 4492-4498.

[4] G. Gund, D. Dubal, B. Patil, S. Shinde, C. Lokhande, Electrochim. Acta., 92 (2013) 205-215.

[5] C. Ling, L.Q. Zhou, H. Jia, RSC Adv., 4 (2014) 24692-24697.

[6] M. Zhang, H. Fan, N. Zhao, H. Peng, X. Ren, W. Wang, H. Li, G. Chen, Y. Zhu, X. Jiang, P. Wu, Chem. Eng. J., 347 (2018) 291-300.

[7] F. Li, H. Na, W. Jin, X. Xu, W. Wang, and J. Gao, J. Solid State Electrochem., 22 (2018) 2767-2774.

[8] V. Lokhande, T. Ji, Adv. Sc. Technol. Lett., 139 (2016) 409-413.

[9] S. Chen, G. Yang, Y. Jia, H. Zheng, Chem. Electrochem., 3 (2016) 1490-1496.

[10] K. Ding, X. Zhang, J. Li, P. Yang, X. Cheng, Chem. Electro. Chem., 4 (2017) 3011-3017.

[11] G. Karkera, T. Sarkar, M. Bharadwaj, A. Prakash, ChemCatChem, 9 (2017) 3681-3690.

[12] F. Luo, R. Xu, S. Ma, Q. Zhang, H. Hu, K. Qu, S. Xi, Z. Yang, W. Cai, Appl. Catal. B, 259 (2018) 118090-118095.

[13] B. Rani, G. Ravi, S. Ravichandran, V. Ganesh, F. Ameen, A. Al-sabri, R. Yuvakumar, Appli. Nanosci., 8 (2018) 1241-1258.

[14] H. Pathan, C. Lokhande, Bull. Mater. Sci., 27 (2004) 85-111.

[15] A. Patil, G. Lohar, V. Fulari, J. Mater. Sci., 27 (2016) 9550-9557.

[16] F. Lei, B. Yan, H. Chen, J. Zhao, J. Am. Ceram. Soc., 92 (2009) 1262-1267.

[17] J. Zhang, Y. Zhang, J. Yan, S. Li, H. Wang, F. Huang, Y. Shen, A. Xie, J. Nanopart. Res., 14 (2012) 796-805.

[18] Q. Zhang, W. Yao, X. Chen, L. Zhu, Y. Fu, G. Zhang, L. Sheng, S. Yu, Cryst. Growth Des., 7 (2007) 1423-1431.

[19] P. Sharma, M. Minakshi, J. Whale, A. Jean-Fulcrand, G. Garnweitner, Nanomaterials, 11 (2021) 580-596.

[20] P. Bagwade, D. Malavekar, S. Ubale, R. Bulakhe, I. In, U. Patil, C. Lokhande, 408 (2022) 139933-139944.

[21] X. Xing, Y. Gui, G. Zhang, C. Song, Electrochim. Acta, 157 (2015) 15-22.

[22] A. Bhardwaj, I. Kim, L. Mathur, J. Park, S. Song, J. Hazard. Mater., 403 (2021) 123797-123808.

[23] P. Bagwade, D. Malavekar, T. Ghogare, S. Ubale, V. Mane, R. Bulakhe, I. In, C. Lokhande, J. Alloys Compd., 859 (2021) 157829-157848.

[24] D. Dubal, D. Dhawale, R. Salunkhe, V. Fulari, C. Lokhande, Electrochim. Acta, 497 (2010) 166-170.

[25] S. Ubale, S. Kale, V. Mane, P. Bagwade, C. Lokhande, J. Solid State Electrochem., 25 (2021) 1753-1764.

[26] M. Zhang, H. Fan, N. Zhao, H. Peng, X. Ren, W. Wang, H. Li, G. Chen, Y. Zhu, X. Jiang, P. Wu, Chem. Eng. J., 347 (2018) 291-300.

[27] P. Taneja, S. Sharma, A. Umar, S. Mehta, A. Ibhadon, S. Kansal, Mater. Chem. Phys., 211 (2018) 335-342.

[28] P. Shinde, N. Chodankar, V. Lokhande, A. Patil, T. Ji, J. kim, C. Lokhande, RSC Adv., 114 (2016) 113442-113451.

[29] S. Alshehri, J. Ahmed, T. Ahamada, P. Arunachalama, T. Ahmad, A. Khan, RSC Adv., 7 (2017) 45615-45623.

[30] A. Saleh, N. Ahmed, A. Biby, N. Allam, J. Colloid Interface Sci., 603 (2021) 478-490.

[31] B. Huang, H. Wang, S. Liang, H. Qin, Y. Li, Z. Luo, C. Zhao, L. Xie, L. Chen, Energy Storage Mater., 32 (2020) 105-114.

[32] P. Xu, K. Ye, D. Cao, J. Huang, T. Liu, K. Cheng, J. Yin, G. Wang, J. Power Sources, 268 (2014) 204-211.

[33] G. Ojha, B. Pant, A. Muthurasu, S. Chae, S. Park, T. Kim, H. Kim, Energy, 188 (2019) 116066-116078.

[34] S. Kale, A. Lokhande, R. Pujari, C. Lokhande, J. Colloid Interface Sci., 532 (2018) 491-499.

CHAPTER-4

$CoWO_4$@rGO thin films by SILAR method; characterizations, electrochemical and electrocatalytic performance

CHAPTER 4

$CoWO_4$@rGO thin films by SILAR method; characterizations, electrochemical and electrocatalytic performance

SECTION- A

Synthesis and characterization of $CoWO_4$@rGO composite thin film electrode

SECTION - B

Electrochemical Supercapacitive performance of $CoWO_4$@rGO composite thin film electrode

SECTION - C

Electrocatalytic OER performance of $CoWO_4$@rGO composite thin film electrode

4.1. Introduction:

The composition of pseudocapacitive materials with modified graphenes (rGO and GO) has been widely studied due to their exceptional characteristics, particularly high surface area, moderate electrical conductivity, and good thermal stability [1]. Different morphologies can be achieved by employing composition. Also, the composition of pseudocapacitive materials with EDLC materials shows an effective way to enhance electrochemical cycling stability. The functional groups attached to the rGO such as -COOH, -OH, -CHO, etc., provide excellent defect sites for the growth of pseudocapacitive material [2]. However, the binder free synthesis of the composite electrode on the conducting current collector is still a challenge [3].

SILAR is a facile and low cost thin film deposition method used to synthesize variety of nanostructures via governing parameters like temperature, time, and precursor concentration. Therefore this method is effective in preparing composite materials for various application. In this investigation, cobalt tungstate/reduced graphene oxide ($CoWO_4$@rGO) composite materials were synthesized using SILAR method. This method replaces the conventional drop casting method where, the synthesized composite materials are in powder form and they are deposited on SS substrates which create dead volume caused by tedious process of mixing active material without binders [4].

In the present work, effect of change in concentration of rGO on physico-chemical properties, and their effect on the supercapacitive as well as electrochemical water splitting in terms of OER are studied. Meanwhile, pristine $CoWO_4$ 120 (CW120) and $CoWO_4$@rGO composite ($CoWO_4$@rGO) at different concentrations of rGO (0.05, 0.10, 0.15, 0.20, and 0.25 mg mL^{-1} concentration) are synthesized and compared their electrochemical study to investigate the best performing electrocatalyst. Present investigation gives the detailed study of $CoWO_4$@rGO composite materials and their physico-chemical characterizations. Further, analysis of thin film deposited electrodes were done for the supercapacitive and electrochemical splitting of water in the forms of OER properties were studied.

SECTION - A

Synthesis and characterization of $CoWO_4$@rGO composite thin film electrode

4.2.A.1 Experimental details:

4.2.A.1.1 Materials used and substrate cleaning:

To prepare rGO, analytical grade sulfuric acid (H_2SO_4), sodium nitrate ($NaNO_3$), graphite flakes, potassium permanganate ($KMnO_4$), hydrochloric acid (HCl) and hydrogen peroxide (H_2O_2), etc. chemicals were required. For the synthesis of $CoWO_4$@rGO, cobalt chloride ($CoCl_2.6H_2O$) and sodium tungstate ($NaWO_4.2H_2O$) were, purchased from Thomas Baker. The SS substrates were cleaned by acetone and DDW.

4.2.A.1.2 Synthesis of reduced graphene oxide (rGO):

The Hummers method was used to synthesize GO [5]. First of all, $NaNO_3$ (2.5 g) and graphite flakes (5 g) were mixed in H_2SO_4 in 1 L Beaker (120 mL) and stirred for 30 min at room temperature. After 30 min, the reaction bath was kept in ice to maintain the reaction temperature bellow 5°C. After that, $KMnO_4$ (15 gm) was slowly added to the reaction bath [rate:~1g/6min].

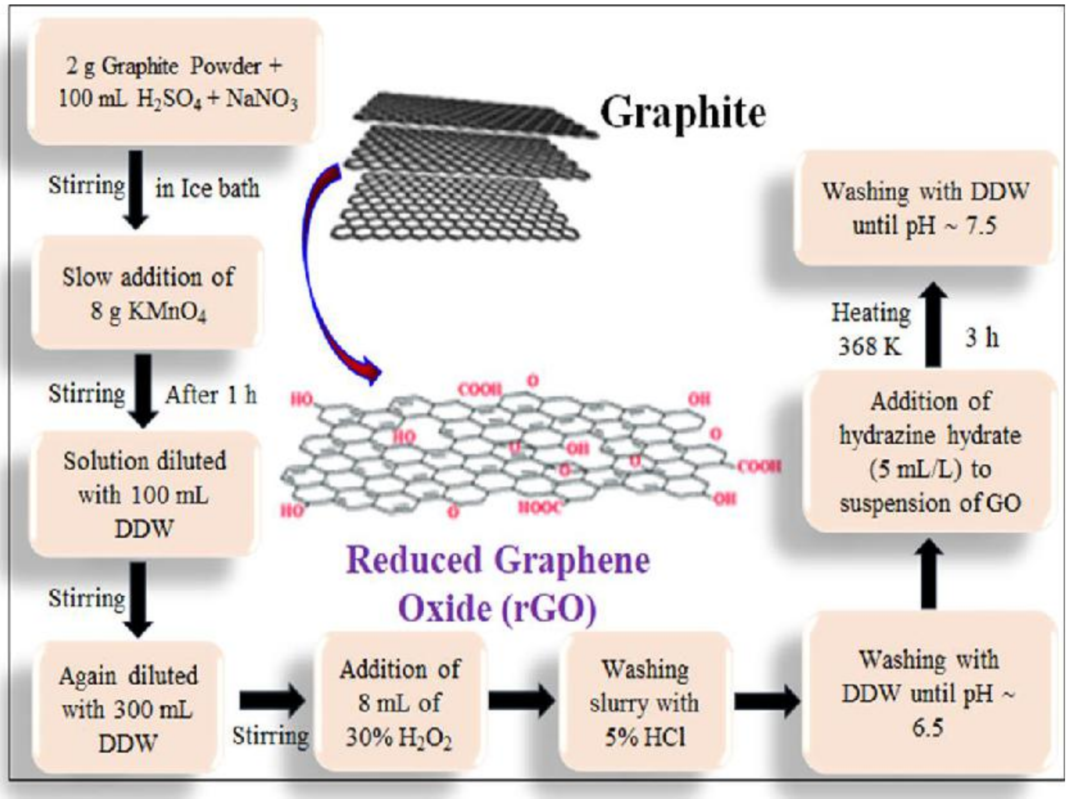

Figure 4.1: Schematic flow chart of rGO synthesis.

After completion of addition, the prepared mixture was stirred for 6 h at room temperature. After 12 h, the colour of solution was changed from black to dark reddish. Later, DDW (50 mL) was added and reaction temperature was increased to 95 °C for 30 min (color changes to brown). The 50 mL mixture of 30 % H_2O_2 and 150 mL DDW was slowly added while maintaining temperature of solution at room temperature. During the addition of H_2O_2, the color of solution turns dark brown to yellow. Furthermore, 100 mL solution containing 25 mL HCl and 75 mL DDW was added in the mixture for washing purpose (color changes to blackish brown). Then, resultant mixture was centrifuged at low rpm (2000) to remove unreacted graphite flakes and further centrifuged at high rpm (10000) several times to wash GO nanosheets until pH becomes ~5, to obtain brown colored GO solution. From hydrazine hydrate process we convert GO solution to rGO. The whole process of synthesis of the rGO is schematically represented in Figure 4.1. The schematic of SILAR method for prepration of $CoWO_4$@rGO thin film preparation is shown in Figure 4.2.

4.2.A.1.3 Synthesis of $CoWO_4$@rGO:

The concentration of rGO suspension was calculated by drying 1 mL of rGO solution at temperature of 373 K and then measuring its weight. From the determined concentration, dispersions of rGO with concentration of 0.05, 0.10, 0.15, 0.20, and 0.25 mg mL^{-1} were prepared in DDW. The rGO sheets were deposited on SS substrate using layer by layer method followed by single deposition cycle of $CoWO_4$ nanoparticles using the SILAR method. Where, the SS substrate was dipped in rGO solution for 60 s for adsorption of rGO sheets, followed by insertion in cationic solution for 20 s, to adsorb Co^{2+} ions. In this process, some Co^{2+} species may react with extraplanar hydroxyl or carboxyl groups of rGO sheets.

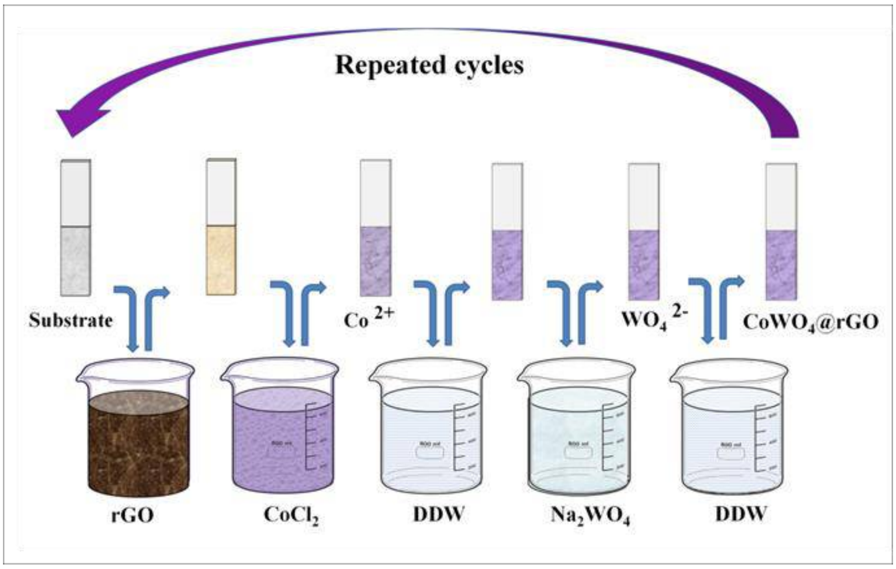

Figure 4.2: The schematic of SILAR method for prepration of $CoWO_4$@rGO thin film on SS substrate.

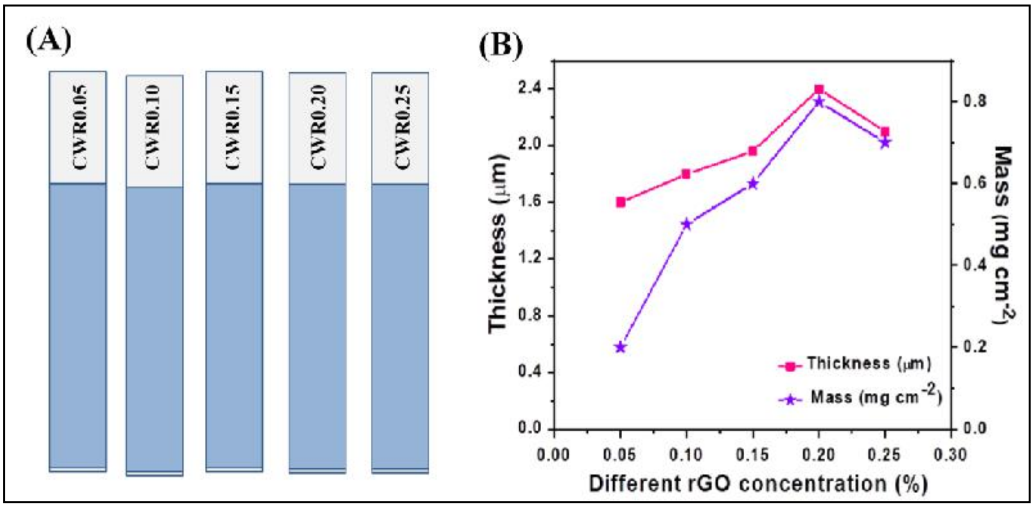

Figure 4.3: A) Photograph of $CoWO_4$@rGO composite deposited using SILAR method, and B) The variation of $CoWO_4$@rGO composite series thickness and mass of electrodes with the different concentrations of rGO deposited on SS substrate.

To remove loosely bound Co^{2+} ions, SS substrate was rinsed in DDW for 25 s subsequently, and dipped in the anionic precursor (WO_4^{2-}) for 20 s for reaction and again rinsed in DDW for 30 s. In this way, a cycle of $CoWO_4$@rGO deposition was completed and 100 such cycles were repeated with different concentrations of rGO suspension. The process of deposition was carried out using an automated SILAR coating system (HOLMARC-HO-TH-03A). Thin film growth becomes uniform as both rGO sheets and $CoWO_4$ have hexagonal structure. The synthesized $CoWO_4$@rGO composite thin films prepared with 0.05, 0.10, 0.15, 0.20, and 0.25 mg mL^{-1} concentrations of rGO suspension are denoted as CWR0.05, CWR0.10, CWR0.15, CWR0.20 and CWR0.25, respectively. The photograph of $CoWO_4$@rGO composites is shown in Figure 4.3A, the graph of thickness and mass loading of $CoWO_4$@rGO composites is illustrated in Figure. 4.3B.

4.2.A.2 Results and discussion:

4.2.A.2.1 Material Characterization:

4.2.A.2.1.1 XRD analysis:

The XRD patterns of CW120, CWR0.05, CWR0.10, CWR0.15, CWR0.20, and CWR0.25 thin films are shown in Figure 4.4A. Intense peaks correspond to (100), (011), (-111), (002), (-102), (202), (-113), and (-311) planes of hexagonal crystal structure of $CoWO_4$ (JCPDS card no. 01-078-0877) [6]. The variation in the peak intensity at (-111) indicates that the concentration of rGO affects the growth rate of $CoWO_4$ nanoparticles on rGO sheet. The calculated 'd' values (from Eq. 2.2) match well with standard ‘d’ values which confirm the hexagonal crystal structure of $CoWO_4$ in $CoWO_4$@rGO thin films. The prominent diffraction peaks observed for $CoWO_4$@rGO thin films are different from that of $CoWO_4$ thin films. The crystallite size calculated using Scherrer’s formula (Eq. 2.2) along (-111) plane is 0.35 nm. Compared to the crystallite size of $CoWO_4$, crystallite size of $CoWO_4$@rGO is higher. The XRD peaks highlighted by the symbol * correspond to the SS substrate. No other diffraction peak is observed indicating the absence of any other impurity. The XRD study confirms that the composition of rGO with $CoWO_4$ affects growth of $CoWO_4$ particles.

4.2.A.2.1.2 FTIR analysis:

The FT-IR spectra in the wavenumber range of 4000–400 cm^{-1} for CW120, CWR0.05, to CWR0.25 thin films are shown in Figure 4.4B. The deformation mode of W-O bonds in WO_4 is observed at 428 cm^{-1}. The Co-O stretching mode is observed at 616 cm^{-1}. A sharp peaks at around 817 cm^{-1} assigned to the characteristic absorption of $CoWO_4$. The peak at 1370 cm^{-1} corresponds to -COOH symmetric stretch [7, 8]. The broad peak at 1625 cm^{-1} indicates the presence of sp^2 bond of C-C in rGO. The peaks at 2258, 2666 and 2916 show stretching vibration mode. Also, peak at 3281 cm^{-1} is associated with bonded and nonbonded -OH groups from adsorbed water molecules. Compared to FT-IR spectrum of $CoWO_4$ thin films, additional absorption bands from the rGO is observed in the $CoWO_4$@rGO thin films [9]. From the results, the formaion of $CoWO_4$@rGO on SS substrate was confirmed.

4.2.A.2.1.3 Raman analysis:

The Raman spectra of $CoWO_4$ and CWR series are shown in Figure. 4.4C. The G bands at ~1608 cm^{-1} are characteristic of sp^2 hybridized carbon-carbon bonds in graphene while the D bands at ~1346 cm^{-1} are characteristic of lattice distortions and sp^3-like defects caused by the oxidation process. In the case of $CoWO_4$, Co-O bonds have the same bond length and W-O bonds have an asymmetric nature. The distorted crystal structure forms due to asymmetric bonds. Therefore, the Raman spectrum of tungstate enclosing molecules is influenced by tungstate octahedron peaks [10]. All peaks correspond exactly to the characteristic monoclinic CoWO4 active mode reported in the literature. The main peak at 880 cm^{-1} corresponds to symmetrical stretching vibration of terminal W=O bond. The peak of 767 and 680 cm^{-1} reaches to the asymmetric stretching of O–W–O vibration mode bridges. The weak peaks observed at 405 and 340 cm^{-1} meet to deformation and rotation indicate bridging W–O bonds. The stretching vibration of Co–O bond observed at 280 cm^{-1} [11]. The lowest wavelength peaks seen at 195 and 132 cm^{-1} is related to the off-plane vibration. Therefore, the formation of $CoWO_4$ nanostructures is supported by Raman spectra studies. In the spectra of $CoWO_4$@rGO nanocomposites, the characteristic peaks of $CoWO_4$ and rGO still exist, indicating the successful synthesis of their composites.

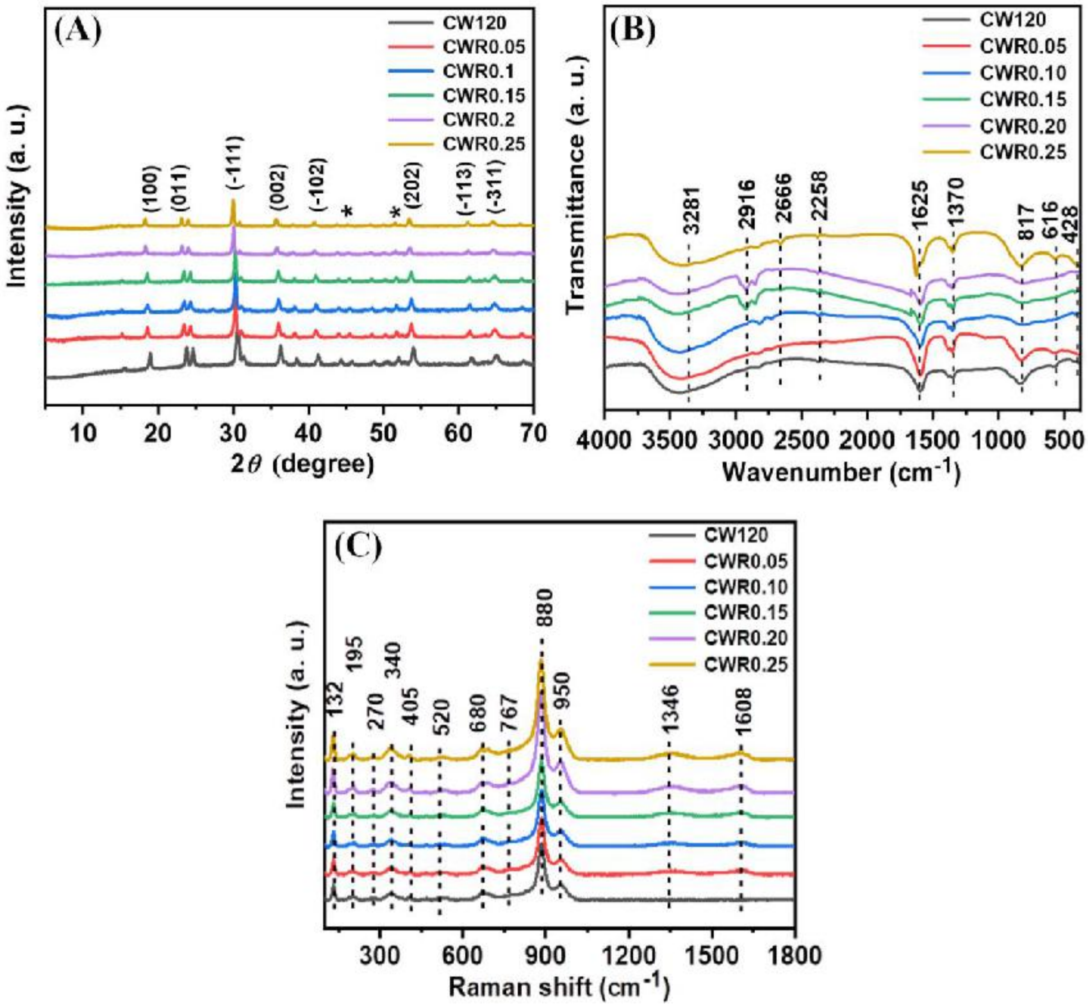

Figure 4.4: A) XRD patterns, B) FT-IR patterns, and C) Raman spectra of CWR thin films deposited using different concentrations of rGO suspension.

4.2.A.2.1.4 Field emission scanning electron microscopy:

Microstructures of $CoWO_4$@rGO thin films investigated from FE-SEM analysis, the microstructure at different magnifications are shown in Figure 4.5 (A-L). Figure 4.5 (A-B) indicates microstructure of CW120 thin film exhibits spherical-like nanoparticles. Figure 4.5 (C-D) shows morphology of the CWR0.05 thin film at 10,000X and 25,000X magnifications, displaying a discontinuous and irregularly arranged rGO sheets structure. As increase in concentration of rGO discontinuous and irregularly arranged rGO sheets are observed from Figure 4.5 (C-L). The FE-SEM images at 10,000X magnification indicate rGO network is interconnected by $CoWO_4$ nanoparticles and the nanoparticles are sandwiched between rGO sheets.

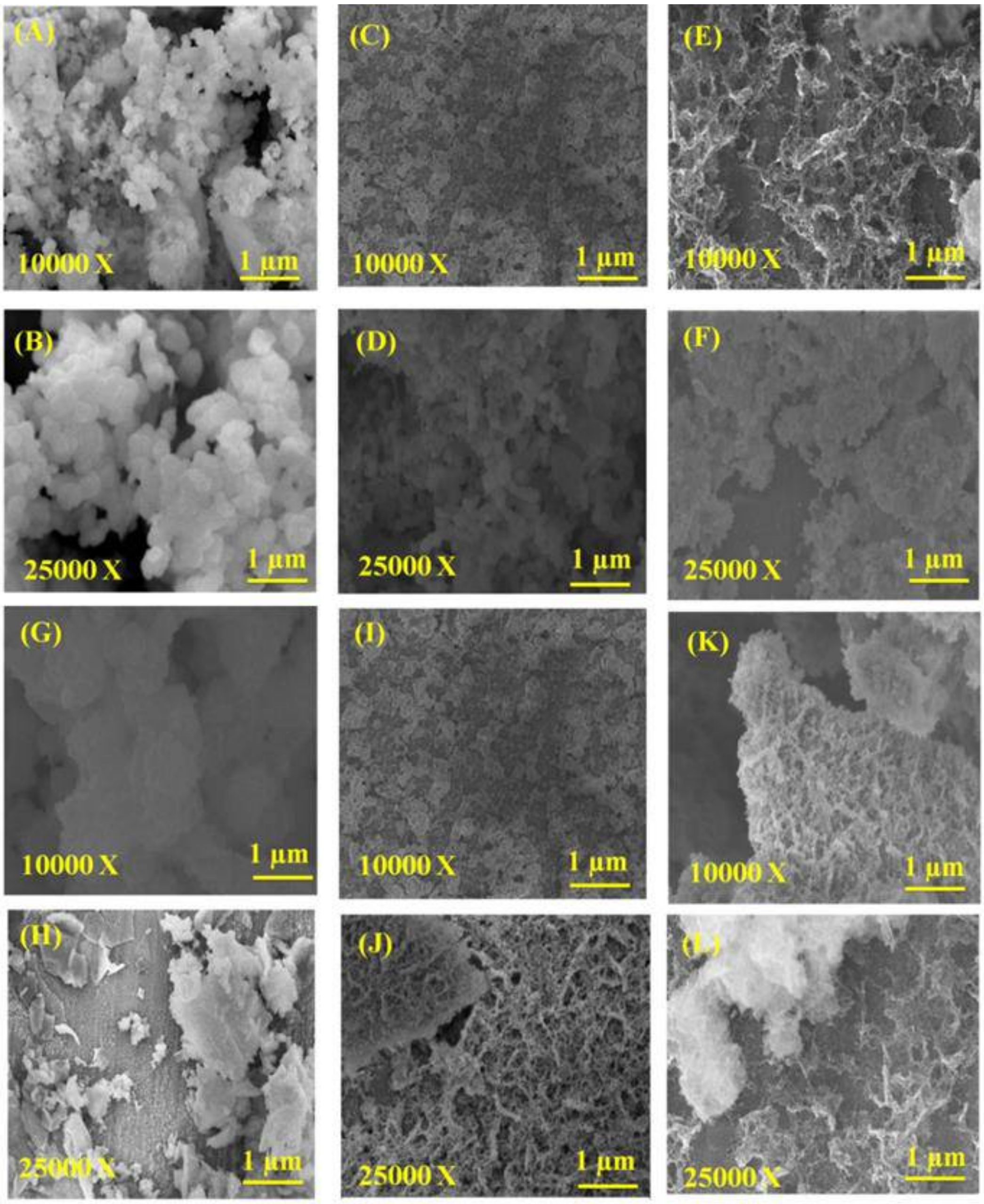

Figure 4.5: FE-SEM images of A-B) CW120, C-D) CWR0.05, E-F) CWR0.10, G-H) CWR0.15, I-J) CWR0.20, and K-L) CWR0.25 at the magnification of 10,000X, and 25,000X.

The rGO sheets are uniformly coated with $CoWO_4$ nanoparticles in all thin films prepared at various concentrations of rGO suspension. These nanoparticles prevent the stacking of rGO sheets and provide easy access to electrolyte ions at the bulk of electrode material through diffusion [12-14]. Compared to FE-SEM images of

$CoWO_4$ thin films (Figure 3.4), the pores are observed on topography of $CoWO_4$@rGO thin films. These pores are beneficial for the diffusion of electrolytic ions.

4.2.A.2.1.5 EDAX study:

The EDAX plays an important role to find out composition in the thin film material. The chemical composition of $CoWO_4$@rGO thin films deposited using different concentrations of rGO suspension was investigated by the EDAX. The EDAX spectra of $CoWO_4$@rGO thin films are shown in Figure 4.6A-D. The atomic percentages of C, O, Co, and W elements are shown in the inset of each spectrum, which confirm the composite nature of the thin films.

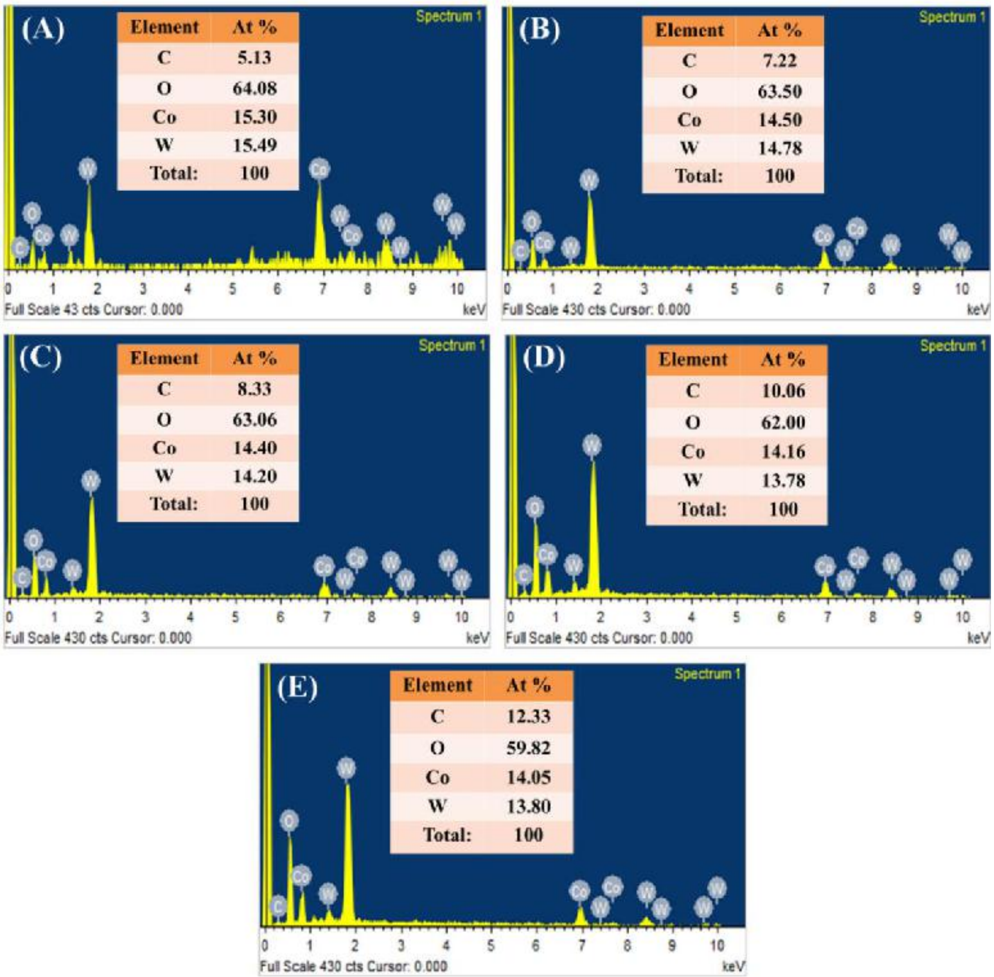

Figure 4.6: The EDAX spectra of A) CWR0.05, B) CWR0.10, C) CWR0.15, D) CWR0.20 and E) CWR0.25 thin films (Insets show atomic percentages of constituting elements).

The approximately similar atomic percentage of Co, W and O indicates the possible formation of CoWO4 on rGO sheets. Slightly higher content of oxygen shows effective oxidation of the graphite flakes into rGO sheets. The rGO sheets have nonplaner oxygen containing groups which allow the growth of CoWO4 nanoparticles, and also, these groups provide more active sites for interaction with K+ ions from electrolyte, which may increase the energy storage capacity of a composite thin film [15].

4.2.A.2.1.6 Surface Wettability:

The contact angle measurement was carried out in order to study the interfacial properties between water and electrode. The hydrophilic or hydrophobic nature of material can be confirmed by contact angle [54]. The water contact angle photographs of A) CW120, B) CWR0.05, C) CWR0.10, D) CWR0.15, E) CWR0.20, and F) CWR0.25 composite films presented in Figure 4.7 show contact angles of 61°,

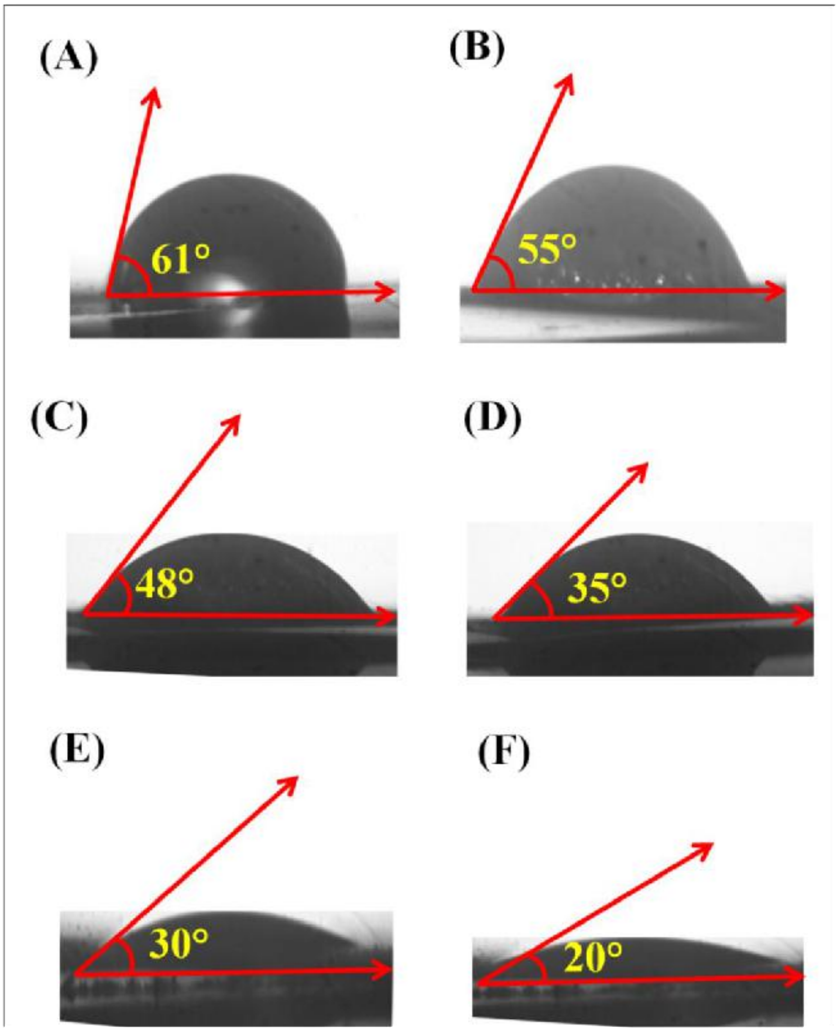

Figure 4.7: Contact angle photographs of A) CW120, B) CWR0.05, C) CWR0.10, D) CWR0.15, E) CWR0.20, and (F) CWR0.25 thin films.

55°, 48°, 35°, 30°, and 20°, respectively. The enhanced hydrophilicity of CWR composite series decreases the contact angle of composites as compared to pristine CW120 films making CWR composite film more favorable for supercapacitor application in water based electrolytes [16]. For supercapacitive and electrocatalytic applications, hydrophilic surfaces are useful for making intimate contact with water based electrolytes. It is acknowledged that the hydrophilic surface of the electrode is an essential element in an electrochemical supercapacitor for good performance [17].

4.2.A.2.1.7 BET analysis:

The high specific surface area of the material enhances the rate of reactions owing to increased number of reaction sites on materials surface [18]. The specific surface area of CWR0.20 nanoparticles along with pore size distribution was examined at 77 K using BET and FBJH techniques, respectively. The N_2 adsorption isotherm of CWR0.20 in the relative pressure between 0 to 1.0 are shown in Figure 4.7. The nature of isotherm (type IV) suggests the presence of mesopores structure of CWR0.20. The specific surface area of CWR0.20 is 65 m^2 g^{-1} which signifies the applicability of SILAR method for the preparation of CWR0.20 electrode material with high surface area.

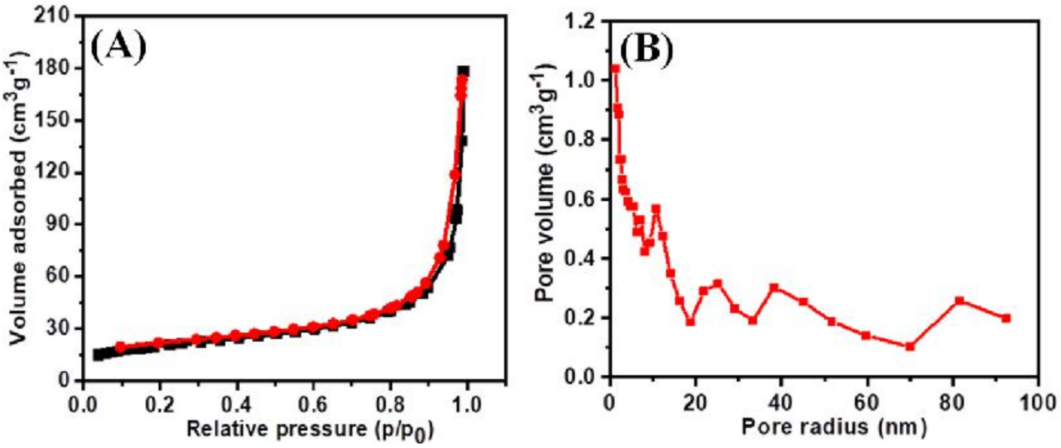

Figure 4.8: A) Nitrogen adsorption – desorption isotherms, and B) pore size distribution curve of CWR0.20 thin film.

The pore size distribution curve of CWR0.20 is shown in inset of Figure 4.8. Room temperature synthesis and precise control over reaction in the SILAR method enable preparation of microporous material. Lower average pore size and higher specific surface area are beneficial for electrochemical reactions which provide more electroactive sites [16].

4.2.A.2.1.8 XPS analysis:

The surface composition and the chemical states of $CoWO_4$@rGO are investigated by XPS. The XPS survey spectrum of $CoWO_4$@rGO is shown in Figure 4.9A, the survey spectrum confirms Co, O, C and W elements are present in the sample. In the high resolution of cobalt (Figure 4.9B), there are two major peaks at 781.2 eV and 797.5 eV along with two satellite peaks at 786.1 eV and 803 eV corresponding to $Co2p_{3/2}$ and $Co2p_{1/2}$, respectively. The peak positions revealed and confirmed that, the detected Co element have Co^{2+} electronic state [19]. The observed broad peak of oxygen is at 531.3 eV, which is deconvoluted into three peaks as 530.1, 531.13, and 531.5 eVs, where the peaks at 530.1 and 531.13 eVs corresponding to the M-O and P-O bonding and peak at 531.5 eV are due to surface adsorbed water (Figure 4.9C) [20].

High resolution C1s peaks in the XPS proves that oxygen-containing groups have been less due to reduction of GO at high temperature in hydrothermal process [20]. The intense peak shown in Figure 4.9D at 284.7 eV is due to C=C in-plane bonding of sp^2 hybridization. On the other hand, out of plane bonding of sp^3 hybridized C-C is very short. The present result provides the explicit indication regarding reduction of GO. The carboxylate carbon (O-C=O) is observed at 289.5 eV21]. The XPS spectrum of W4f has four peaks assigned to W^{6+} and W^{5+} (Figure 4.9E). The peaks at binding energy (B.E.) of 37.43 eV and 35.28 eV originated from $W4f_{5/2}$ and $W4f_{7/2}$ states of W^{6+}. The B. E. values of tungsten approve tungsten designation in a hexavalent state. The separation of spin-orbit of 2.15 eV shows great ordering as W among +6 valance in the compound [22, 23].

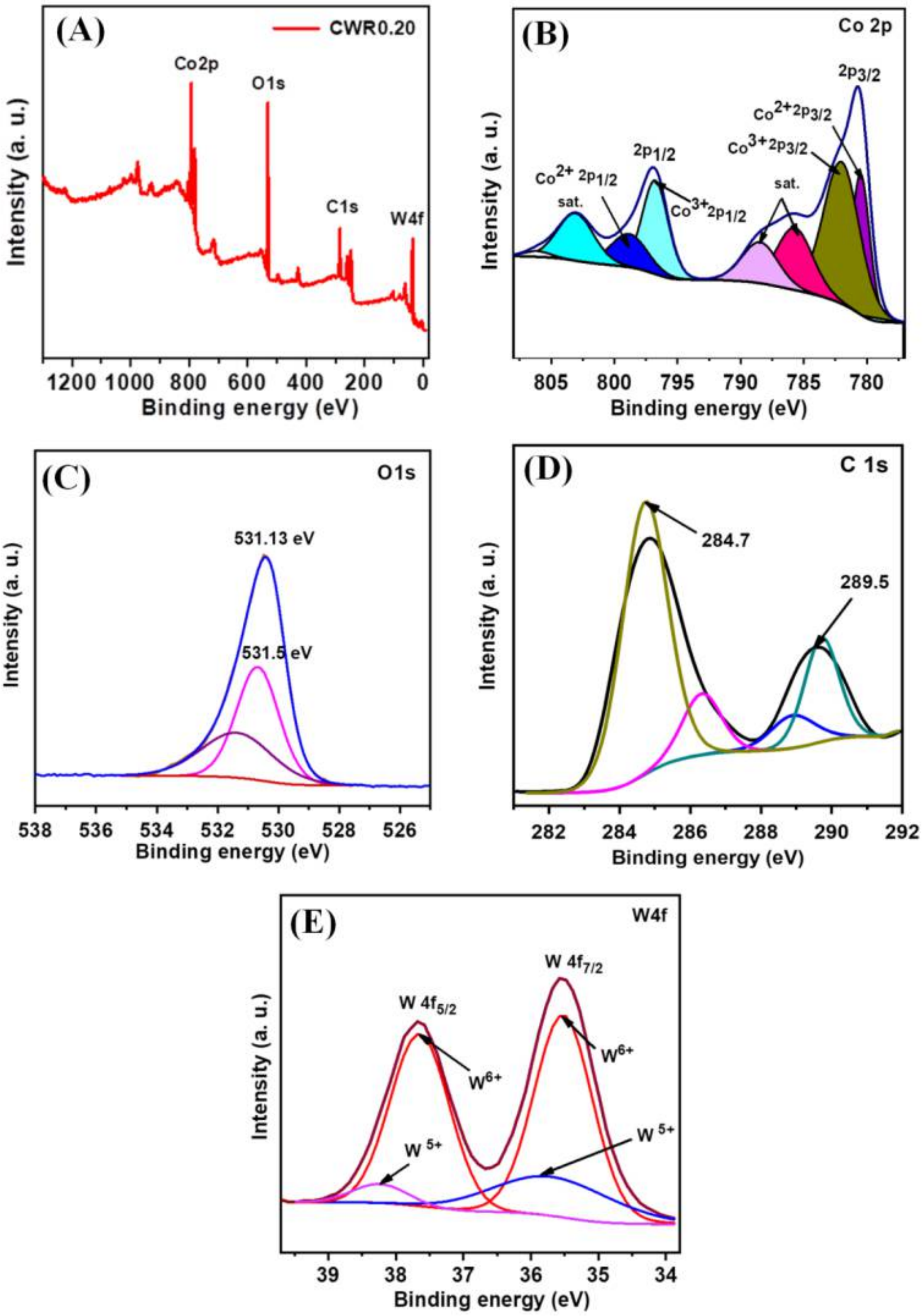

Figure 4.9: The XPS spectra of CWR0.20 electrode: A) survey spectrum, B) Co2p spectrum, C) C1s spectrum, D) O1s spectrum, and E) W4f spectrum.

SECTION B

Electrochemical Supercapacitive performance of CoWO$_4$@rGO composite thin film electrode

4.2.B.1 Electrochemical characterizations of CoWO$_4$@rGO thin films:

4.2.B.1.1 CV study:

To find out the effect of the composition of $CoWO_4$ with rGO on the electrochemical charge storage performance of electrodes, CV curves of $CoWO_4$ and $CoWO_4$@rGO composites were measured in a 1 M KOH electrolyte using a half cell (three electrodes) system with potential window 0.0 to 0.65 V/SCE. As shown in Figure 4.10A, there is a higher current response for the CWR0.20 thin film compared with CWR0.05, CWR0.10, CWR0.15, CWR0.20 and CWR0.25 thin film electrodes. The area enclosed by the CV curve of rGO was too smaller compared to $CoWO_4$@rGO electrodes. The specific capacitance of rGO (90 F g^{-1}) is very low compared to CWR0.20 (1201.8 F g^{-1}) at the scan rate of 5 mV s^{-1}.

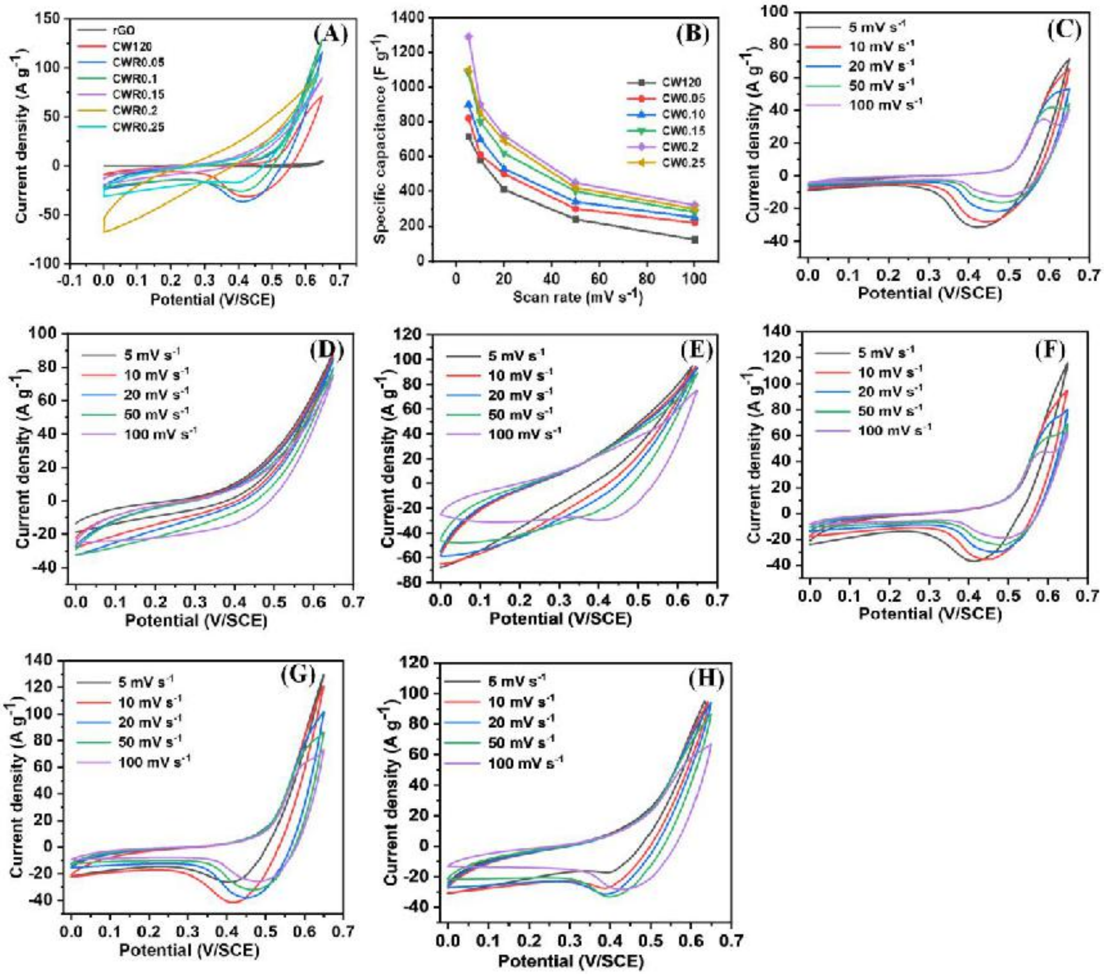

Figure 4.10 A) Comparative CV curves of rGO and $CoWO_4$@rGO thin films at a scan rate of 5 mV s^{-1}, B) variation of C_s with the scan rate, and the CV curves at various scan rates from 5-100 mV s^{-1} of C) CWR120, D) CWR0.05, E) CWR0.10, F) CWR0.15, G) CWR0.20, and H) CWR0.25 thin film electrodes.

Hence, further electrochemical characterization of rGO does not reported in further study. This shows that CWR0.20 thin film electrode may facilitate fast electronic and ionic transport which raises the current response capacity of the electrode [24, 25].

The nonrectangular shape of the CV curves confirm the presence of a pseudocapacitive charge storage mechanism [26]. The C_s values of CW120, CWR0.05, CWR0.10, CWR0.15, CWR0.20 and CWR0.25 film electrodes are 714, 750, 901.6, 1109.1, 1201.8, and 1022.9 F g^{-1} a scan rate of 5 mV s^{-1} respectively. The graphs of variation of C_s with the scan rate for all films displayed in Figure 4.10B shows a decrease in C_s with a higher scan rate due to least time for reversible redox reactions to occur [27]. At a higher scan rate, all the electrolyte ions do not undergo reversible redox reaction due to time constraint so C_s decreases with the scan rate. The CV curves of CWR0.05, CWR0.10, CWR0.15, CWR0.20 and CWR0.25 thin film electrodes at different scan rates from 5 to 100 mV s^{-1} are shown in Figure 4.10C-H. From the CV curves one can conclude that $CoWO_4$ thin film electrodes can be used as an electrode material at various current ratings. As specific capacitance of $CoWO_4$@rGO composite electrode is larger than $CoWO_4$ electrode, further electrochemical properties of $CoWO_4$@rGO are studied [28].

4.2.B.1.2 GCD study:

The GCD curves of CW120 and $CoWO_4$@rGO composite variations are shown in Figures 4.11 A. The GCD curves show transformation of charge storage mechanism due to the composition of $CoWO_4$ with rGO [29]. The C_s value from GCD plot is 1300 F g^{-1} at the current density of 1 A g^{-1} for $CoWO_4$@rGO. Variation of C_s with the applied current density is shown in Figure 4.11 B. The values of C_s for CW120, CWR0.05, CWR0.10, CWR0.15, CWR0.20, and CWR0.25 composite electrode are 714, 820, 900, 1080, 1290, and 1100 F g^{-1}, respectively. The GCD study shows good reversibility of $CoWO_4$@rGO composite electrode. As C_s decreases with the increasing scan rate, in the same way, it decreases with the rising current density.

The GCD curves for different rGO concentrations of CWR0.05, CWR0.10, CWR0.15, CWR0.20, and CWR0.25 are shown in Figure 4.11 (C-H) with the changing current density from 1 to 4 A g^{-1}. From the CV and GCD studies, it is concluded that the charge storage for $CoWO_4$@rGO electrode is mainly attributed to surface faradaic charge transfers as a result of the insertion of electrolyte ions into layer structured $CoWO_4$@rGO electrode [30, 31]. The decrease in C_s with rising current density is because of limited time available for reversible redox reactions at higher values of changing current densities [32].

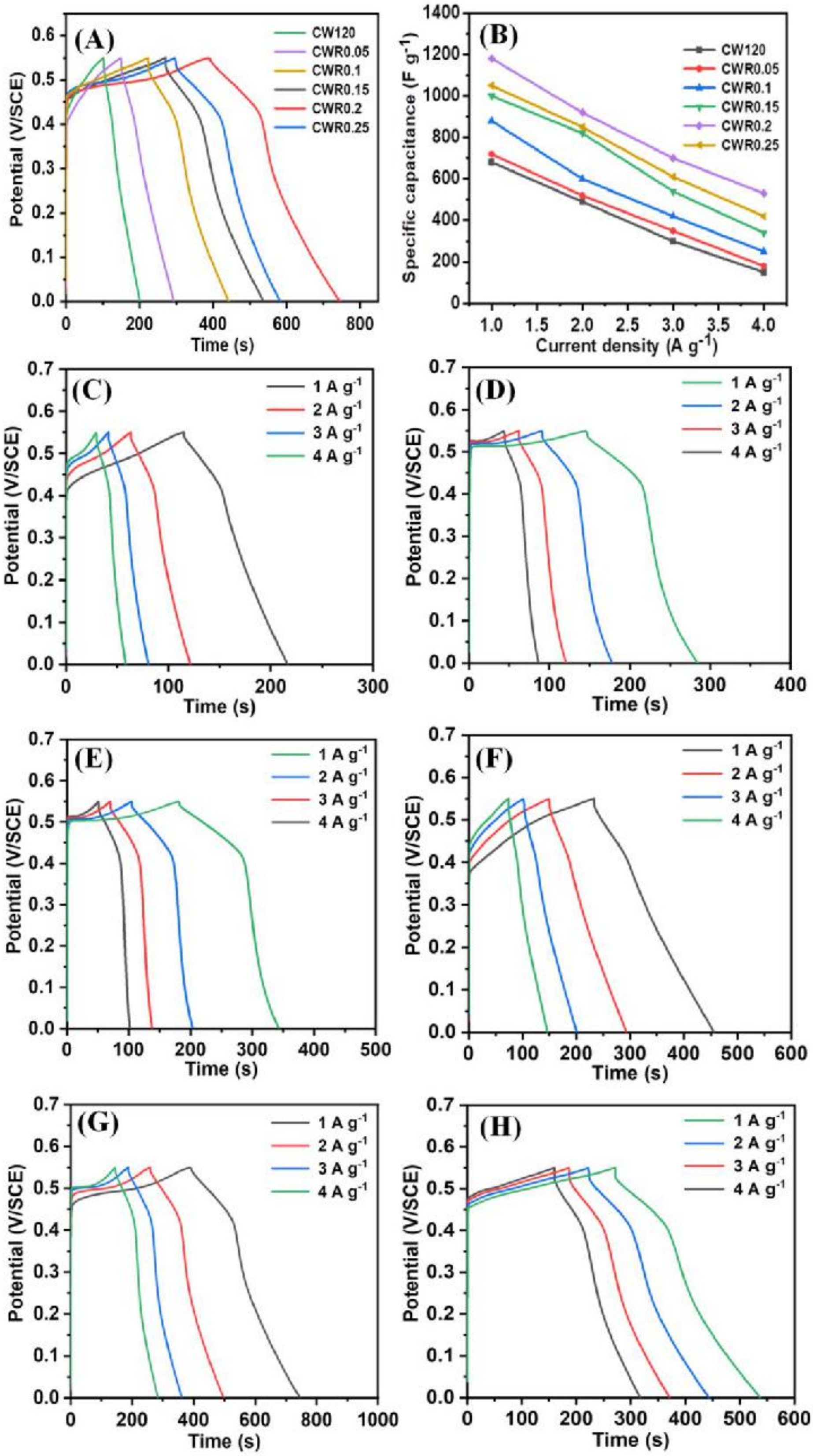

Figure 4.11: A) Comparative GCD curves of CoWO$_4$@rGO thin film electrodes at a current density of 3 A g^{-1}, B) variation of C_s with the current densities, and the GCD

curves at various current densities from 1-4 A g^{-1} of C) CW120, D) CWR0.05, E) CWR0.10, F) CWR0.15, G) CWR0.20, and H) CWR0.25 thin film electrodes.

4.2.B.1.3 Stability study:

The electrochemical stability of electrode material is one of the decisive parameters to determine applicability of synthesized thin film electrode for SC device fabrication [33, 34]. The GCD studies at a current density of 2 A g^{-1} were carried out to examine electrochemical stability of both electrodes for 3,000 cycles. The 93% retention of C_s for CWR0.20 electrode for 3,000 GCD cycles are shown in Figure 4.12. CWR0.20 thin film electrode shows improved cycling stability as compared to $CoWO_4$ thin film electrode as rGO sheets assist rapid electron mobility in CWR0.20 composite to accelerate the reversible electrochemical redox reactions. Increased electrical conductivity also results in improved stability of the composite electrode material [35].

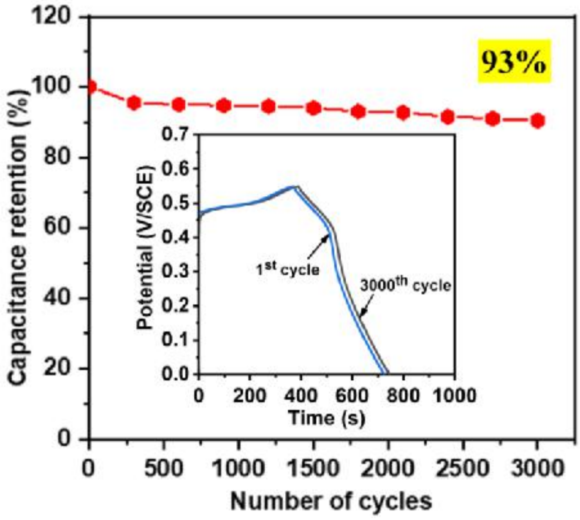

Figure 4.12: Stability curves of CWR0.20 thin film electrode.

SECTION C

Electrocatalytic OER performance of $CoWO_4$@rGO composite thin film electrode

4.2.C.1 Electrocatalytic characterizations of $CoWO_4$@rGO thin films:

4.2.C.1.1 LSV and Tafel slope:

The influence on electrochemical water splitting due to the incorporation of rGO into the active catalyst material was further studied. The concentration of rGO in the reaction solution was varied and the electrochemical performances were analyzed in terms of OER in basic 1M KOH aqueous electrolyte, individually. For that purpose, the electrodes were made by depositing material on SS substrates by means of slurry coating technique.

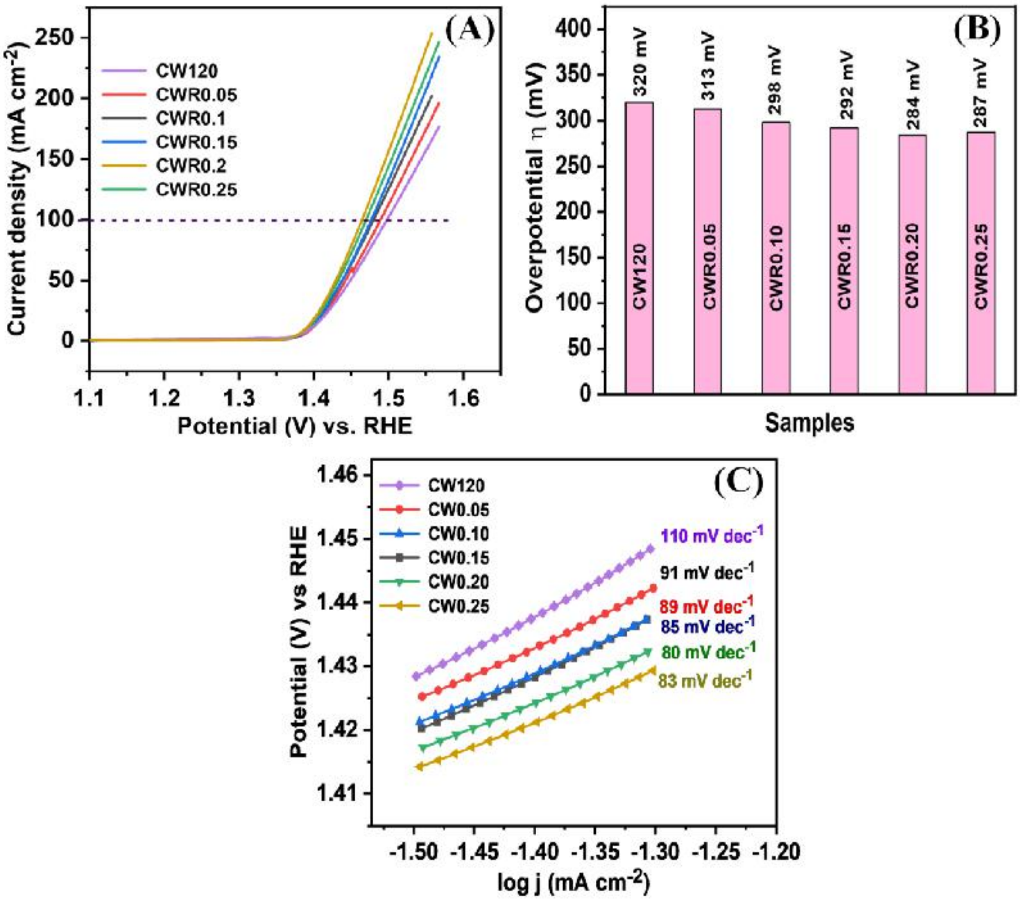

Figure 4.13: Electrochemical OER analysis A) LSV polarization curves, B) comparative bar diagram of overpotentials, C) Tafel plots of the $CoWO_4$@rGO composite electrodes.

The electrochemical water splitting in the form of OER properties of the as prepared $CoWO_4$@rGO composite electrodes were tested. The LSV analysis was conducted to evaluate the catalytic activity in 1 M KOH electrolyte at scan rate of 1 mV/s as shown in Figure 4.13A. The nature of the all LSV polarization curves is similar and continuous change in current density with change in rGO concentration from 0.05 to 0.25 mg/ml. It is observed that due to composition, the material become electrochemically more active. Sample CWR0.20 requires the smallest overpotential of 287 mV to deliver the current density of 10 mA/cm^2 suggesting outstanding oxygen evolution catalyst than the previously reported cobalt-tungstate catalysts. The bar diagram (Figure 4.13B) reveals the values of overpotential for all other electrodes from series. The Tafel slope gives the catalytic activity in the form of reaction rate kinetics indicating diverse rate defining steps surrounded in the reaction process.

By plotting applied potential against the logarithmic current density at the shoot-point of current density, the Tafel plots are shown in Figure 4.13C. Tafel slopes are 91, 89, 85, 80, and 83 mV dec^{-1} for all CWR0.05, CWR0.10, CWR0.15, CWR0.20, and CWR0.25 composite electrodes, respectively [36]. Figure reveals that CWR0.20 electrode has smallest Tafel slope of 80 mV dec^{-1}. It suggests that the OER reaction process is faster and highly efficient reaction kinetics at surface of CWR0.20 electrode. The EIS was carried out to explore the electrochemical kinetics activity [37, 38].

4.2.C.1.2 ECSA analysis:

It is necessary to calculate ECSA related to the double layer capacitance (C_{dl}) of the prepared materials prior to study electrocatalytic OER. The cyclic voltamograms were recorded at different scan rates in non-Faradic region with small potential range as shown in Figure 4.14 (A-F) for all $CoWO_4$@rGO composite electrodes. C_{dl} is calculated by plotting the anodic charging currents (i_c) of each CV curve against the scan rate by the equation (2.9).

By plotting the anodic current versus scan rate (Figure 4.15), the values of C_{dl} have been calculated as 0.24, 0.74, 1.39, 1.80, 1.92, and 1.27 mF cm^{-2} for CW120, CWR0.05, CWR0.10, CWR0.15, CWR0.20, and CWR0.25 composite electrodes, respectively. The ECSA were calculated using C_{dl} values as 18.60, 34.75, 44.25, 48.0, and 45.0 cm^2. The electrocatalytic interface texture can be derived from roughness factor (RF) by dividing the ECSA with the geometric area of the electrode in contact with electrolyte. The values of RF are the same as ECSA values due to 1 cm^2 geometric area in contact with electrolyte.

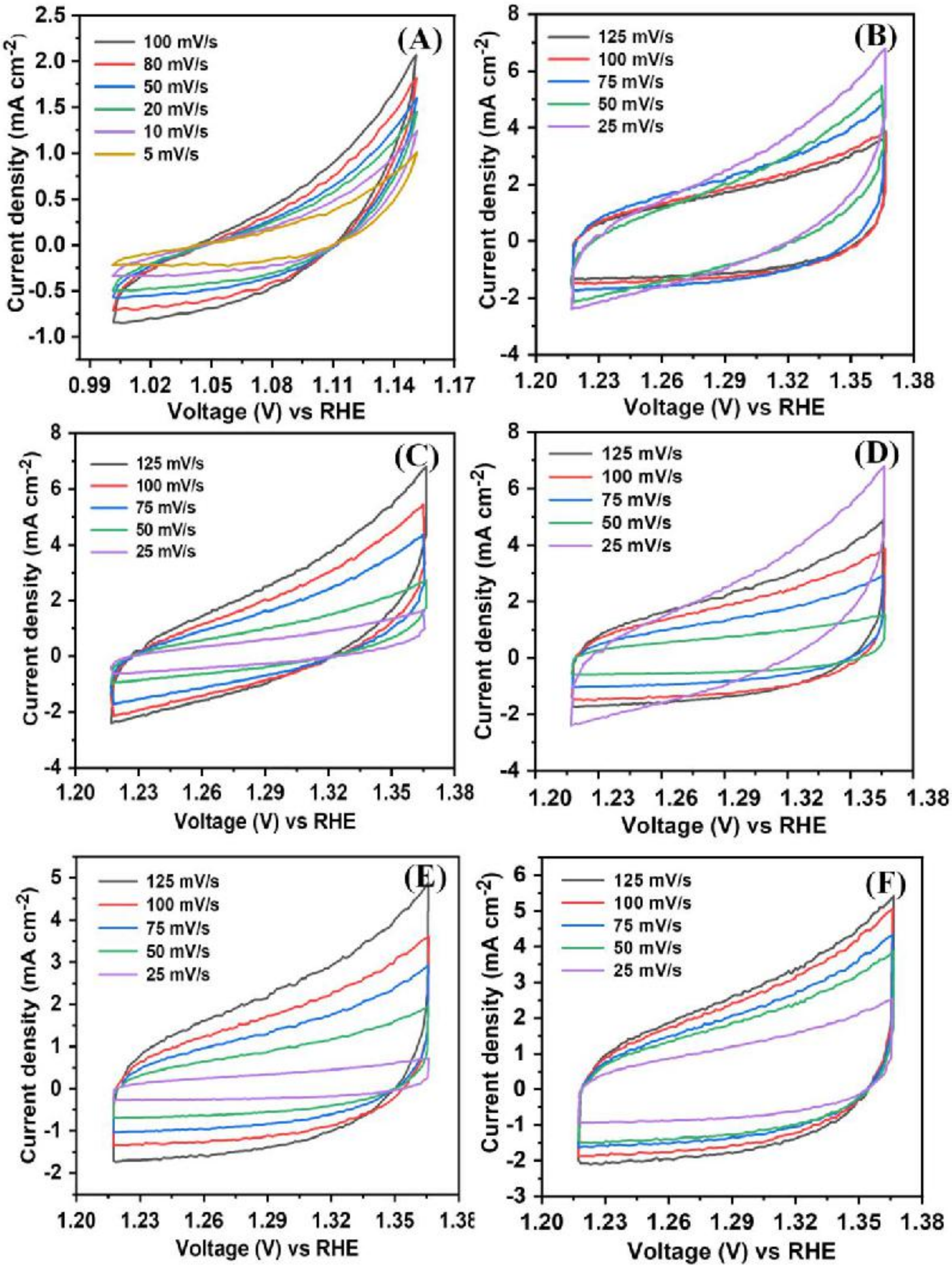

Figure 4.14: The CV curves of A) CW120, B) CWR0.05, C) CWR0.10, D) CWR0.15, E) CWR0.20, and F) CWR0.25 at various scan rates in a potential window of 1.05 - 1.2 V vs RHE.

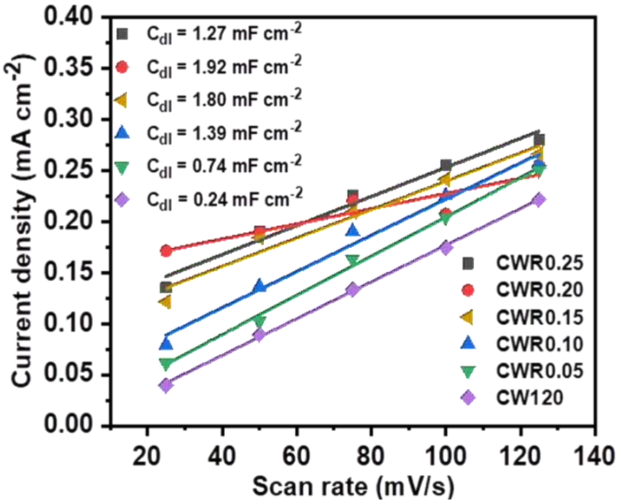

Figure 4.15: Anodic current linear fit for C_{dl} values to calculate ECSA of the CoWO$_4$@rGO series composite electrodes.

4.2.C.1.3 EIS and stability:

The typical Nyquist plots of CWR0.05, CWR0.10, CWR0.15, CWR0.20, and CWR0.25 electrodes with fitted equivalent circuit are presented in Figure 4.13D. Inset shows the EIS circuit and magnification of nyquist plots. The fitted R_{ct} values are 1.20, 1.81, 2.84, 3.25, and 5.29 Ω for CWR0.05, CWR0.10, CWR0.15, CWR0.20, and CWR0.25 electrodes, respectively. It reveals that, easy charge transfer process is one of the reason for low overpotential.

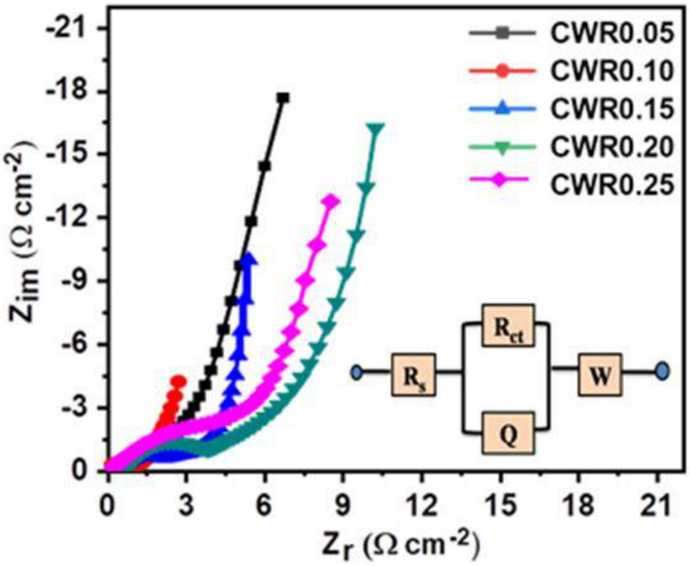

Figure 4.16: Nyquist plots of CoWO$_4$@rGO thin films.

Due to the hybridization of material with rGO, the charge transfer process becomes easy. The EIS data reveals that CoWO$_4$@rGO film electrode has lower resistance and better electrochemical performance. This proves that resistive parameters of electrodes are modified due to lateral paths provided by rGO in $CoWO_4$@rGO composite electrode [37]. The electrochemical impedance spectroscopic fitted circuit parameters for Nyquist plots of $CoWO_4$@rGO thin film electrodes are shown in Table 4.1.

Table 4.1: Electrochemical impedance spectroscopic fitted circuit parameters for Nyquist plots of $CoWO_4$@rGO thin film electrodes.

Parameters	**Electrocatalysts**				
	CWR0.05	**CWR0.10**	**CWR0.15**	**CWR0.20**	**CWR0.25**
R_s (Ω cm^{-2})	0.69	0.65	0.67	0.70	0.73
R_{ct} (Ω cm^{-2})	1.20	1.81	2.84	3.25	5.29
Q	13.80	6.20	6.80	7.00	6.20
W (Ω)	0.56	0.54	0.45	0.65	0.65

The catalytic stability for OER at overpotential was studied by three electrode cell in 1M KOH bath to achieve 10 mA/cm^2 current density for the best performing catalyst.

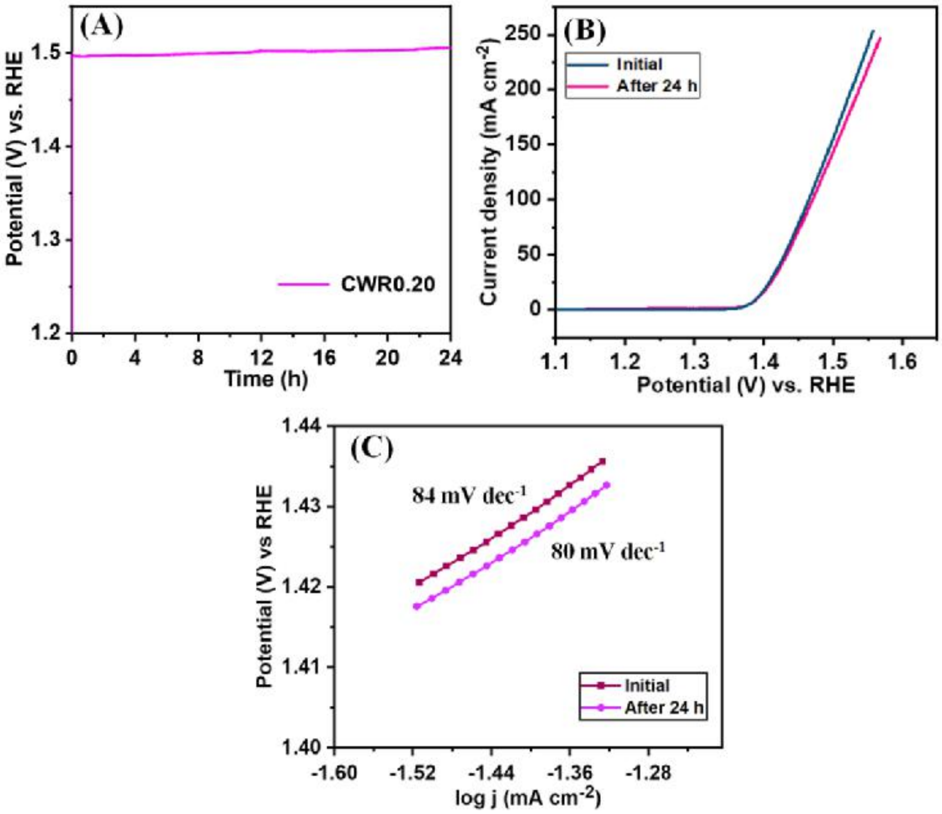

Figure 4.17: A) CA (I-t) curve for OER stability, B) LSV before and after 24 h OER catalysis, and C) Tafel plots extracted from LSV curves before and after stability study.

Figure 4.17A gives the OER catalytic stability test by chromoamperometry (CA) for 24 h. At the initial stage, material started to activate electrochemically and current density rose to 10 mA/cm^2 and became stable. After 24 h, the catalysis remained 97% stable and overpotential becomes 293 mV with loss of small amount of current density as shown by comparative LSV plot (Figure 4.17B). Because of the material consumption in the electrolyte during the catalytic activity, the decrement in catalytic performance was observed by LSV curve [39]. The comparative Tafel slope before and after 24 h catalysis and increase in Tafel slope predicted the slowed down reaction rate (Figure 4.17C).

4.3 Conclusions:

In conclusion, SILAR method is developed to prepare sequential layered $CoWO_4$@rGO composite thin film electrodes directly on SS substrate. The formation of $CoWO_4$@rGO composite material was confirmed by observing their corresponding bonds and elemental content in the prepared samples via EDAX, FT-IR, and XPS. The $CoWO_4$@rGO showed maximum C_s of 1201 F g^{-1} at the scan rate of 5 mV s^{-1} in 1 M KOH electrolyte. The value of R_s decreased for $CoWO_4$@rGO electrode compared to pristine $CoWO_4$. The electrochemical cycling stability of $CoWO_4$@rGO film electrode (93%) is more compared to $CoWO_4$ film electrode (88%). The $CoWO_4$@rGO demonstrates minimum overpotential of 287 mV for OER to deliver the current density of 10 mA cm^{-2} with Tafel slope of 80 mV dec^{-1} and 97% catalytic OER retention after 24 h in alkaline medium. The $CoWO_4$@rGO composite electrode showed better performance for supercapacitive and electrocatalytic properties. These electrochemical investigations indicate that $CoWO_4$@rGO is a good candidate as a future electrode material for energy storage and electrocatalytic applications.

4.4 References:

1] B. Zhao, D. Chen, X. Xiong, B. Song, R. Hu, Q. Zhang, B. Rainwater, G. Waller, D. Zhen, Y. Ding, Y. Chen, C. Qu, D. Dang, C. Wong, M. Liu, Energy Storage Mater., 7 (2017) 32-39.

2] C. Jing, X. Guo, L. Xia, Y. Chen, X. Wang, X. Liu, B. Dong, F. Donge, S. Li, Y. Zhang, Chem. Eng. J., 379 (2020) 122305-122334.

3] A. Fouda, A. Salem, F. El-Tantawy, H. Salem, E. Duraia, Superlattices Microstruct., 124 (2018) 240-247.

4] W. Cui, C. Ge, Z. Xing, A. Asiri, X. Sun, Electrochim. Acta, 137 (2014) 504-510.

5] P. Ren, D. Yan, X. Ji, T. Chen, Z. Li, Nanotechnology, 22 (2011) 055705-055714.

6] S. Chen, G. Yang, Y. Jia, H. Zheng, Chem. Electrochem. 3 (2016) 1490-1496.

7] F. Lei, B. Yan, H. Chen, J. Zhao, J. Am. Ceram. Soc. 92 (2009) 1262-1267.

8] J. Zhang, Y. Zhang, J. Yan, S. Li, H. Wang, F. Huang, Y. Shen, A. Xie, J. Nanopart. Res., 14 (2012) 796-805.

9] S. Molaei and M. Ghadermazi, Solid State Sci. 100 (2019) 106091-106135.

10] P. Bagwade, D. Malavekar, S. Ubale, R. Bulakhe, I. In, U. Patil, C. Lokhande, Solid State Sci., 408 (2022) 139933-139944.

11] X. Xing, Y. Gui, G. Zhang, C. Song, Electrochim. Acta, 157 (2015) 15-22.

12] X. Xu, Y. Yang, M. Wang, P. Dong, R. Baines, J. Shen, M. Ye, Ceram. Int., 42 (2016) 10719-10725.

13] X. Xu, J. Shen, N. Li, M. Ye, Electrochim. Acta, 150 (2014) 23-34.

14] R. Wu, X. Qian, X. Rui, H. Liu, B. Yadian, K. Zhou, J. Wei, Q. Yan, X. Feng, Y. Long, L. Wang, Y. Huang, Small, 10 (2014) 1932–1938.

15] F. Li, H. Na, W. Jin, X. Xu, W. Wang, J. Gao, J. Solid State Electrochem., 22 (2018) 2767-2774.

16] D. Malavekar, V. Lokhande, D. Patil, S. Kale, U. Patil, J. Colloid Interface Sci., 609 (2022) 734-745.

17] P. Bagwade, D. Malavekar, T. Ghogare, S. Ubale, V. Mane, R. Bulakhe, I. In, C. Lokhande, J. Alloys Compd., 859 (2021) 157829-157848.

18] M. Wang, W. Wang, X. Guo, RSC Advances, 4 (2014) 39625-39633.

19] Z. Dai, H. Geng, J. Wang, Y. Luo, B. Li, Y. Zong, J. Yang, Y. Guo, Y. Zheng, X. Wang, Q. Yan, ACS Nano., 11 (2017) 11031-11040.

20] P. Katkar, S. Marje, S. Pujari, S. Khalate, A. Lokhande, U. Patil, ACS Sustain. Chem. Eng., 7 (2019) 11205-11218.

21] G. Beamson and D. Briggs, High Resolution XPS of Organic Polymers: The Scienta ESCA300 Database, John Wiley and Sons, New York, 318 (1992) 128-189.

22] P. Shinde, A. Lokhande, N. Chodankar, A. Patil, J. Kim, C. Lokhande, Electrochim. Acta, 224 (2017) 397-404.

23] H. Handal, N. Ghany, G. Elsherif, A. Siebel, N. Allam, Electrochim. Acta, 401 (2022) 139494-139502.

24] Y. Zhang, L. Li, H. Su, W. Huang, X. Dong, J. Mater. Chem. A, 3 (2015) 43-59.

25] N. Shi, S. Xiong, F. Wu, J. Bai, Y. Chu, H. Mao, B. Xi, (2017), Eur. J. Inorg. Chem., 3 (2017), 734-740.

26] S. Jadhav, D. Malavekar, R. Bulakhe, U. Patil, I. In, C. Lokhande, P. Pawaskar, Surf. Interfaces, 23 (2021) 101018-101027.

27] P. Xu, K. Ye, D. Cao, J. Huang, T. Liu, K. Cheng, J. Yin, G. Wang, J. Power Sources, 268 (2014) 204-211.

28] C. Sun, F. Li, C. Ma, Y. Wang, Y. Ren, W. Yang, Z. Ma, J. Li, Y. Chen, Y. Kim, L. Chen, J. Mater. Chem. A, 2 (2014) 7188-7196.

29] G. Ojha, B. Pant, A. Muthurasu, S. Chae, S. Park, T. Kim, H. Kim, Energy, 188 (2019) 116066-116078.

30] M. Wimmer, M. Kaes, C. Dellen, M. Salinga, Front. Phys., 2 (2014) 1-12.

31] U. Patil, M. Nam, J. Sohn, S. Kulkarni, R. Shin, S. Kang, S. Lee, J. Kim, S. Jun, J. Mater. Chem. A, 2 (2014) 19075-19083.

32] D. Dubal, D. Dhawale, R. Salunkhe, V. Fulari, C. Lokhande, J. Alloys Compd., 497 (2010) 166-170.

33] J. Theerthagiri, K. Thiagarajan, B. Senthilkumar, Z. Khan, R. Senthil, P. Arunachalam, J. Madhavan, M. Ashokkumar, Chem. Sel., 2 (2017) 201-210.

34] M. Zhang, H. Fan, N. Zhao, H. Peng, X. Ren, W. Wang, H. Li, G. Chen, Y. Zhu, X. Jiang, P. Wu, Chem. Eng. J., 347 (2018) 291-300.

35] K. Adib, M. Rahimi-Nasrabadi, Z. Rezvani, S. Pourmortazavi, F. Ahmadi, H. Naderi, J. Mater. Sci. Mater. Electron., 27 (2016) 4541-455.

36] H. Yue, Q. Li, D. Liu, X. Hou, S. Bai, S. Lin, D. He, J. Alloys Compd., 744 (2018) 243-251.

37] C. McCrory, S. Jung, J. Peters, T. Jaramillo, J. Am. Chem. Soc. 135 (2013) 16977-16987.

38] S. Zou, M. Burke, M. Kast, J. Fan, N. Danilovic, S. Boettcher, Chem. Mater., 27 (2015) 8011-8020.

39] R. Cong, J. Y. Choi, J. B. Song, M. Jo, H. Lee, C. Lee, Sci. Rep., 11(2021) 1-11

CHAPTER-5

Fabrication and performance evaluation of asymmetric FSS–ASCs device based on $CoWO_4$@rGO and CuS thin films

CHAPTER 5

Fabrication and performance evaluation of asymmetric FSS–ASCs device based on $CoWO_4$@rGO and CuS thin films

SECTION-A

Synthesis, characterization and supercapacitive performance of CuS thin films

Section B

Fabrication of asymmetric FSS–ASCs device based on $CoWO_4$@rGO and CuS thin films

5.1 Introduction:

In recent times, extensive research exertions have been dedicated to the preparation of transition-metal sulfides which have differents to ichiometric compositions, crystal structures, oxidation states, providing them redox activities. It is possible to achieve higher specific capacitance using metal sulphides compared to other electrode materials [1, 2]. As compared to metal oxides, consistent transition-metal sulfides show improved electrical conductivity as well as thermal stability. Especially, ternary metal sulfides can offer comfortable redox reactions, resulting in higher C_s [3]. Among metal sulfides, CuS is a significant multifunctional semiconductor material with excessive applications in lithium ion batteries, solar energy devices and gas sensors [4-6]. Furthermore, CuS displays a property of characteristic of ion exchange processes. This permits to prepare different materials without the destruction of morphology by exchanging Cu or S for other elements [7]. Hence, it is noteworthy for CuS and CuS-derived materials for study the connection between the morphology and electrochemical supercapacitive property. The supercapacitive performance of electrode materials mainly depend on surface morphologies. Recently, nanostructured electrodes have much attention as supercapacitor electrode materials due to availability of large electroactive sites [8-10].

Presently, some efforts have been made to explore CuS as an electrode material for supercapacitors due to its electronic conductivity ($10s^{-1}$ S cm^{-1}) and high theoretical capacity (561 mAh g^{-1}) [11, 12]. Nevertheless, it is not auspicious for applications in electrochemical superpcapacitor because of semiconductor like properties of pure CuS. Also, cycling stability of CuS electrode material is less as compared to carbon nanomaterials [13-17]. Thus, it is highly necessary to have geometrically control during preparation of CuS composites. The strategy to enhance the supercapacitor performance of CuS is to combine with electronically conductive substance like SS substrate.

SECTION -A

Synthesis, characterization and supercapacitive performance of CuS thin films

5.2.A.1 Introduction:

The present section deals with the synthesis and characterization of CuS thin film by SILAR method.

5.2.A.2 Experimental details:

5.2.A.2.1 Chemicals:

For preparation of CuS thin film, copper sulphate ($CuSO_4$), triethylamine (TEA), hydrochloric acid (HCl) and sodium thiosulfate pentahydrate ($Na_2S_2O_3.5H_2O$) were used without further purification (Sigma Aldrich). Acetone and KOH were provided by Loba chemicals. The commercially available flexible SS material (304 grade) was used as current collector material.

5.2.A.2.2 Synthesis of CuS thin films:

To deposit CuS thin film; solutions of 0.1 M $CuSO_4$ (50 mL) and 0.05 M Na_2S (50 mL) were used as cationic and anionic sources, respectively. The SS substrate was immersed in the cationic precursor for 30 s, followed by 25 s rinsing in DDW. The same substrate was immersed in an anionic precursor for 30 s for reaction purposes and further rinsed in DDW for 25 s to remove loosely bounded CuS molecules. Thus a single cycle of SILAR forms a monolayer of CuS; further, such 100 cycles were repeated to get adherent thickness of CuS on SS substrate.

5.2.A.3 Results and discussion:

5.2.A.3.1 XRD study:

The XRD pattern of CuS thin film is presented in Figure 5.1A. The XRD patterns of CuS thin film sample do not show any peak of desired materials rather than SS peak denoted by sign #; which confirms amorphous nature of films [3]. Amorphous nature of thin film is beneficial to enhance electrochemical activities because of more active sites are available due to irregular arrangement of the particles. Broad peaks confirm the amorphous nature of the film. No other diffraction peak was observed indicating the absence of any other impurity.

5.2.A.3.2 FT-IR study:

The molecular bond vibrations in CuS thin film deposited at 100 cycles was investigated using FT-IR. The FT-IR absorption spectrum in the wavenumber range of 4000-400 cm^{-1} of CuS is shown in Figure 5.1B. The strong absorption bands at 617, 830 and 1115 cm^{-1} are assigned to the characteristic absorption of CuS [19]. The broad absorption peaks at 1338 and 1598 cm^{-1} indicate the presence of -OH bond of adsorbed H_2O; also, broad peak at 3390 cm^{-1} is associated with bonded and nonbonded -OH groups from adsorbed water molecules [20]. The results of FT-IR study confirms presence of adsorbed water in the prepared CuS thin film. From the results, formation of CuS on SS substrate was confirmed.

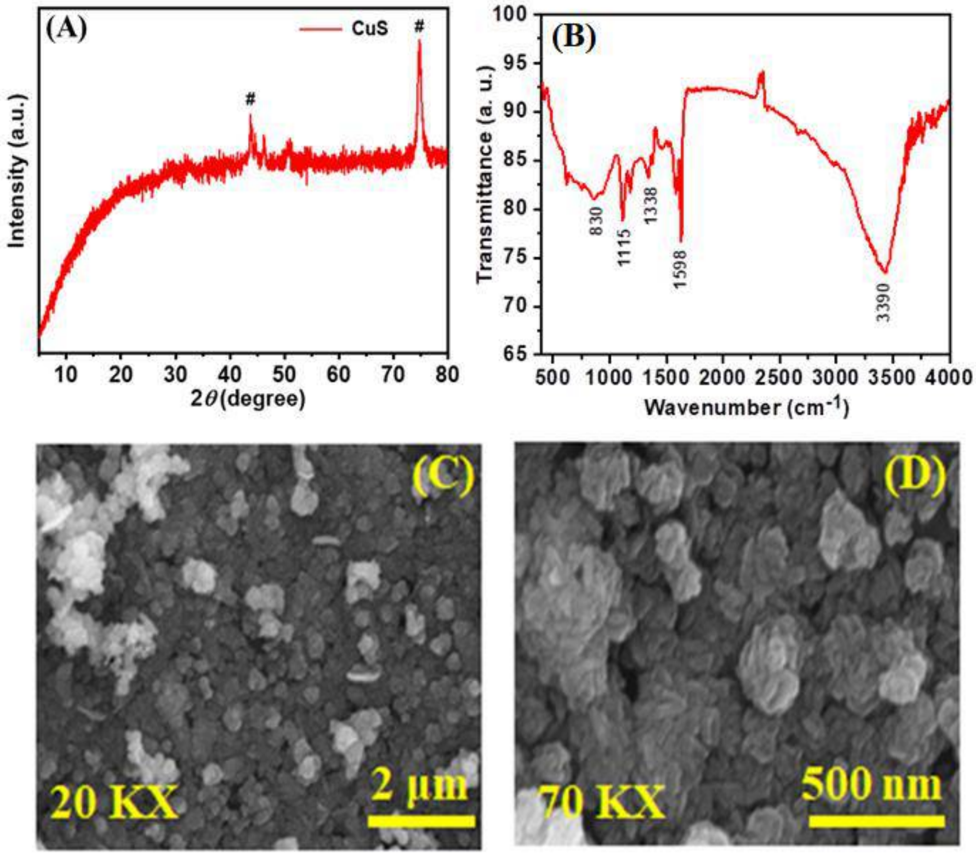

Figure 5.1: A) The XRD pattern, B) the FT-IR pattern, and C), and D) FE-SEM of CuS thin film at different magnifications.

5.2.A.3.3 FE-SEM study:

It is known that, the performance of active material is extensively related to morphology of electrode material. The material with microstructured morphology may improve specific surface area allowing easy adsorption/desorption of electrolytic ions and it enhances electrochemical performance of the electrode. The FE-SEM images of CuS thin film deposited on the SS substrate at two different magnifications (20 KX and 70 KX) are shown in Figure 5.1 (C-D). The FE-SEM images reveal the random arrangement of particles is attributed to the higher reaction rate in the alkaline bath in which nucleation and grain growth take place simultaneously [21]. The FE-SEM images of CuS film shown in Figure 5.1 C) and D) indicate sponge like porous structure consisting of uniform nanoparticles. Most importantly, the nanoflakes are interconnected with each other, which help efficiently to carry electrons from active material to the current collector.

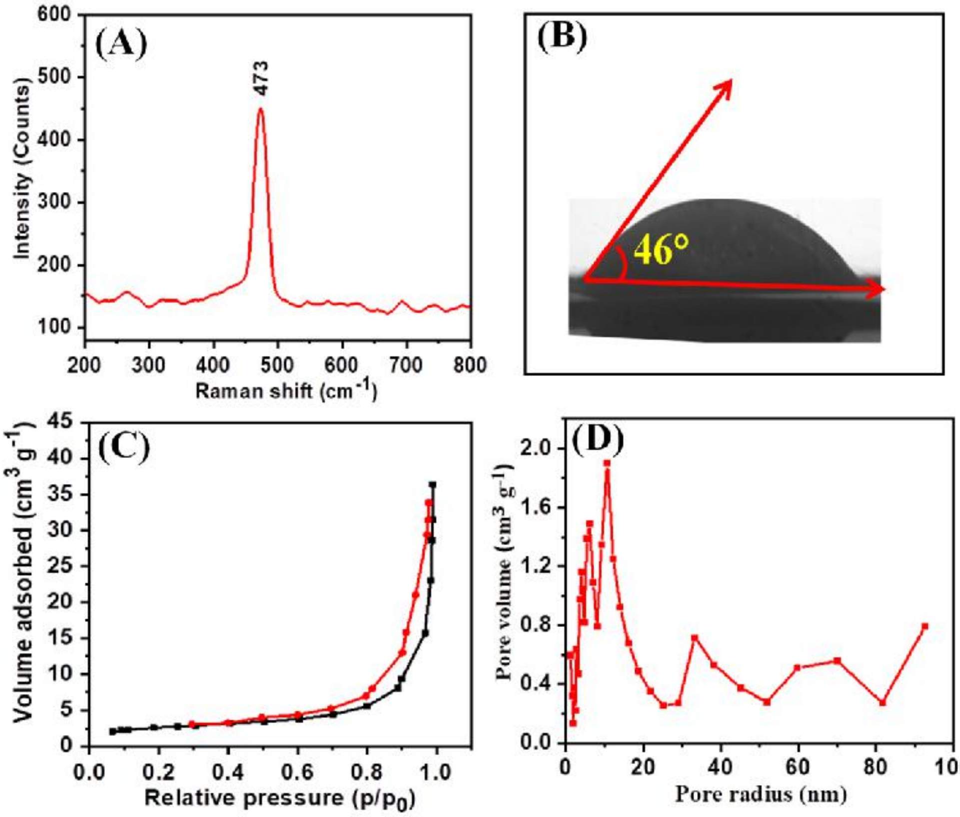

Figure 5.2: A) The Raman spectrum, B) photograph of water contact angle, C) N_2 adsorption isotherms, and D) BJH pore size distribution curve of CuS thin film.

5.2.A.3.4 Raman study:

The Raman spectroscopic study of CuS thin film was carried out using Ar laser with an excitation wavelength of 473 nm which explores the chemical bonding of the material. The Raman spectrum of CuS thin film recorded over 200-800 cm^{-1} is shown in Figure 5.2A. The sharp peak at wavenumber 473 cm^{-1} corresponds to S-S bonding in CuS film. Bulakhe et al. [22] reported similar results for Cu_2S compound.

5.2.A.3.5 Surface wettability:

The nature of surface structure of solid film creates considerable impact on the wettability of the water based electrolytes with film surface. The smaller contact angle and higher surface energy has profoundly positive influence on the electrochemical performance of the material. The particle shape, particle size, purity, roughness, cleanliness of surface and heterogeneity affect the contact angle values [23]. The hydrophilic nature is suitable for SCs application as it provides more interface for electrolyte ions with active electrode. The water contact angle image of CuS film is shown in Figure 5.2B. The contact angle of CuS thin film is 47°. The porous surface of CuS film is beneficial for lower water contact angle. The hydrophilic nature of the thin film surface helps to create intimate contact with the water based electrolyte which may result in the lower contact resistance.

5.2.A.3.6 BET study:

It is well known that as the specific surface area of the electrode material increases, the charge accumulation on the electrode increases in proportion. The specific surface area and average pore size distribution of material scratched from CuS thin film electrode were measured by N_2 sorption isotherms. CuS thin film exhibits type IV isotherms (Figure 5.2C) having a H_3-type hysteresis curve in the range of 0.40 to 1.0 of relative pressure, indicating the presence of meso and micropores [24]. The average pore diameter of the electrodes was analysed by Barrett- Joyner-Halenda (BJH) method and results are provided in Figure 5.2D. The BET specific surface area of CuS sample is 32.4 $m^2\ g^{-1}$ and observed average pore diameter is 29 nm.

5.2.A.4 Supercapacitive performance of CuS thin films:

5.2.A.4.1 CV study:

The electrochemical evaluation of CuS thin films was carried out in an aqueous 1 M KOH electrolyte. The potential window for CuS electrode was 0.0 to -1.2 V/SCE. The CV curves are shown in Figure 5.3 A, with different scan rates ranging from 5 to 100 mV s^{-1}. From CV curves, it is seen that strong oxidation and reduction peaks for CuS arise at a potential of -0.43 and -0.37 V/SCE, respectively. The area under CV curves is directly proportional to the scan rate.

The current response of CuS film electrode in CV curves is more, indicating CuS may facilitate fast electronic and ionic transport. The change of oxidation states of Cu^{2+} at an interface of CuS and electrolyte is shown in the following equation,

$$Cu^{(II)}S + xK^+ \rightarrow Cu^{(I)}S.K_x^+ + e^- \qquad (5.1)$$

The CuS electrode has excellent supercapacitive capacitance, as 687, 550, 420, 310, and 270 F g^{-1} of C_s at scan rates of 5, 10, 20, 50 and 100 mV s^{-1}, respectively. The non-rectangular nature of CV curves indicates reversible faradic reactions at the electrode surface i.e. change in the oxidation state of the electrode material [25]. Variations of C_S with scan rate is illustrated in Figure 5.3B, at high scan rate, the large amount of electrode material remains unutilized due to fast intercalation-deintercalation process hence C_S decreases as scan rate raises.

5.2.A.4.2 GCD study:

The GCD curves of CuS electrode at different current densities are shown in Figure 5.3C. The electrode exhibit C_S of 672, 500, 390, 250, and 180 F g^{-1} at current densities 3 to 7 F g^{-1}, respectively. The variation of C_S with different current densities are shown in Figure 5.3D.

5.2.A.4.3 EIS study:

The EIS analysis was carried out to understand the resistive parameters of (CuS) electrolyte junction, Figure 5.3E shows Nyquist plot of CuS electrode at potential amplitude of 10 mV between frequency range 100 kHz to 100 mHz. The observed value of solution resistance (R_s) is 0.52 Ω cm^{-2}. The lowest value of R_s is attributed to the direct contact of electrode material to the substrate. The initial barrier in the electrochemical reactions is the charge transfer resistance (R_{ct}) which is represented by the semicircle in the Nyquist plot [26]. A lower value of the R_{ct} (17.4 Ω cm^{-2}) for the electrode-electrolyte system represents facile charge transfer at the electrode-electrolyte interface. The Warburg resistance obtained from matched equivalent circuit (Inset of Figure 5.3E) is 0.041Ω.

5.2.A.4.4 Stability study:

The stability of CuS electrode is tested for 3,000 GCD cycles at the current density of 3 F g^{-1}. As shown in Figure 5.3F, 89 % capacitance is retained by the electrode after 3,000 cycles. Image in inset (Figure 5.3F) shows 1nd and 3000th cycles from the GCD curves. The small drop in peak current after the cycling suggests the decrease in active sites of the electrode.

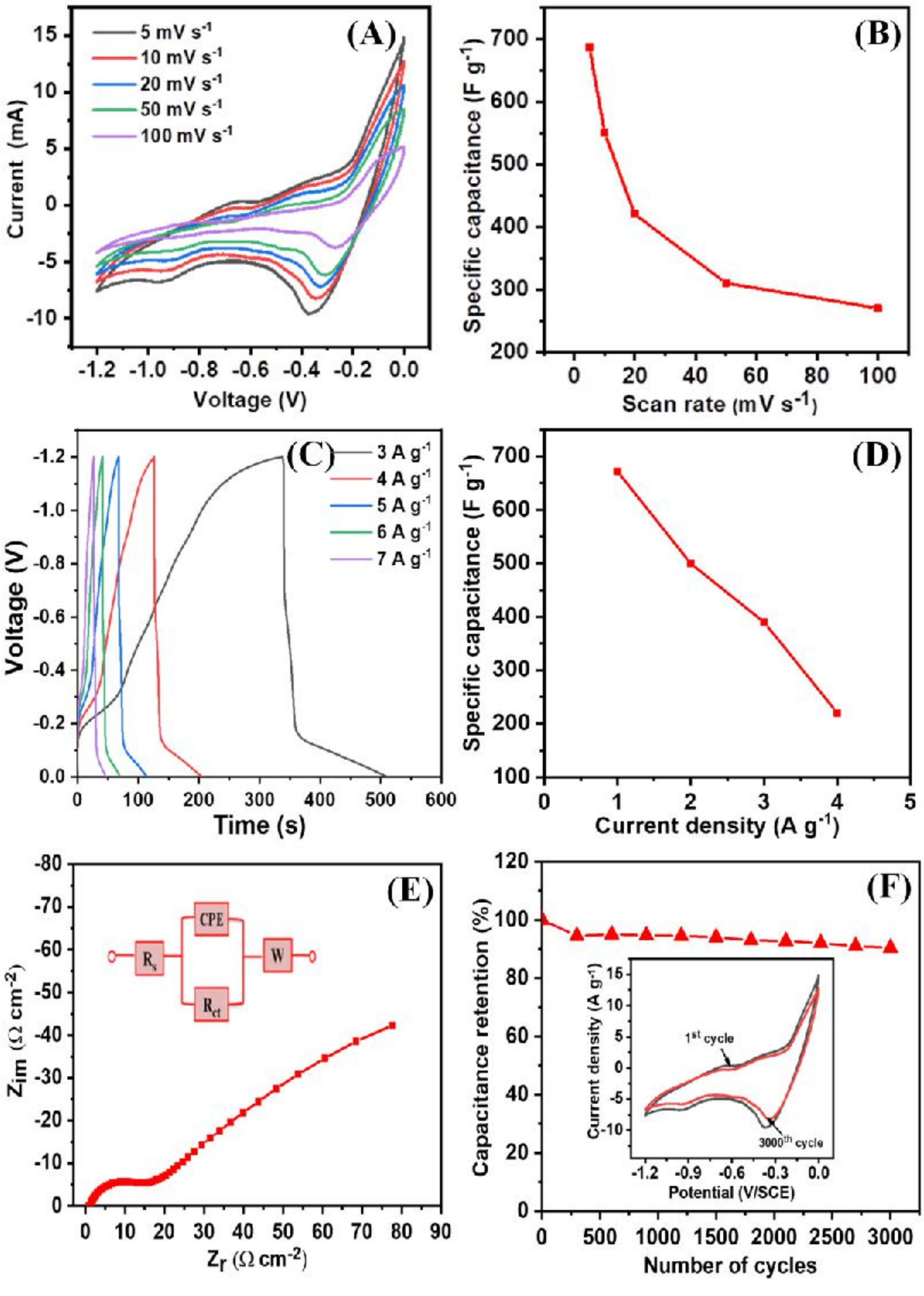

Figure 5.3 A) The CV curves of CuS electrode at different scan rates ranging from 5 to 100 mV s^{-1}, B) the variation of specific capacitance with applied scan rates, C) the GCD curves of CuS electrode at different current densities, D) the variation of specific capacitance with applied current densities, E) Nyquist plot of CuS electrode, and F) capacitance retention of CuS electrode (Inset show the CV curves of 1st and 3000th cycle).

SECTION-B

Fabrication of asymmetric FSS–ASCs device based on $CoWO_4$//rGO and CuS thin films

5.3.B.1 Introduction:

The portable and small size SCs are required in the fabrication of recent energy storage devices [27, 28]. The mechanical flexibility, lightweight, inexpensive, and environment friendly energy storage of SCs provides uses in portable, wearable, and commercialized pocket electronic devices [29, 30]. There is a need to increase S_E and S_P of energy storage devices using different electrode materials and electrolytes. The asymmetric design of SC is an effective method to enhance the operating voltage of the device [31]. The specific energy (S_E) and C_s of asymmetric supercapacitor (ASCs) are higher as compared to the symmetric supercapacitor (SSCs) [32-35]. Various combinations of the anode and cathode have been reported in literature as, MnO_2//CuS [36], CuS–AC//AC [37], CuS@CD//RGO [38], Co_3O_4@$CoWO_4$//rGO [39], $CoWO_4$//NRGO [40]. The solid electrolyte based SC holds many advantages such as small size, lightweight, excellent reliability, and a wider range of operating temperature. The polymer based gel electrolytes offer mechanical flexibility to the SC devices [41, 42].

The transition metal based electrode chalcogenides such as copper sulfide can be operated in the wide potential window. Therefore, the combination of polymeric gel electrolytes with these electrode materials will be a good contribution to the FSC devices. The $CoWO_4$@rGO holds great attention as a positive electrode to fabricate the FSS–ASCs device due to higher C_s and operating voltage as compared to carbon based materials. In addition, the low cost, large abundance, higher conductive and nontoxic nature of copper based chalcogenides makes them possible to develop the FSS–ASCs devices [43-45].

In this section, FSS–ASC device is fabricated using $CoWO_4$@rGO thin film as an anode and CuS thin film as a cathode with ionically conducting PVA–KOH gel as an electrolyte as well as a separator. This section deals with the fabrication and electrochemical performance evaluation of flexible solid state asymmetric supercapacitor (FSS–ASCs) device with configuration of $CoWO_4$@rGO//CuS.

5.3.B.2 Experimental details:

5.3.B.2.1 Introduction:

The present section describes the electrode preparation (CuS, $CoWO_4$ and $CoWO_4$@rGO) by SILAR method, polymer gel electrolytes (PVA-KOH) preparation and fabrication of $CoWO_4$@rGO//CuS FSS-ASCs device.

5.3.B.2.2 Preparation of polymer gel electrolytes:

To fabricate FSS-ASCs device, water soluble PVA polymer was selected to prepare gel electrolyte using salt of KOH. To prepare polymer based PVA-KOH gel electrolyte, 3 g PVA was added in 30 mL DDW and mixed properly with continuous heating for 4 h at 350 K and to it, 1 M KOH [20 mL] solution was added slowly. This solution was stirred continuously, till it becomes transparent. This polymer based gel electrolyte was used to fabricate FSS-ASCs device. This viscous solution was used as a gel electrolyte to fabricate CuS//$CoWO_4$@rGO FSS-ASCs device. A similar process is followed to prepare PVA-KOH gel electrolyte.

5.3.B.2.3 Fabrication of FSS–ASCs devices:

The FSS–ASCs device having configuration CuS/PVA-KOH/rGO@$CoWO_4$ was fabricated employing CuS and $CoWO_4$@rGO thin films as cathode and an anode, respectively and PVA-KOH gel as solid-state electrolyte. The electrodes of size 5 × 5 cm^2 were used. Initially, PVA-KOH gel electrolyte was applied uniformly on both electrodes and allowed to dry at room temperature to remove the water content. The edges of electrodes were sealed with plastic tape to avoid short circuit. After drying one more time polymer gel electrolyte was painted on electrodes for proper contact between electrode and electrolyte. Then for fabricating the device, both electrodes were pressed in such a way that PVA-KOH electrolyte was sandwiched between them. The device thickness measured using a digital micrometer screw was found to be 0.565 ± 0.001 mm.

5.3.B.3 Electrochemical performance of $CoWO_4$@rGO//CuS FSS-ASCs device:

The FSS-ASC device with configuration CuS/PVA-KOH/rGO@$CoWO_4$ was fabricated having area 5 × 5 cm^2. The rGO@$CoWO_4$ and CuS electrodes were used as an anode and an cathode, respectively. By considering the operating potential window of the two electrodes, the optimized voltage of 1.7 V was used for the ASC device. Different CV curves of FSS-ASC device at scan rate of 100 mV s^{-1} within voltage 0.0 to +1.7 V are shown in Figure 5.4A. The GCD curves at voltages varying from 0 to +1.7 V at an applied current of 5 A g^{-1} are shown in Figure 5.4B. The maximum possible working voltage for water based electrolyte depends on electrode materials. So, from analysis of CV and GCD curves, a suitable working voltage of +1.7 V was decided and further electrochemical characterizations were carried out in that working voltage (0 to +1.7 V).

Also, Figure 5.4C shows CV curves at the scan rates 5-100 mV s^{-1} in voltage 0 to +1.7 V. All CV curves show improved current response. At the scan rate of 5 mV s^{-1}, the maximum C_s of 158 F g^{-1} was observed. Also, the GCD curves at different current densities of 2, 3, 4, and 5 A g^{-1} are displayed in Figure 5.4D. The curves show excellent pseudo-capacitive behavior within a given potential window. The C_s of FSS-ASC decreases with respect to the scan rate as shown in Figure 5.4E. The constituting electrodes possess excellent capacitance and rate performance which results in the extraordinary electrochemical activity of the FSS-ASC device. The capacitance was decreased from 122 to 25 F g^{-1} for the increase in charge-discharge current from 2 to 5 A g^{-1}, as exhibited in Figure 5.4F.

The value of S_E obtained by the present FSS-ASC device is 53 Wh kg^{-1} at a S_P of 1080 W kg^{-1}. Figure 5.5A exhibits the plots of S_E and S_P. Mechanical flexibility without losing the electrochemical efficiency of the SC is important for the usefulness of the device in different portable and flexible electronic devices [46, 48]. Therefore, for flexibility measurement of FSS-SSC device, the CV analysis was performed at bending angle of 0°, 45°, 90° and 165°, and corresponding voltammograms are shown in Figure 5.5B. It is inspiring to note that the shape of CV curves are the same even when the device was bent at an angle of 165°, highlighting extreme adherent nature of the electrode material with SS substrate. Also, it affirms the good contact between the electrode-electrolyte interface. Figure 5.5C shows the percent C_s retention versus bending angle and it is observed that the device retains 90% of initial C_s even at the twisting of the device at an angle of 165º.

The resistive characteristics of CuS//$CoWO_4$@rGO device were evaluated by EIS measurement in the frequency range of 0.01 Hz to 0.1 MHz. EIS measurement of the asymmetric device was performed in order to understand the capacitive, electronic, and ionic resistive properties of the device. Figure 5.5D shows a Nyquist plot of the CuS//$CoWO_4$@rGO device with a fitted circuit. As depicted in Figure 5.5D, the intercept at real Z-axis is related to the solution resistance (R_s), and it is observed to be 2.1 Ω. Also, the charge transfer resistance (R_{ct}) is 3.5 Ω. The low R_s and R_{ct} values manifesting the good conductivity of the electrolyte and very low internal resistance of the electrode [49, 50]. The low value of the R_{ct} for FSS-ASC is the cause of the improved values of the C_s, S_E and S_P.

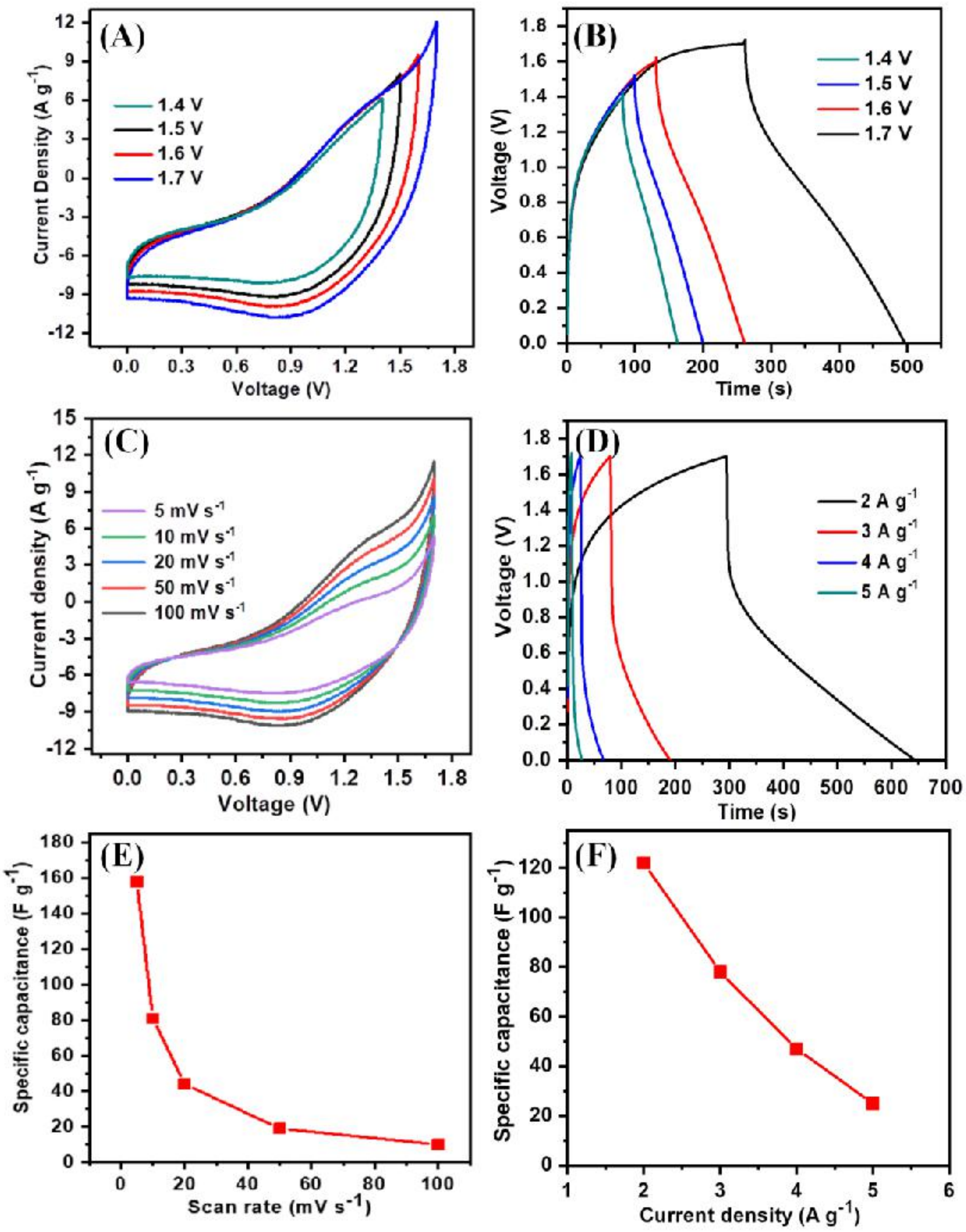

Figure 5.4: A) The CV curves, B) the GCD curves at different voltage ranges (0 V to 1.7 V), C) the CV curves at various scan rates, D) the GCD curves at various current densities, E) variation of specific capacitance with the scan rate, and (F) variation of specific capacitance with applied current densities of CuS//CoWO$_4$@rGO ASC device.

The life span of SC is considered as a core parameter that reduces the cost of maintenance of any portable electronic device that leads to economically affordable appliances. The C_s retention over a large number of cycles is one of the major needs of FSS-ASC devices and to test cycling stability of FSS-ASC device 5000 CV cycles were repeated at the scan rate of 100 mV s^{-1}. The plot of the C_s retention versus cycle number is shown in Figure 5.5E. Inset shows 2nd and 5000th CV curves. The excellent electrochemical stability (94%) can be accredited to a proper combination of faradic and pseudocapacitive electroactive material forming a porous hybrid electrode with an appropriate pore size [51]. The excellent performance of FSS-ASC is a result of good contact establishment between gel electrolyte and electrode material. In general, FSS-ASC (CuS//$CoWO_4$@rGO) device shows excellent supercapacitive features.

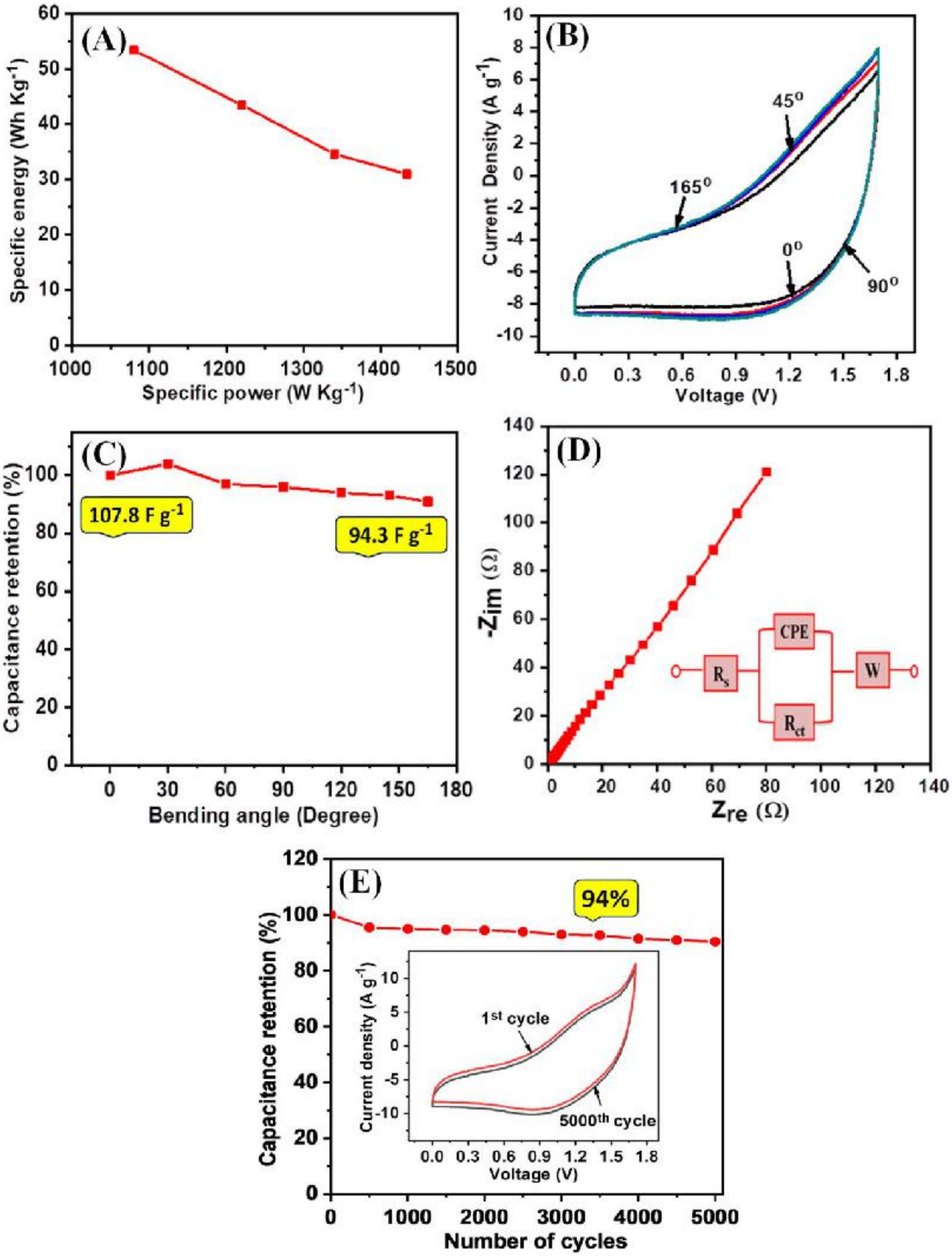

Figure 5.5: A) Ragone plot, B) the CV curves at different bending angles, C) change in specific capacitance with different bending angles, D) The Nyquist plot (Inset shows equivalent circuit), and E) variation of specific capacitance with CV cycles (Inset show 1st and 5000th cycles) of CuS//$CoWO_4$@rGO ASC device.

5.3.B.4 Demonstration of CuS//$CoWO_4$@rGO FSS-ASCs device:

For practical demonstration, two asymmetric devices (5 × 5 cm^2) were connected in series. Each device has an operating voltage of 1.7 V, which in turn provides potential of 3.4 V for charging. Initially, these CuS//$CoWO_4$@rGO devices were charged at 3.4 V for 30 s and discharged through LEDs panel consisting of 211 red LEDs. The discharging of the CuS//$CoWO_4$@rGO device through LEDs panel was observed for more than 150 s. Fig. 5.6 (A-C) demonstrates photographs captured while discharging an CuS//$CoWO_4$@rGO device at 4, 9 and 150 s. The measured power output of single device (0.179 mW cm^{-2}) signifies excellent charge storage capability of a CuS//$CoWO_4$@rGO device.

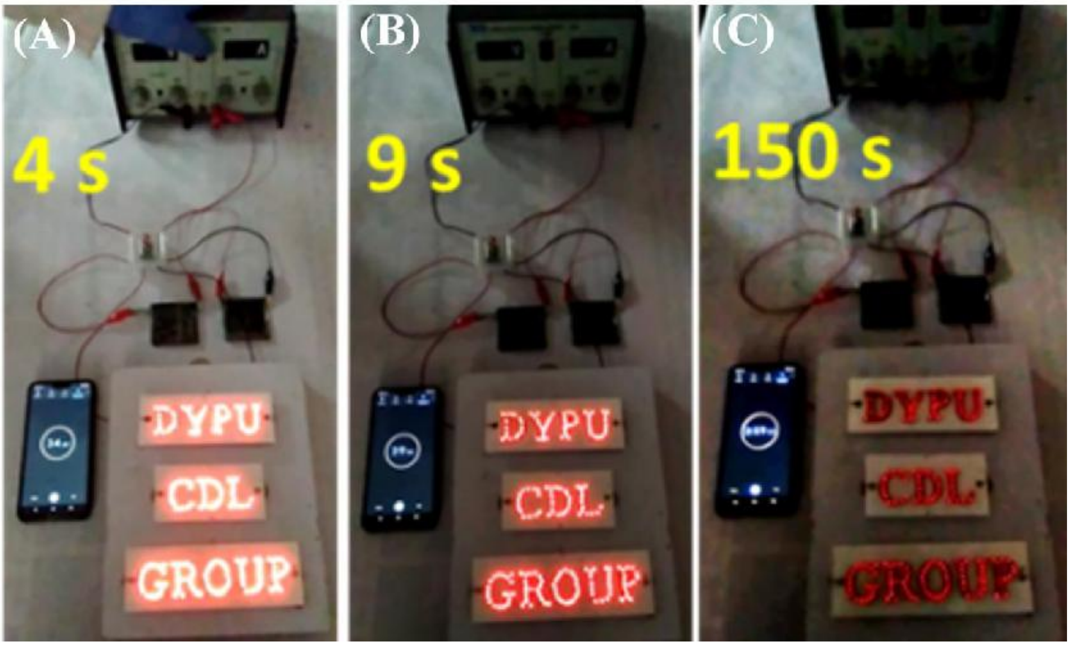

Figure 5.6. A-C) Photographs of two series connected CuS//$CoWO_4$@rGO devices charged at +3.4 V for 30 s, and the discharged through a panel of 211 red LEDs (DYPU CDL GROUP) glows for 150 s.

5.4 Conclusions:

In summary, CuS//$CoWO_4$@rGO asymmetric FSS-ASC device has been fabricated using CuS as a negative and $CoWO_4$@rGO as a positive electrode using PVA-KOH gel electrolyte. The CuS//$CoWO_4$@rGO FSS-ASCs device exhibits the excellent electrochemical performance with a maximum specific capacitance of 158 F g^{-1}, energy density of 53 Wh kg^{-1} and power density of 1080 kW kg^{-1}. Furthermore, CuS//$CoWO_4$@rGO FSS-ASC device reveals excellent cycling stability of 94% with a wide operating potential window of +1.7 V for 5000 CV cycles. The CuS//$CoWO_4$@rGO asymmetric FSS-ASC device displays outstanding mechanical flexibility and high rate capability. In an actual demonstration of CuS//$CoWO_4$@rGO asymmetric FSS–ASC device, 201 red LEDs is illuminated using a series combination of two CuS//$CoWO_4$@rGO asymmetric FSS-ASCs devices (area of 5 × 5 cm^2). The series combination of two CuS//$CoWO_4$@rGO asymmetric FSS-SCs devices gives maximum power of 0.350 W. This shows the possible use of CuS//$CoWO_4$@rGO asymmetric FSS-ASC device for supercapacitor applications.

5.5 References:

1] D. Dubal, J. Kim, Y. Kim, R. Holze, C. Lokhande, W. Kim, Energy. Technol., 2 (2014) 325-341.

2] S. Shi, C. Xu, C. Yang, J. Li, H. Du, B. Li, F. Kang, Particuology, 11 (2013) 371-377.

3] L. Nyholm, G. Nystrom, A. Mihranyan, M. Stromme, Adv. Mater., 23 (2011) 3751- 3769.

4] P. Wen, M. Fan, D. Yang, Y. Wang, H. Cheng, J. Wang, J Power Sources, 320 (2016) 28-36.

5] B. Choi, S. Chang, C. Park, H. Kang, H. Kim, W. Hong, S. Lee, Y. Huh, Nanoscale, 4 (2012) 4983-4988.

6] H. Cheng, Z. Dong, C. Hu, Y. Hu, L. Qu, Y. Zhao, N. Chen, L. Dai, Nanoscale, 5 (2013) 3428-3434.

7] T. Brousse and D. Belanger, ECS Solid State Let., 6 (2003) 244-248.

8] J. Wang, S. Liu, X. Zhang, X. Liu, X. Liu, N. Li, J. Zhao, Y. Li, Electrochim. Acta, 213 (2016) 663-671.

9] N. Bretesche, O. Crosnier, G. Buvat, F. Favier, T. Brousse, J. Power Sources, 326 (2016) 695-701.

10] S. Zhang, B. Yin, Z. Wang, F. Peter, Chem. Eng. J., 306 (2016) 193-203.

11] L. Zhang, W. Zheng, H. Jiu, C. Ni, J. Chang, G. Qi, Electrochim. Acta, 215 (2016) 212-222.

12] K. Huang, J. Zhang, K. Xing, Electrochim. Acta, 149 (2014) 28-33.

13] M. Jayalakshmi, M. Rao, B. Choudary, Electrochem. Commun. 6 (2004) 1119-

1122.

14] K. Krishnamoorthy, G. Veerasubramani, P. Pazhamalai, S. Kim, Electrochim. Acta, 190 (2016) 305-312.

15] N. Chodankar, G. Gund, D. Dubal, C. Lokhande, RSC. Adv., 4 (2014) 61503-615013.

16] A. Kumar, A. Sanger, A. Kumar, Y. Kumar, R. Chandra, Electrochim Acta, 220 (2016) 712-720.

17] M. Jiang, H. He, C. Huang, B. Liu, W. Yi, Z. Chao, Electrochim Acta, 219 (2016) 492-501.

18] W. Fu, W. Han, H. Zha, J. Mei, Y. Li, Z. Zhang, E. Xie, Phys. Chem. Chem. Phys., 18 (2016) 24471-24476.

19] K. Jeyabanu, K. Sundaramahalingam, P. Devendran, A. Manikandan, N. Nallamuthu, Physica B Condens. Matter, 572 (2019) 129-138.

20] S. Riyaz, A. Parveen, A. Azam. Perspect Sci., 8 (2016) 632-635.

21] U. Shamraiz, R. Hussain, A. Badshah, J. Solid State Chem., 238 (2016) 25-40

22] T. Hurma, and S. Kose, Optik, 127 (2016) 6000-6006.

23] H. Wang, Y. Wang, X. Cao, M. Feng, G. Lan, J. Raman Spectrosc., 40 (2009) 1791-1796

24] S. Iqbal, A. Bahadur, S. Anwer, M. Shoaib, G. Liu, H. Li , M. Raheel, M. Javed , B. Khalid, Cryst Eng Comm., 22 (2020) 4162-4173.

25] C. Raj, B. Kim, W. Cho, W. Lee, Y. Seo, K. Yu, J. Alloys Compd, 586 (2014) 191- 196

26] H. Peng, G. Ma, J. Mu, K. Sun, Z. Lei, Mater Lett., 122 (2014) 25-28

27] D. Dubal, J. Kim, Y. Kim, R. Holze, W. Kim, Energy. Technol., 1 (2013) 125-130

28] S. Shi, C. Xu, C. Yang, J. Li, H. Du, B. Li, F. Kang, Particuology, 11 (2013) 371-377

29] L. Nyholm, G. Nystrom, A. Mihranyan, M. Stromme, Adv. Mater., 23 (2011) 3751- 3769

30] P. Wen, M. Fan, D. Yang, Y. Wang, H. Cheng, J. Wang, J. Power Sources, 320 (2016) 28-36

31] B. Choi, S. Chang, C. Park, H. Kang, H. Kim, W. Hong, S. Lee, Y. Huh, Nanoscale, 4 (2012) 4983-4988

32] B. Zheng, T. Huang, L. Kou, X. Zhao, K. Gopalsamy, C. Gao, J. Mater. Chem. A, 2 (2014) 9736-9743

33] M. Jayalakshmi, M. Rao, B. Choudary, Electrochem. Commun., 6 (2004) 1119-1122.

34] K. Krishnamoorthy, G. Veerasubramani, P. Pazhamalai, S. Kim, Electrochim. Acta, 190 (2016) 305-312.

35] Y. Munaiah, B. Raj, T. Kumar, P. Ragupathy, J. Mater. Chem. A, 1 (2013) 4300-4306

36] A. Patil, A. Lokhande, P. Shinde, C. Lokhande, ACS Appl. Mater. Interfaces, 19 (2018) 16636-16649

37] G. Wang, M. Zhang, L. Lu, H. Xu, Z. Xiao, S. Liu, S. Gao, and Z. Yu, ChemNanoMat, 9 (2018) 964-971

38] B. De, T. Kuila, N. Kim, J. Lee, Carbon, 122 (2017) 247-257

39] X. Xu, Y. Yang, M. Wang, P. Dong, R. Baines, J. Shen, M. Ye, Ceram. Int., 42 (2016) 10719-10725

40] H. Naderi, A. Sobhani-Nasab, M. Rahimi-Nasrabadic, M. Ganjalia, Appl. Surf. Sci., 423 (2017) 1025-1034

41] S. Bernardini, F. Bellatreccia, A. Municchia, G. Ventura, A. Sodo, J. Raman Spectrosc., 50 (2019) 873-888

42] E. Guneri, A. Kariper, J. Alloys Compd., 516 (2012) 20-26

43] A. Phuruangrat, T. Thongtem, S. Thongtem, Chalcogenide Lett., 8 (2011) 291-295.

44] P. Deshmukh, S. Pusawale, V. Jamadade, U. Patil, C. Lokhande, J. Alloys Compd., 509 (2011) 5064-5069

45] K. Huang, J. Zhang, K. Xing, Electrochim. Acta, 149 (2014) 28-33,

46] N. Chodankar, D. Dubal, A. Lokhande, C. Lokhande, J. Colloid Interf. Sci., 460 (2015) 370-376

47] T. Brousse, D. Belanger, J. Long, J. Electrochem. Soc., 162 (2015) A5185-A5189

48] V. Pototskaya, O. Gichan, Int. J. Electrochem. Sci., 14 (2019) 8195-8205

49] W. Choi, H. Shin, J. M. Kim, J. Choi, W. Yoon, J. Electrochem. Sci. Technol., 11(2020) 1-13

50] D. Dubal, O. Ayyad, V. Ruiz, P. Gomez-Romero, Chem. Soc. Rev., 44 (2015) 1777-1790

51] D. Moye, P. Moss, D. Kannan, X. Chen, O. Bolufawi, W. Cao, S. Foo, Mater. Sci. Appl., 11 (2020) 347-369

CHAPTER-6

CONCLUSIONS

Conclusions

The electrical energy storage systems such as battery, capacitor and SCs are available in recent years. In which SC have ability to store charge rapidly and it has higher power density than batteries. The tremendous use of SCs in the flexible and wearable electronics has been intended for a number of applications like medical bio-monitoring devices for military equipment. The batteries have limited service lifetime, safety issue and small–scale power which restrict applications of batteries in portable electronic devices. In contradict, SCs offers higher power density, electrochemical cycling stability, better energy density and environmental energy storage. Therefore, SC technology is rising rapidly to substitute capacitors and batteries. Currently, SCs are being used in several applications such as telecommunications, hybrid electric vehicles, power back up sources, flash camera's, etc. In hybrid electric vehicles, the higher power during start is required.

The SCs give high power and energy to hybrid electric vehicles during start and so hybrid electric vehicles use SCs. Nevertheless, SCs have limitations with aqueous electrolytes, lower reduction potential of metal cations and higher resistivity of metal oxides. The FSS-ASCs device is the innovative member of energy storage SC and attracted due to its high power density, long cycle life, environmental friendliness and safety. To overcome these drawbacks of device, further electrode material investigation is necessary to enhance the performance of SCs. Temporarily, the combination of best active electrode materials with supportable electrolyte efficiently raises both the energy and power capability of the FSS-SCs device.

The previous reports suggest that the materials like metal oxides, conducting polymers and carbon based materials enhance the electrochemical performance of SC device. The transition metal oxide and hydroxide electrodes with pseudocapacitive behavior are of great interest in SCs. Due to the different oxidation states transition metal oxides are greatly studied as pseudocapacitive materials. The binary metal oxides does not show highest performance in every case and not in all environments. The pseudocapacitive performance of electrode material depends on number of factors, such as electrolyte concentration, type of electrolyte (neutral, alkaline, and acidic), mass loading, electrical conductivity, crystalline nature, etc. In fact, some single component metal oxides have shown promising electrochemical performance.

The electrochemical water splitting or electrolysis of water is the most feasible hydrogen production method at the time being. Among the reaction (HER) and oxygen evolution reaction (OER), OER is sluggish and complicated because it demands high overpotential which affects the overall water splitting. For this reason, the present study is focused upon the development and characterization of novel transition metal tungstate materials by successive ionic layer adsorption and reaction (SILAR) route for application as OER electrocatalysts in water splitting.

To fulfill the requirement, cobalt tungstate and cobalt tungstate/reduced graphene oxide composite electrodes were prepared via the SILAR methods on SS substrates. By these method, pristine cobalt tungstate was synthesized by varying the number of cycles in SILAR. Further in the optimized cobalt-tungstate, rGO concentration was varied and cobalt tungstate /reduced graphene oxide composite electrodes were synthesized for the study of supercapacitor and water splitting electrochemically in the forms of OER.

Chapter 1 gives an introduction about the energy economics and the present situation of energy generation. The drawbacks of fossil fuels and the need of renewable energy sources for example solar, wind, and hydrogen energy were discussed. Chapter deals with a general introduction and literature survey of different transition metal tungstates for SC and OER application. It displays information regarding mechanisms of energy exploitation from different energy sources. Consequently, the importance of energy storage from renewable energy sources is noted. It clarifies the most simple energy storage devices specifically capacitor, battery, and SC. It deals with a general introduction and literature survey of different transition metal tungstates for SC and OER application. It displays information regarding mechanisms of energy exploitation from different energy sources. Consequently, the importance of energy storage from renewable energy sources is noted. It clarifies the most simple energy storage devices specifically capacitor, battery, and SC. The different types of SCs along with their energy storage capabilities are discussed. The benefits of SCs over capacitors and batteries in terms of energy and power densities are mentioned. The reaction mechanisms of OER along with performance parameters have discussed thoroughly. The objectives of the research work such as to develop nanomaterial cobalt-tungstate/reduced graphene oxide composite electrodes, using effective SILAR method, which can work as efficient electrocatalysts for supercapacitor and OER.

Chapter 2 presents thin film preparation method and the advantages of chemical methods over physical thin film deposition methods. Out of chemical methods, the SILAR method is deemed to be more controllable on thin film deposition process. This method is comprised of three processes, i) adsorption, ii) reaction, and iii) rinsing. To evaluate the structural, morphological, and elemental compositional parameters different characterization techniques such as XRD, FESEM, FT-IR and Raman spectroscopy, XPS, contact angle measurement and BET were used. The basic principle and working mechanism of these techniques are discussed in chapter II in order to understand obtained results. Further, fundamental aspects and applications of various electrochemical techniques for energy storage application were studied in this chapter.

Thickness affects the charge storage, cycling stability, resistive parameters of the film electrode material. Considering this, the optimization of thin film thickness or mass loading is necessary which can be done by varying deposition cycles in SILAR method. Similarly, the theory behind electrochemical techniques used to evaluate supercpacitive and electrocatalytic OER performance was also studied in chapter 2. Since the film thickness or mass loading of the electrocatalyst significantly affects the OER performance.

Chapter 3 deals with the synthesis of $CoWO_4$ thin films by SILAR method gives the study of the effect of the mass loading on the physicochemical properties, electrochemical, electrocatalytic performance of cobalt tungstate. The mass loading of active material was found to significantly change with the number of SILAR deposition cycles and influenced the surface morphologly of the thin film. This chapter have three sections (A, B and C). Section A deals with the synthesis, physicochemical characterizations of $CoWO_4$ thin film by SILAR method. Co^{2+} ions were obtained by dissolving $CoCl_2$ precursor in DDW. The source of anion, WO_4^{2-} ions was taken from Na_2WO_4, and deposition was taken for 60, 90, 120, and 150 SILAR cycles respectively. The formation of $CoWO_4$ thin film was identified from XRD and FT-Raman investigations. The field emission scanning electron microscopy (FE-SEM) study showed the nano-grained surface morphology. The surface wettability study examined using drop of water over $CoWO_4$ film showed hydrophilic nature.

Section B deals with the electrochemical behaviour of $CoWO_4$ electrode was tested in an aqueous (1 M KOH) electrolyte. The three-electrode system configuration with platinum plate as a counter, $CoWO_4$ film as working, and mercury/mercury oxide (Hg/HgO) as a reference electrode were used. The supercapacitive properties of $CoWO_4$ film electrode were studied using the CV, GCD, and EIS tests. From the CV investigation, the electrochemical performance was investigated in terms of specific capacitance by varying scan rate. The GCD showed that $CoWO_4$ film electrode has good discharge ability. Further, the electrochemical cyclic stability was tested up to 3000 CV cycle at constant scan rate. The 88% electrochemical stability of $CoWO_4$ film electrode retained. These electrochemical tests are essential to decide the superior electrode material for fabrication of supercapacitor device.

Section C presents the study of the effect of mass loading on the OER performance of cobalt tungstate electrocatalyst. The mass loading of active material was found to significantly change with the number of SILAR deposition cycles and influenced the surface morphology of the thin film. As an impact of change in morphology, CW (deposited at 120 SILAR cycles) with mass loading 0.8 mg cm^{-2}, exhibited an efficient OER performance with 320 mV overpotential at 10 mA cm^{-2} and Tafel slope 110 mV dec^{-1}. The porous surface is evidenced as the main reasons for high ECSA (12.16 cm^{2}) and low R_{ct} values (4.5 Ω) which possibly enhanced the OER performance. This chapter highlights the importance of optimization of mass loading in the field of electrocatalytic OER.

To enhance the charge and mass transport efficiency, the coupling of transition metal tungstates with 3D conductive nanocarbon supports such as reduced graphene oxide (rGO) is a most efficient strategy. Therefore, in **Chapter 4**, the composite thin films of cobalt tungstate and reduced graphene oxide were synthesized. For this, the experimental conditions of previously optimized CW120 electrode was carry forwarded and varied concentration of rGO in composite electrode. This chapter have three sections (A, B and C).

Section A deals with the preparation and characterization of $CoWO_4$@rGO composite thin films by the SILAR method. The mass loading of $CoWO_4$@rGO thin films was 0.091 (±0.01) mg cm^{-2} and 0.106 (±0.01) mg cm^{-2}, respectively. The effect of rGO on chemical composition, crystal structure, and surface morphology was studied. Due to low concentration of rGO in cobalt tungstate, there is no any change in XRD pattern. The spherical-like morphology of $CoWO_4$ thin film modified to randomly distributed sheet-like morphology. The nanospheres of $CoWO_4$ coated on rGO sheets were observed in $CoWO_4$@rGO thin film. This mesoporous structure exhibited specific surface area of 65 m^{2} g^{-1} compared to 49 m^{2} g^{-1} of $CoWO_4$ material. Shift in average pore radius to lower dimension side (12.68 nm for $CoWO_4$ to 1.5 nm for $CoWO_4$@rGO) was the main cause of increased specific surface area.

Section B exhibits the supercapacitive properties of $CoWO_4$@rGO thin film were assessed using CV, charge-discharge, electrochemical stability and EIS study. The optimum rGO concentration (CWR 0.20) shows high C_s of 1201 F g^{-1} was achieved at the scan rate of 5 mV s^{-1}. The charge-discharge curves were non-linear indicating pseudocapacitive behaviour of CWR 0.20 composite thin film exhibited maximum C_s of

1280 F g^{-1} at the scan rate of 5 mV s^{-1}. The stability of CWR 0.20 thin film increased impressively from 88 to 93% after composition. The values of R_{ct} for $CoWO_4$ thin film were 4.5 Ω cm^{-2} and that of CWR 0.20 were 3.2 Ω cm^{-2}, respectively. In conclusion, the highest specific surface area offered by CWR 0.20 material helps to reduce ion diffusion resistance and maximum active sites exposed to the electrolyte improves the infiltration of electrolyte ions (OH^-) in the electrode.

Section C shows the electrocatalytic performance of $CoWO_4$@rGO composite thin film. For this, the experimental conditions of previously optimized CWR 0.20 electrocatalyst were carry forwarded and the quantity of rGO in composite electrocatalysts was optimized by changing the number of rGO concentration. Impressively, the CWR0.20 composite electrocatalyst showed excellent electrocatalytic OER performance. It required a notably low, 287 mV overpotential to reach 10 mA cm^{-2} current density and demonstrated a Tafel slope as low as 80 mV dec^{-1}. The significantly high OER performance was found to be facilitated by the optimum atomic stoichiometry, high electrochemically active surface area, improved electronic structures and better electronic conductivity. This part highlights the importance of controlling the amount of rGO during the synthesis of composite materials. $CoWO_4$@rGO composite thin film electrocatalysts requires low overpotential to reach 10 mA cm^{-2} current density as compared to pristine $CoWO_4$.

Chapter 5 contains the fabrication and demonstration of CuS//$CoWO_4$@rGO asymmetric FSS-ASCs device. In the first step, the CuS thin films synthesized by the SILAR method. For asymmetric device fabrication high performance positive electrode material is required. CuS has negative potential window with nanostructure morphology. Furthermore, this chapter includes the fabrication and electrochemical evaluation of CuS//$CoWO_4$@rGO asymmetric FSS-ASCs device using PVA-KOH polymer gel electrolyte. The CuS//$CoWO_4$@rGO asymmetric FSS–ASCs device exhibits the prolonged operating window of +1.7 V, which is due to different operating potential windows of CuS and $CoWO_4$@rGO thin films. It demonstrates the excellent C_s of 158 F g^{-1} with maximum S_E of 53 Wh kg^{-1} at power density of 1080 W Kg^{-1}.

In the present study, a system of transition metal oxide and its composite with a highly conducting carbon structure (rGO) was systematically optimized for energy storage and electrocatalytic OER by controlled experiments. Despite this work, there is a lot of work one can do to further improve the supercapacitive and OER performance as well as to enlighten the various aspects of electrocatalysts. Heteroatoms such as S and N doped rGO can be used instead of rGO. Also, zero-dimensional (0D) fullerene or one dimensional (1D) carbon nanotubes (CNT) can be used instead of two-dimensional (2D) rGO sheets to enhance the performance of transition metal oxide. In the present study and also in other numerous reports the basis of supercapacitive and OER performance of electrocatalysts is evaluated/concluded based on their physical properties such as phase, microstructures, hydrophilicity, etc.

CHAPTER-7

80-Recommendations

80-Recommendations

7.1 Recommendations:

In the presented research work, thin films of cobalt tungstate are prepared using SILAR method. The charge storage capacity of these thin film was improved by means of improvement in surface area. To achieve this rGO was composited with the cobalt tungstate using the SILAR method. The objective of the preparation of composite electrodes was to improve specific capacitance, stability and overpotential of the material than pristine materials. The solid state supercapacitor fabricated using these thin films delivered an energy density of 40.5 Wh kg^{-1} at 1087 W kg^{-1} power density.

Finally, it is recommended that, at 120 SILAR cycles, $CoWO_4$ thin film show best electrochemical and electrocatalytic performance. To get best electrochemical performance optimized concentration of rGO is 0.20 mg mL^{-1}. Due to the simplicity, scalable nature of the deposition method, it can be potentially translated at industrial level with minimum modification.

7.2 Conclusions:

The conclusions from the present research work are listed as follows:

1. The mass loading per unit area of electrode is controlled through variation of deposition cycles. Optimum mass loading of electrode was essential for highest electrochemical and electrocatalytic performance.
2. At the optimum mass loading charge transfer resistance per unit mass is minimum and thereafter it increased. Cobalt tungstate thin film deposited at 120 SILAR cycles showed best electrochemical and electrocatalytic performance.
3. Composition of rGO with cobalt tungstate improve specific surface area. This leads to increase in electrochemical active sites and improvement in charge storage through capacitive assisted mechanism. As the pristine rGO has very low specific capacitance, optimization of composition of each material need to be considered. For cobalt tungstate 0.20 mg mL^{-1} concentraion of rGO suspension provide better effect on electrochemical properties.
4. Composition of cobalt tungstate with the rGO increased in electrochemical stability of the electrodes. Stability of $CoWO_4$ was improved from 88% to 93% ($CoWO_4$@rGO).

5. Compared to composite electrodes of cobalt tungstate/reduced graphene oxide ($CoWO_4$@rGO) electrochemical performance of electrodes of cobalt tungstate ($CoWO_4$) is lower.
6. Asymmetric solid-state supercapacitor fabricated using CuS and $CoWO_4$@rGO delivers energy density of 53 Wh kg^{-1} at the power density of 1080 W kg^{-1}.

7.3 Summary:

The present work deals with the synthesis of cobalt tungstate thin films by simple, cost effective and binder–free chemical approach. The numbers of preparative parameters were optimized to get highly porous surface morphology with higher specific surface area, which successfully increase the electrochemical features of $CoWO_4$ thin film. The composite thin films showed better SC performance than $CoWO_4$ thin films. Therefore, the composite thin films with excellent electrochemical features were used as one electrode for fabrication of FSS-ASCs device. Furthermore, CuS was selected as negative electrode with a wide potential window (0.0 to -1.2 V).

The significance of thin film and different nanostructure morphologies of material is explained in brief. The different electrode materials such as carbon based materials, metal oxides/hydroxides, and conducting polymers are discussed. The significance of metal tungstate for SC and OER application is described concerning a contribution from non-faradaic reactions in addition to faradaic reactions. The literature survey of transition metal oxides includes preparation methods, properties, and applications. Furthermore, the literature survey of cobalt tungstate based electrode materials for supercapacitive and electrocatalytic applications is carried out and finally, the orientation and purpose of the thesis are described.

The thin film preparation method and the advantages of chemical methods over physical thin film deposition methods are discussed. Out of chemical methods, the SILAR method is deemed to be more controllable on thin film deposition process. This method is comprised of three processes, i) adsorption, ii) reaction, and iii) rinsing. To evaluate the structural, morphological, and elemental compositional parameters different characterization techniques such as XRD, FE-SEM, FT-IR and Raman spectroscopy, XPS, contact angle measurement and BET were used. The basic principle and working mechanism of these techniques are discussed to understand obtained results. Further, fundamental aspects and applications of various electrochemical techniques for energy storage and electrocatalytic applications are discussed.

Thickness affects the charge storage, cycling stability, resistive parameters of the film electrode material. Considering this, the optimization of thin film thickness or mass loading is necessary which can be done by varying deposition cycles in SILAR method.

From this perspective, the study of the effect of mass loading on the physico-chemical properties, electrochemical, and electrocatalytic performance of cobalt tungstate is evaluated. Since the ratio of rGO in the composite film decides the overall electrochemical performance of the film, the effect of amount of rGO on the electrochemical performance of $CoWO_4$@rGO thin films was evaluated. The crystalline nature of $CoWO_4$ thin films changes with the composition of rGO. With mass loading 0.0126(±0.001) mg cm^{-2}, CW120 thin film ($CoWO_4$ film prepared at 120 cycles) exhibited the specific capacitance of 1201.8 F g^{-1} at the scan rate of 5 mV s^{-1} and stability of 93 % after 3000 GCD cycles.

The mass loading of $CoWO_4$@rGO 0.20 (CWR0.20) thin film of 0.0137(±0.001) mg cm^{-2}, indicated an increase in mass loading with the introduction of rGO. The C_s of the composite film was 1201.8 F g^{-1} at the scan rate of 5 mV s^{-1} and stability of 93% over 3000 GCD cycles. The values of R_s and R_{ct} for CW120 thin film were 0.88 and 4.5 Ω cm^{-2} and that of $CoWO_4$@rGO0.20 were 0.78 and 3.20.Ω cm^{-2}, respectively. Thus the composition of $CoWO_4$ with rGO in proper ratio can be used to modify structural and morphological properties and able to improve specific capacitance. Due to higher mass loading R_s of $CoWO_4$@rGO composite thin film was more. This highlights superiority of $CoWO_4$@rGO thin film over $CoWO_4$ and rGO thin films.

The thin films of CuS were prepared using SILAR method and characterized for electrochemical performance evaluation. CuS thin film exhibited a specific surface area of 32.4 cm^2 gm^{-1} and an average pore radius of 29 nm. The mesoporous surface showed a hydrophilic nature. In addition to this, CuS thin film exhibited C_s of 687 F g^{-1} at a scan rate of 5 mV s^{-1}. Low resistive parameters such as R_s (1.94 Ω cm^{-2}) and R_{ct} (17.4 Ω cm^{-2}) and capacitive retention of 89% after 3000 GCD cycles of CuS thin film electrode ascribed to its nanostructured morphology consisting nanospheres.

The FSS-ASC devices with configuration of CuS//$CoWO_4$@rGO was fabricated. The CuS//$CoWO_4$@rGO FSS-ASC device exhibited the operating voltage of +1.7 V, which is due to different operating potential windows of $CoWO_4$@rGO and CuS thin films. It exhibited the excellent C_s of 158 F g^{-1} with a maximum S_E of

53 Wh kg^{-1} at the power density of 1087 W kg^{-1}. The CuS//$CoWO_4$@rGO FSS-ASC device showed capacitance retention of 94% after 5000 CV cycles.

Finally, FSS–ASC devices connected in series were able to glow a panel of 211 red LEDs efficiently. The initial power dissipated through CuS//$CoWO_4$@rGO FSS-ASC was 31 mW/cm^2. Finally, the observed results conclude that the cobalt tungstate based FSS-ASCs can power up small electronic gadget requiring power in the range of 0.01 mW to 0.1 mW.

7.4 Future findings:

In this study, cobalt tungstate thin films and their composites with rGO were synthesized using automated SILAR method. The introduction of rGO improves electrical conductivity, specific surface area, and overall electrochemical performance of pristine material. Instead of rGO, other carbon allotropes like fullerene, CNTs, carbon aerogel, and carbon foam for the composition can be used. Along with this, the composition of other transition metals (Ni, Co, Cr) to form a bimetallic compound will also enhance the electrochemical energy storage and catalytic properties of the electrode material. To understand the process of energy storage in cobalt tungstate based compounds, physical characterization of these materials should be performed to analyze changes in the crystal structure, surface morphology, and chemical composition using techniques such as XRD, SEM, TEM, and XPS.